Investigating electromagnetic properties of topological surface states in mercury telluride

Dissertation zur Erlangung des naturwissenschaftlichen Doktorgrades der Julius-Maximilians-Universität Würzburg

vorgelegt von
Florian Bayer
aus Schweinfurt

Würzburg, 2023

Eingereicht am: 07.07.2023
bei der Fakultät für Physik und Astronomie

1. Gutachter: Dr. Tobias Kießling
2. Gutachter: Prof. Dr. Ralph Claessen
3. Gutachter: _____
der Dissertation

Vorsitzender: Prof. Dr. Friedrich Reinert
1. Prüfer: Dr. Tobias Kießling
2. Prüfer: Prof. Dr. Ralph Claessen
3. Prüfer: Prof. Dr. Ronny Thomale
im Promotionkolloquium

Tag des Promotionskolloquiums: 09.02.2024

Doktorurkunde ausgehändigt am: _____

Zusammenfassung

Diese Doktorarbeit untersucht die magneto-optischen Eigenschaften zugverspannter Quecksilbertelluridschichten auf Cadmiumtelluridsubstraten. Die Schichtdicken sind hierbei dicker als die gewöhnlicher Quantentrogsysteme bis etwa 20 nm und nach oben hin beschränkt durch Gitterrelaxationeffekte ab ca. 100 nm. Dieses Schichtsystem wurde in zahlreichen Publikationen der Materialklasse dreidimensionaler Topologischer Isolatoren zugeordnet, welche sich durch intrinsische Grenzflächenzustände auszeichnet, die energetisch in der Bandlücke des Schichtinneren liegen.

Um die Eigenschaften der Bandstruktur im direkten Umfeld der Fermi-Kante, inklusive etwaiger Grenzflächenzustände, untersuchen zu können, kommt die Methode der hochpräzisen Zeitdomänen-Terahertz-Polarimetrie zum Einsatz. Der Stand der dazu nötigen Technik wird zu Beginn der Doktorarbeit einleitend diskutiert und der daraus entstandene Messaufbau wird im Detail beschrieben, sowie dessen Charakterisierung erläutert. Die typischerweise erzielbare Standardabweichung einer Messung liegt, je nach Transmissionsgrad der untersuchten Probenstrukturen, im Bereich weniger 10 – 100 Tausendstel Grad für die Polarisationgrößen Rotation und Elliptizität. In Abhängigkeit externer Magnetfelder bis hin zu 10 Telsa ergeben sich so mittels Fourier-Transformation des Zeitsignals verschiedene Polarisationspektren.

Der Rückschluss auf die zugrunde liegende Bandstruktur gelingt durch die Modellierung möglicher Bandstrukturen mittels der Einhüllenden-Funktionen-Näherung der $\boldsymbol{k} \cdot \boldsymbol{p}$-Methode. Hierzu wird zunächst die Bandstruktur nach den gewählten Modellparametern berechnet und aus dieser wiederum die zu erwartenden Elliptizitätsspektren in Abhängigkeit des externen Magnetfeldes und der Ladungsträgerkonzentration berechnet. Aus dem Vergleich berechneter und tatsächlich gemessener Spektren wird im Laufe der Arbeit die Validität verschieden detaillierter $\boldsymbol{k} \cdot \boldsymbol{p}$-Modelle analysiert. Die reichhaltigen Informationen aus der Elliptizitätsmesung liefern bei der Zuordnung einzelner optischer Übergänge entscheidende Hinweise, die in reiner Absorptionsspektroskopie nicht enthalten sind. So ist das Vorzeichen der Elliptizität verknüpft mit der Zusammensetzung der am optischen Übergang beteiligten Landau-Level Zustände. Dies ermöglicht einen direkten Nachweis sogenannter Bulk-Inversions-Asymmetrie-Effekte aus den Spektren.

Im Verlauf der Arbeit wird zudem wiederholt ein Vergleich der Ergebnisse mit existierenden Publikationen gezogen, wobei sich zeigt, dass dort verwendete Modelle häufig unzureichend oder inkorrekt sind. Wo immer dies sinnvoll und ohne größeren Aufwand möglich ist, werden die Unterschiede zu Aussagen, die aus dem $\boldsymbol{k} \cdot \boldsymbol{p}$-Modell heraus getroffen werden können, diskutiert.

Zum Ende der Analyse hin wird verstärkt auf die Grenzen der $\boldsymbol{k} \cdot \boldsymbol{p}$-Methode eingegangen und verbleibende Abweichungen zwischen Modell und Messung diskutiert. Dies beinhaltet sowohl die Qualität der verwendeten Modellparameter, als auch verschiedene Versuche, die in den Strukturen vorhandenen elektrostatischen Potentiale mit in die Modellierung zu integrieren.

Abschließend wird ein Ausblick auf mögliche zukünftige Entwicklungen des Quecksilbercadmiumtellurid Schichtsystems und die Anwendung der hier vorgestellten Methodiken auf weitere Fragestellungen gegeben.

Abstract

This doctoral thesis investigates magneto-optical properties of mercury telluride layers grown tensile strained on cadmium telluride substrates. Here, layer thicknesses start above the usual quantum well thickness of about 20 nm and have a upper boundary around 100 nm due to lattice relaxation effects. This kind of layer system has been attributed to the material class of three-dimensional topological insulators in numerous publications. This class stands out due to intrinsic boundary states which cross the energetic band gap of the layer's bulk.

In order to investigate the band structure properties in a narrow region around the Fermi edge, including possible boundary states, the method of highly precise time-domain Terahertz polarimetry is used. In the beginning, the state of the art of Teraherz technology at the start of this project is discussed, moving on to a detailed description and characterization of the self-built measurement setup. Typical standard deviation of a polarization rotation or ellipticity measurement are on the order of 10 to 100 millidegrees, according to the transmission strength through investigated samples. A range of polarization spectra, depending on external magnetic fields up to 10 Tesla, can be extracted from the time-domain signal via Fourier transformation.

The identification of the actual band structure is done by modeling possible band structures by means of the envelope function approximation within the framework of the $\boldsymbol{k} \cdot \boldsymbol{p}$ method. First the bands are calculated based on well-established model parameters and from them the possible optical transitions and expected ellipticity spectra, all depending on external magnetic fields and the layer's charge carrier concentration. By comparing expected with measured spectra, the validity of $\boldsymbol{k} \cdot \boldsymbol{p}$ models with varying depths of detail is analyzed throughout this thesis. The rich information encoded in the ellipitcity spectra delivers key information for the attribution of single optical transitions, which are not part of pure absorption spectroscopy. For example, the sign of the ellipticity signals is linked to the mix of Landau levels which contribute to an optical transition, which shows direct evidence for bulk inversion asymmetry effects in the measured spectra.

Throughout the thesis, the results are compared repeatedly with existing publications on the topic. It is shown that the models used there are often insufficient or, in worst case, plainly incorrect. Wherever meaningful and possible without greater detours, the differences to the conclusions that can be drawn from the $\boldsymbol{k} \cdot \boldsymbol{p}$ model are discussed.

The analysis ends with a detailed look on remaining differences between model and measurement. It contains the quality of model parameters as well as different approaches to integrate electrostatic potentials that exist in the structures into the model.

An outlook on possible future developments of the mercury cadmium telluride layer systems, as well as the application of the methods shown here onto further research questions concludes the thesis.

Contents

1 Introduction

> Nothing is ever completed.
> Incompleteness is a part of nature and it needs great art or great wisdom to know when to lay down the brush [...] we should always avoid perfectionism.
>
> Jean Omer Marie Gabriel Monnet

1.1. Topological materials

Within the last two decades, the classification of condensed matter into (semi)conductors and insulators was revolutionized and developed further by introducing the concept of topological invariants. These invariants are integer numbers that classify the band structure of materials further and connect to the symmetry properties of the materials bulk bands [1, 2].

The most famous class of topological materials is the one of Topological Insulators (TIs) [3, 4], which describes systems that are ideally insulating in the bulk but are guaranteed to have conducting states at the surface or interface to topologically trivial systems, e.g. conventional (semi-)conductors. The topological protection of those interface states essentially boils down to an inverted bulk band structure which at the interface connects to normally (or trivially) ordered bands.

Even though first descriptions of conductive states at inverted-normal band structure interfaces [5, 6] as well as a concept of topological invariants (in terms of the Chern number linked to the integer quantum Hall effect (QHE) [7, 8]) had already existed in the 1980s, it took another twenty years before a topological invariant was used to classify band inversions [3] in two-dimensional systems. The approach was later generalized and extended to three-dimensional systems [9, 10, 11].

First suggestions for promising materials [12] and experimental validation using (magneto-) transport measurements on mercury cadmium telluride quantum wells (QWs) [13, 14] and angle-resolved photoemission spectroscopy (ARPES) on three-dimensional Bismuth based compounds [15, 16, 17] followed soon after.

The combination with time-reversal symmetry, relativistic corrections to the bandstructure and strong spin-orbit coupling (due to the large mass of the involved elements) gives rise to interesting properties, such as spin-momentum locking and suppressed back-scattering of the surfaces states [18]. Furthermore, universally quantized observables like optical Faraday and Kerr rotation have been proposed [11] and were claimed to be observed in experiments[1] [19, 20]. However, it can be shown that the effect does not produce a measurable net rotation under most circumstances and generally is *not* universally quantized [A1].

A promising application of topological materials is proposed in the field of (topological) quantum computing. A topological superconductor (which can for example be built from a TI in proximity to a conventional superconductor [21]) may host zero-energy Majorana bound states. The interaction of such qubit-like states can be described by non-Abelian statstics and is potentially useful for building a quantum computer [2, 22].

[1] At the beginning of this project, the observation of the quantized topological magneto-electric effect through the Faraday rotation caused by it was one of the goals.

1.2. A note on band structure models

The beauty of the theoretical approach to topological insulators lies in the prediction of presence of bulk gap crossing surface states from very simple Hamiltonians, constructed just from basic symmetry arguments. This will be discussed on the example of mercury cadmium telluride quantum wells and the model by Bernevig, Hughes and Zhang (BHZ) [12].

From $\boldsymbol{k} \cdot \boldsymbol{p}$ calculations the authors deduced that the spin degenerate uppermost valence subband H1 and lowest conduction subband E1 of thin HgTe layers sandwiched between CdTe barriers become inverted when the quantum well thickness is increased beyond a critical value $d_c \approx 6.4$ nm. Around the inversion point, both subbands are sufficiently far away in energy from other subbands, such that the authors are able to construct a simplified four-band Hamiltonian, assuming inversion and time-reversal symmetries.

This effective Hamiltonian is treated only in lowest order of momentum k and is only valid in a very narrow region around the Γ ($k = 0$) high-symmetry point of the Brillouin zone. Here, the authors find a linear dispersion relation similar to massless/massive relativistic particles at/near thickness $d \approx d_c$. This structure is called a Dirac cone and can be found similarly in other topological insulators. The linear dispersion is a prominent feature of the effective models constructed for a clear explanation of concepts of topology by leaving aside the fine details of interaction with remote bands. Generally, the presence of a topological non-trivial system is not automatically linked to Dirac cones with linear dispersion. Such simple models may, however, be a very suitable approximation to the real band structure in some cases like graphene [23, 24, 25, 26].

The downside of the effective models for topological systems is, that people started to automatically link TIs with the existence of Dirac fermion states in the bulk band gap and as such at the system's Fermi level. Since tensile strained HgTe was predicted to be a three-dimensional TI, where Dirac states would lead to unusual quantum Hall conductivity [10] similar to graphene [26], there have been many claims to have measured such signatures [27, 28, 29, 30]. But from the very same $\boldsymbol{k} \cdot \boldsymbol{p}$ calculations that are the foundation of the BHZ model, one can follow the inverted E1 band further down into the valence band states with increasing HgTe layer thickness. Already at QW thicknesses of 15 nm one may observe the formation of a 'massive' Dirac cone structure between the E1 and the L1 subbands about 0.1 eV below the bulk band gap, while the gap crossing H1 band has a quadratic dispersion[2] [32, 33].

Therefore, the actual bands causing Dirac signatures should be completely filled and can not contribute a signal to experiments based on charge transport (i.e. probing the conductivity). Which raises the question about the cause of magneto-transport phenomena, but also observations from optical experiments [20, 28, 30, 34].

1.3. Objective of this work

To shed some light on open questions that arise from measurements on $Hg_{0.32}Cd_{0.68}Te$ - HgTe - $Hg_{0.32}Cd_{0.68}Te$ 'quantum wells' in the limit of thick, strained bulk-like HgTe layers[3]. A structured, detailed and quantitative analysis of the observations requires an accurate model of the

[2] The H1 dispersion of thicker layers resembles the dispersion of conduction subbands, but starts out directly above the H2 subbands with a negligible gap. $\boldsymbol{k} \cdot \boldsymbol{p}$ calculations show that the position of the Dirac point may be controlled by alloying the HgTe layer with approximately 14% cadmium [31].

[3] Mercury telluride can not be grown as fully strained layer for arbitrary thicknesses, but starts to show signs of relaxation after approximately 150 nm, depending on the $Hg_{0.32}Cd_{0.68}Te$ buffer layer thicknesses [35]. 'Thick' (> 20 nm) is to be interpreted with respect to trival/topological QW thicknesses close to 6 nm.

electronic bandstructure, which can be used to calculate theoretically expected measurement outcomes.

By comparing the modeled measurement signatures with real experimental data and successive refinement of the model and its parameters, one may gain insight into the actual bandstructure of a specific sample. Approaches to deduce the band structure directly from measurement results so far did not mange to cover the details of the complicated bandstructure correctly [36].

This work thus tackles the issue both from experimental, as well as theoretical side to unravel the properties of band gap crossing surface states in such materials:

Experimentally, multiple samples with HgTe layer thicknesses from 30 nm up to 90 nm have been investigated using a state-of-the-art time-domain (TD) Terahertz (THz) spectrometer with wold-leading polarization resolution, built by the author. The small photon energy scale of up to 10 meV allows to probe intra-band Landau level (LL) transitions of interface and bulk states alike. The additional Lock-In polarization technique not only dramatically boosts the achievable signal to noise ratio (SNR) but adds important information on the character of the transitions. Finally, specifically developed lithographic structuring of the sample allows for simultaneous measurement and reliable tuning of the charge carrier density inside the sample. This results in an unprecedentedly detailed collection of spectra probing the region around the bulk band gap.

From the perspective of theory, eight-band $\boldsymbol{k}\cdot\boldsymbol{p}$ models are used to calculate band structures and their expected optical spectra[4]. The effects of different levels of symmetry in the model Hamiltonian on the magnetic field dependence of LLs are discussed. It is found that asymmetry terms, often neglected in previous [32] and present [36] work, are required to describe the valence band states accurately.

As no model is ever truly perfect, the discussion points out, where the current set of parameters fails to describe measurements accurately. As there is still much development, both in quality of samples, as well as in the details of the extensive $\boldsymbol{k}\cdot\boldsymbol{p}$ models, a roadmap for continuation of this project is given towards the end of this thesis.

1.4. A short comparison of measurement techniques

There are a bunch of experimental methods commonly used to determine electronic bandstructures directly or help to reconstruct it indirectly from measured quantities. The most common techniques are listed shortly together with their strengths and downsides with respect to the objective of this work.

Angle-resolved photoemission spectroscopy (ARPES) often comes to mind first, due to its current popularity and the ability to directly determine the ground state bandstructure[5] over large ranges in momentum and energy. However, the energy resolution compared to other methods is often rather poor and the sensitivity for bands is not uniform in momentum space [38], which can lead to missing information if some states can not be detected. Furthermore, the method is only sensitive to the bare, vacuum exposed, surface of a sample piece and can not access deeper layers within.

Scanning tunneling spectroscopy can probe the local density of surface states with a high energy resolution and can be used complementary to ARPES to investigate details of band

[4]The `kdotpy` [37] framework, to which the author has also contributed, is used throughout this thesis.
[5]The method can not measure excited conduction band states.

structure properties like quasi-particle scattering vectors [18]. By itself it does not offer momentum resolution for the band structure. Like ARPES, this method is only sensitive to the sample surface.

Electron magneto-transport is able to probe Landau level (LL) fan charts, i.e. the variation of longitudinal and Hall conductance against changing magnetic fields and the charge carrier density. This method can map out the evolution of LL states and further yields the connected layer's charge carrier density and mobility. As the method does not offer direct access to an energy scale a direct reconstruction of the LL energy evolution and band structure is not possible. However, the position of crossing points between LL states allows for conclusive comparisons between a modeled bandstructure and measurements. The technique is sensible to bulk and surface states close to the Fermi level. This method can only directly measure states extending between electrical contacts to the sample.

Magneto-optical techniques probe selective transitions between LL states by photon absorption. In contrast to magneto-transport, an energy scale for the distance between LLs states is directly given by the photon energy, which can be used for precise quantitative comparison with a modeled bandstructure. In contrast to ARPES, these techniques come with better energy resolution and are not limited to surfaces, but also probe the bulk of a sample. Layered and gated structures to improve the sample properties and control the samples charge carrier concentration are also possible. However, it does not yield information directly in momentum space and usually only samples within a narrow momentum range around high symmetry points. The sensitivity around the Fermi energy is related to the usable photon energy range. At larger photon energies there are typically more detectable transitions between different states, which may overlap at the same transition energies, complicating the analysis of acquired signals. The choice to use the low-energy THz spectrum for this work instead of a broad-band energy range Fourier transform infrared (FTIR) spectrometer thus also helps to focus on the detailed analysis of single transitions.

2 $\boldsymbol{k \cdot p}$ theory

2.1. A bicyclist's guide

This introduction to band structure and Landau level calculation based on $\boldsymbol{k} \cdot \boldsymbol{p}$ theory derives the numerical models starting from basic quantum mechanical principles. The description of the steps is reduced to a minimum level required for the understanding of the concepts and implications for the results discussed later on. By no means, this section should provide a full pedestrian's guide to $\boldsymbol{k} \cdot \boldsymbol{p}$ theory. For more details [39, 40] are recommended literature. This section roughly follows along the path and notations given there.

2.1.1. Bulk band structures

Derivation of the $\boldsymbol{k} \cdot \boldsymbol{p}$ Hamiltonian

The description of electron states of any condensed matter system after making use of the Born-Oppenheimer approximation and neglecting atomic core motion is given by the Hamiltonian

$$\mathcal{H}_\mathrm{e} = \sum_i \frac{p_i^2}{2m_i} + \frac{1}{2} \sum_{\substack{i,i' \\ i \neq i'}} \frac{e^2}{4\pi\epsilon_0 \left| \boldsymbol{r}_i - \boldsymbol{r}_{i'} \right|} - \sum_{i,j} \frac{Z_j e^2}{4\pi\epsilon_0 \left| \boldsymbol{r}_i - \boldsymbol{R}_{j0} \right|}, \tag{2.1}$$

where the sums run over all electrons i, i' and atomic cores j. The first terms describe the kinetic and Coulomb potential energy of the electrons, while the last term expresses the interaction between electrons and atomic cores in their time-averaged position $\boldsymbol{R}_{j0}$.

As it is impossible to calculate the eigenstates of eq. (2.1) for many-body systems with $\gg 10^{20}$ electrons, a mean-field approximation is used. In this model each electron only interacts with the same averaged potential $V(r)$, yielding the Schrödinger equation with a one-electron Hamiltonian

$$\mathcal{H}_{1e} \Psi_n(\boldsymbol{r}) = \left(\frac{p^2}{2m} + V(\boldsymbol{r}) \right) \Psi_n(\boldsymbol{r}) = E_n \Psi_n(\boldsymbol{r}), \tag{2.2}$$

where E_n and Ψ_n are the energy eigenvalues and eigenstates of the Hamiltonian. Here, n is an index denoting the electron spin and band. Ψ_n can be decomposed into Bloch functions which span a full set of orthonormal eigenvectors in the Hamiltonian's Hilbert space:

$$\Psi_n(\boldsymbol{r}) = \sum_{\boldsymbol{k}} c_{n\boldsymbol{k}} \exp(i\boldsymbol{k}\boldsymbol{r}) u_{\boldsymbol{k}}(\boldsymbol{r}) = \sum_{\boldsymbol{k}} \psi_{n\boldsymbol{k}} = \sum_{\boldsymbol{k}} \exp(i\boldsymbol{k}\boldsymbol{r}) u_{n\boldsymbol{k}}(\boldsymbol{r}). \tag{2.3}$$

Here, $u_{\boldsymbol{k}}(\boldsymbol{r})$ are Bloch functions which, per definition, have the same periodicity as the crystal lattice. For simplicity the $c_{n\boldsymbol{k}}$ are contracted into the Bloch function as $u_{n\boldsymbol{k}}(\boldsymbol{r})$. As the Bloch functions are eigenstates of the Hamiltonian the explicit summation over $\boldsymbol{k}$ drops out when inserting eq. (2.3) into eq. (2.2). The application of the $\boldsymbol{p}$ operator onto the plain wave factor $\exp(i\boldsymbol{k}\boldsymbol{r})$ of the eigenfunctions directly yields the $\boldsymbol{k} \cdot \boldsymbol{p}$ Hamiltonian

$$\mathcal{H}(\boldsymbol{k}) u_{n\boldsymbol{k}} = \left(\frac{p^2}{2m} + \frac{\hbar \boldsymbol{k} \cdot \boldsymbol{p}}{m} + \frac{\hbar^2 k^2}{2m} + V \right) u_{n\boldsymbol{k}} = E_n(\boldsymbol{k}) u_{n\boldsymbol{k}}, \tag{2.4}$$

where the $\boldsymbol{r}$ dependency is hidden for a simpler notation.

Expansion around $\boldsymbol{k}_0$

To further simplify the calculation one can now expand the $u_{n\boldsymbol{k}}$ in terms of the complete and orthonormal $u_{l\boldsymbol{k}_0}$ basis [41, 42] around $\boldsymbol{k}_0$ as

$$u_{n\boldsymbol{k}} = \sum_l c_{nl}(\boldsymbol{k}) u_{l\boldsymbol{k}_0}. \tag{2.5}$$

Note that $u_{l\boldsymbol{k}_0}$ are not necessarily eigenstates of the Hamiltonian of eq. (2.4), but only of $\mathcal{H}(\boldsymbol{k}_0)$. When the eigensystem at the $\boldsymbol{k}_0$ point is known (e.g. from symmetry considerations and experimental input, see eq. (2.21)), it is useful to rewrite[1]:

$$\mathcal{H}'(\boldsymbol{k}) = \mathcal{H}'(\boldsymbol{k}_0) + \frac{\hbar(\boldsymbol{k}-\boldsymbol{k}_0)\cdot\boldsymbol{p}}{m} = \mathcal{H}_0 + \mathcal{H}_{\boldsymbol{k}\cdot\boldsymbol{p}} \tag{2.6}$$

$$E'_n(\boldsymbol{k}) = E_n(\boldsymbol{k}) - \frac{\hbar^2 k^2}{2m}, \tag{2.7}$$

where $E'_n(\boldsymbol{k})$ are the eigenvalues to the reduced Hamiltonian eq. (2.6), derived from eq. (2.4).

There exist different techniques to solve the Hamiltonian using perturbation theory. The more popular conventional perturbation theory, as discussed by [39], is presented first, followed by the more insightful derivation using the Löwdin partitioning method [40].

Expanding $E'_n(\boldsymbol{k})$ around $\boldsymbol{k}_0$ yields:

$$E'_n(\boldsymbol{k}) = E'_n(\boldsymbol{k}_0) + \sum_j (\boldsymbol{k}-\boldsymbol{k}_0)^j \frac{1}{j!} \left.\frac{\mathrm{d}^j E'_n(\boldsymbol{k})}{\mathrm{d}\boldsymbol{k}^j}\right|_{\boldsymbol{k}=\boldsymbol{k}_0} \tag{2.8}$$

$$= E_n(\boldsymbol{k}_0) + \sum_j (\boldsymbol{k}-\boldsymbol{k}_0)^j \frac{1}{j!} \left.\frac{\mathrm{d}^j E_n(\boldsymbol{k})}{\mathrm{d}\boldsymbol{k}^j}\right|_{\boldsymbol{k}=\boldsymbol{k}_0} - \frac{\hbar^2 k_0^2}{2m} - \frac{\hbar^2(\boldsymbol{k}-\boldsymbol{k}_0)\cdot\boldsymbol{k}_0}{m} - \frac{\hbar^2(\boldsymbol{k}-\boldsymbol{k}_0)^2}{2m} \tag{2.9}$$

$$= E_n(\boldsymbol{k}_0) + \sum_j (\boldsymbol{k}-\boldsymbol{k}_0)^j \frac{1}{j!} \left.\frac{\mathrm{d}^j E_n(\boldsymbol{k})}{\mathrm{d}\boldsymbol{k}^j}\right|_{\boldsymbol{k}=\boldsymbol{k}_0} - \frac{\hbar^2 k^2}{2m} \tag{2.10}$$

$$= E'_n(\boldsymbol{k}_0) + \sum_j (\boldsymbol{k}-\boldsymbol{k}_0)^j \frac{1}{j!} \left.\frac{\mathrm{d}^j E_n(\boldsymbol{k})}{\mathrm{d}\boldsymbol{k}^j}\right|_{\boldsymbol{k}=\boldsymbol{k}_0} + \frac{\hbar^2(k_0^2-k^2)}{2m} \tag{2.11}$$

From now on, $\boldsymbol{k}_0 = 0$[2] is used, as it simplifies the expressions for discussion. From a physical point of view, choosing $\boldsymbol{k}_0 = 0$ is also beneficial, as in zinc-blend type materials the Brillouin zone center is a high-symmetry point. These materials typically have their band extrema and minimal band gap at this point[3].

Treating $\mathcal{H}_{\boldsymbol{k}\cdot\boldsymbol{p}}$ as small perturbation to $\mathcal{H}_0$ (see eq. (2.6)) using nondegenerate perturbation theory up to second order in energy, one can identify those terms in the expansion eq. (2.10). As stated above, the expansion is done at band extrema $\left.\frac{\mathrm{d}E_n(\boldsymbol{k})}{\mathrm{d}\boldsymbol{k}}\right|_{\boldsymbol{k}=\boldsymbol{k}_0} = 0$ and with $\boldsymbol{k}_0 = 0$ it follows that there are no terms linear in k inside the $E'_n(\boldsymbol{k})$ expansion.

Therefore, the resulting dispersion up to second order of k can be expressed analytically

[1] The quadratic dispersion $\frac{\hbar^2 k^2}{2m}$ is moved from the original Hamiltonian part of the Schrödinger equation into the eigenvalues. This change is reflected here in the notation by additional dashes.

[2] This point is commonly labeled Γ, following group theory notation.

[3] Small effects from spin interaction can lift this condition and introduce terms linear in k [39, 43].

$$E_n(\boldsymbol{k}) = E'_n(\mathbf{0}) + \frac{\hbar^2 k^2}{2m} + \frac{\hbar^2}{m^2} \sum_{l \neq n} \frac{|\langle u_{n\mathbf{0}} | \boldsymbol{k} \cdot \boldsymbol{p} | u_{l\mathbf{0}} \rangle|^2}{E_n(\mathbf{0}) - E_l(\mathbf{0})}, \tag{2.12}$$

with $u_{n\boldsymbol{k}}$ to first order of k

$$u_{n\boldsymbol{k}} = u_{n\mathbf{0}} + \frac{\hbar}{m} \sum_{l \neq n} \frac{|\langle u_{n\mathbf{0}} | \boldsymbol{k} \cdot \boldsymbol{p} | u_{l\mathbf{0}} \rangle|}{E_n(\mathbf{0}) - E_l(\mathbf{0})} u_{l\mathbf{0}}. \tag{2.13}$$

The matrix elements $\langle u_{n\mathbf{0}} | \boldsymbol{k} \cdot \boldsymbol{p} | u_{l\mathbf{0}} \rangle$ can be expressed in term of the so called Kane matrix element P, a material specific parameter with $P^2/m \approx 10$ eV for most semiconductors. The contribution of remote bands is generally weak, as their contribution is scaled inversely proportional to the energetic difference at the expansion point.

Equation (2.12) can be rewritten to

$$E_n(\boldsymbol{k}) = E'_n(\mathbf{0}) + \frac{\hbar^2 k^2}{2m_n^*}, \text{ with } \frac{m}{m_n^*} = 1 + \frac{2}{mk^2} \sum_{l \neq n} \frac{|\langle u_{n\mathbf{0}} | \boldsymbol{k} \cdot \boldsymbol{p} | u_{l\mathbf{0}} \rangle|^2}{E_n(\mathbf{0}) - E_l(\mathbf{0})}, \tag{2.14}$$

which is known as effective mass (m_n^*) approximation. It only results in parabolic bands.

When following along this derivation, one can come to think, that the $\boldsymbol{k} \cdot \boldsymbol{p}$ method generally is an approximation for $\boldsymbol{k} \approx \boldsymbol{k}_0$ and invalid for the remaining Brillouin zone. However, using Löwdin partitioning, it can be shown, that this is not the case and numerical solutions can give a good approximation for a large range of $\boldsymbol{k}$ values.

The idea behind Löwdin partitioning is to bring the Hamiltonian into a block-diagonal form and reduce it's dimensions such that only a very limited subset of all bands and $u_{n\boldsymbol{k}_0}$ states contribute.

The general Hamiltonian $\mathcal{H} = \mathcal{H}^0 + \mathcal{H}^{\boldsymbol{k}\cdot\boldsymbol{p}}$ is transformed into a block-diagonal form (see Figure 2.1)

$$\tilde{\mathcal{H}} = \mathrm{e}^{-S} \mathcal{H} \mathrm{e}^{S}, \tag{2.15}$$

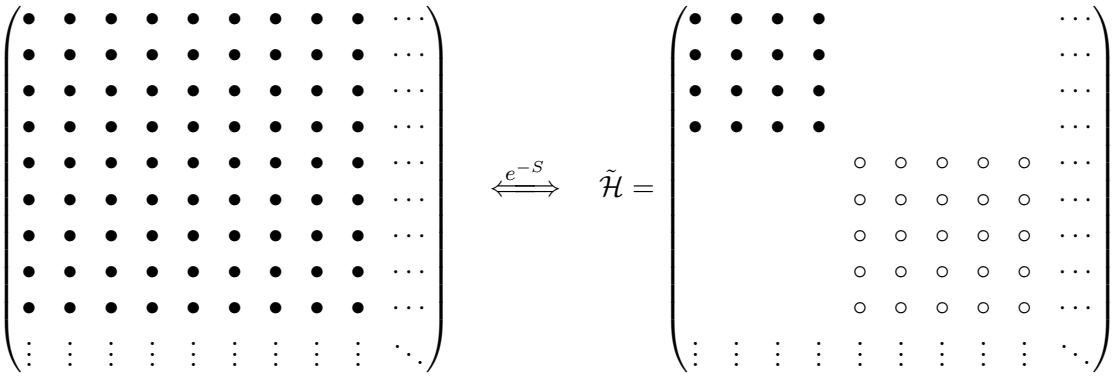

Fig. 2.1.: Löwdin partitioning transforms a Hamiltonian $\mathcal{H}$ into a block-diagonal form $\tilde{\mathcal{H}}$ which separates a subset of states (filled circles) from the remaining states (open circles). The subsequent diagonalization of the finite subset remains as numerical task. Adapted from [40].

using a unitary operator e^S expanded in a series:

$$\mathrm{e}^S = 1 + S + \frac{1}{2!}S^2 + \frac{1}{3!}S^3 + \dots \tag{2.16}$$

By requiring the non-block-diagonal part of $\tilde{\mathcal{H}}$ to be zero, one obtains a set of equations for the construction of S up to the desired order, a process which is explained in detail in Appendix B of [40]. This is used to approximate the block-diagonal

$$\tilde{\mathcal{H}} = \mathcal{H}^{(0)} + \mathcal{H}^{(1)} + \mathcal{H}^{(2)} + \dots, \tag{2.17}$$

with the following evaluation, given up to second order [40]:

$$\mathcal{H}^{(0)}_{mm'} = \mathcal{H}^{0}_{mm'} \tag{2.18}$$

$$\mathcal{H}^{(1)}_{mm'} = \mathcal{H}^{\boldsymbol{k}\cdot\boldsymbol{p}}_{mm'} \tag{2.19}$$

$$\mathcal{H}^{(2)}_{mm'} = \frac{1}{2}\sum_{l} \mathcal{H}^{\boldsymbol{k}\cdot\boldsymbol{p}}_{ml}\mathcal{H}^{\boldsymbol{k}\cdot\boldsymbol{p}}_{lm'}\left[\frac{1}{E_m - E_l} + \frac{1}{E_{m'} - E_l}\right] \tag{2.20}$$

Here m, m' denote matrix indices linked to the subspace of states that are used explicitly in the approximation, whereas l denotes indices for states that are connected to remote bands.

Note that in first order approximation the reduced Hamiltonian $\tilde{\mathcal{H}}$ is essentially just a selection of bands from the original, full Hamiltonian. Starting with the second order additional terms enter the reduced Hamiltonian. They describe the interaction of the bands selected for the $\boldsymbol{k}\cdot\boldsymbol{p}$ model with remote bands and can, in analogy to eq. (2.12), be expressed in terms of material parameters.

Since the energy difference of the bands at the expansion point $\boldsymbol{k}_0$ scales the contribution of higher order terms, they become less important when the energetic splitting of the remote bands is large enough. As the evaluation of $\mathcal{H}^{\boldsymbol{k}\cdot\boldsymbol{p}}_{mm'}$ scales with $\boldsymbol{k}$, the approximation is still better for small $\boldsymbol{k}$ values. Compared to eq. (2.12), a derivation using Löwdin partitioning is, however, not an approximation in orders of k and generally takes higher orders of k into account.

Numerical diagonalization of the $\tilde{\mathcal{H}}$ matrix for discrete values of $\boldsymbol{k}$ will yield the eigenenergies and eigenstates in terms of the c_{nl} weights of $u_{l\boldsymbol{k}_0}$ basis Bloch orbitals (eq. (2.5)) at those points. For derivations of analytical solutions, higher orders of k in $\tilde{\mathcal{H}}$ usually need to be neglected. Reference [39] shows a step by step derivation of such expressions for gallium arsenide valence bands.

8×8 Kane Hamiltonian

For mercury cadmium telluride materials, the important basis orbitals in the vicinity of the Γ-point band gap are the orbitals

$$
\begin{aligned}
|1\rangle &= |\Gamma_6, +\tfrac{1}{2}\rangle = |S, \uparrow\rangle, \\
|2\rangle &= |\Gamma_6, -\tfrac{1}{2}\rangle = |S, \downarrow\rangle, \\
|3\rangle &= |\Gamma_8, +\tfrac{3}{2}\rangle = \tfrac{1}{\sqrt{2}}|X + iY, \uparrow\rangle, \\
|4\rangle &= |\Gamma_8, +\tfrac{1}{2}\rangle = \tfrac{1}{\sqrt{6}}\left[|X + iY, \downarrow\rangle - 2|Z, \uparrow\rangle\right], \\
|5\rangle &= |\Gamma_8, -\tfrac{1}{2}\rangle = -\tfrac{1}{\sqrt{6}}\left[|X - iY, \uparrow\rangle + 2|Z, \downarrow\rangle\right], \\
|6\rangle &= |\Gamma_8, -\tfrac{3}{2}\rangle = -\tfrac{1}{\sqrt{2}}|X - iY, \downarrow\rangle, \\
|7\rangle &= |\Gamma_7, +\tfrac{1}{2}\rangle = \tfrac{1}{\sqrt{3}}\left[|X + iY, \downarrow\rangle + |Z, \uparrow\rangle\right], \\
|8\rangle &= |\Gamma_7, -\tfrac{1}{2}\rangle = \tfrac{1}{\sqrt{3}}\left[|X - iY, \uparrow\rangle - |Z, \downarrow\rangle\right].
\end{aligned}
\tag{2.21}
$$

The first notation is simply an arbitrary numbering of orbitals. The second notation gives the orbital names following the double group notation as first component. The second component denotes the total angular momentum of the orbital. Finally, in the third notation ↑ and ↓ represent the electron spin. In analogy to the atomistic approach $|X\rangle, |Y\rangle, |Z\rangle$ and $|S\rangle$ stand for p- and s-like symmetry wave functions, respectively.

A Hamiltonian treating the interactions between a similar set of orbital bands exactly in diamond and zinc-blende lattice materials was first used by Kane [44], giving this class of Hamiltonians their name. This work uses the following Kane Hamiltonian as basis, with the addition of further terms describing Zeeman interaction, strain [32, 45] and optionally bulk inversion asymmetry (BIA) [40].

$$
H = \begin{pmatrix}
T & 0 & -\frac{1}{\sqrt{2}}Pk_+ & \sqrt{\frac{2}{3}}Pk_z & \frac{1}{\sqrt{6}}Pk_- & 0 & -\frac{1}{\sqrt{3}}Pk_z & -\frac{1}{\sqrt{3}}Pk_- \\
0 & T & 0 & -\frac{1}{\sqrt{6}}Pk_+ & \sqrt{\frac{2}{3}}Pk_z & \frac{1}{\sqrt{2}}Pk_- & -\frac{1}{\sqrt{3}}Pk_+ & \frac{1}{\sqrt{3}}Pk_z \\
-\frac{1}{\sqrt{2}}Pk_- & 0 & U+V & -S_- & R & 0 & \frac{1}{\sqrt{2}}S_- & -\sqrt{2}R \\
\sqrt{\frac{2}{3}}Pk_z & -\frac{1}{\sqrt{6}}Pk_- & -S_-^\dagger & U-V & C & R & \sqrt{2}V & -\sqrt{\frac{3}{2}}\tilde{S}_- \\
\frac{1}{\sqrt{6}}Pk_+ & \sqrt{\frac{2}{3}}Pk_z & R^\dagger & C^\dagger & U-V & S_+^\dagger & -\sqrt{\frac{3}{2}}\tilde{S}_+ & -\sqrt{2}V \\
0 & \frac{1}{\sqrt{2}}Pk_+ & 0 & R^\dagger & S_+ & U+V & \sqrt{2}R^\dagger & \frac{1}{\sqrt{2}}S_+ \\
-\frac{1}{\sqrt{3}}Pk_z & -\frac{1}{\sqrt{3}}Pk_- & \frac{1}{\sqrt{2}}S_-^\dagger & \sqrt{2}V & -\sqrt{\frac{3}{2}}\tilde{S}_+^\dagger & \sqrt{2}R & U-\Delta & C \\
-\frac{1}{\sqrt{3}}Pk_+ & \frac{1}{\sqrt{3}}Pk_z & -\sqrt{2}R^\dagger & -\sqrt{\frac{3}{2}}\tilde{S}_-^\dagger & -\sqrt{2}V & \frac{1}{\sqrt{2}}S_+^\dagger & C^\dagger & U-\Delta
\end{pmatrix}
\tag{2.22}
$$

where colored terms scale with $k_\pm = k_x \pm ik_z$, k_+k_- and $k_\pm^2$.

Material	E_c(eV)	E_v(eV)	E_P(eV)	Δ(eV)	F	γ_1	γ_2	γ_3	κ
HgTe	−0.303	0	18.8	1.08	0	4.1	0.5	1.3	−0.4
CdTe	1.036	−0.570	18.8	0.91	−0.09	1.47	−0.28	0.03	−1.31

Table 2.1.: $\boldsymbol{k}\cdot\boldsymbol{p}$ band parameters used in this work. The Kane matrix element is expressed as $E_P = 2m_0P^2/\hbar^2$. Values and interpolation scheme for HgCdTe materials taken from [32].

The short hand notation terms in the Hamiltonian are resolved to

$$\begin{aligned}
T &= E_c + \frac{\hbar^2}{2m_0}\left((2F+1)k_+k_- + k_z(2F+1)k_z\right),\\
U &= E_v - \frac{\hbar^2}{2m_0}\left(\gamma_1 k_+k_- + k_z\gamma_1 k_z\right),\\
V &= -\frac{\hbar^2}{2m_0}\left(\gamma_2 k_+k_- - 2k_z\gamma_2 k_z\right),\\
R &= -\frac{\hbar^2}{2m_0}\left(\sqrt{3}\mu k_+^2 - \sqrt{3}\bar{\gamma}k_-^2\right),\\
S_\pm &= -\frac{\hbar^2}{2m_0}\sqrt{3}k_\pm\left(\{\gamma_3, k_z\} + [\kappa, k_z]\right),\\
\tilde{S}_\pm &= -\frac{\hbar^2}{2m_0}\sqrt{3}k_\pm\left(\{\gamma_3, k_z\} - \tfrac{1}{3}[\kappa, k_z]\right),\\
C &= \frac{\hbar^2}{m_0}k_-[\kappa, k_z],\\
\mu &= \tfrac{1}{2}(\gamma_3 - \gamma_2),\\
\bar{\gamma} &= \tfrac{1}{2}(\gamma_3 + \gamma_2),
\end{aligned} \tag{2.23}$$

with the conduction and valence band energies $E_{c/v}$ at the Γ point, the Kane matrix element $P = -\frac{\hbar}{m_0}\langle S|p_x|X\rangle$, $F = \frac{1}{m_0}\sum_j^{\Gamma_5}\frac{|\langle S|p_x|u_j\rangle|^2}{E_c - E_j}$ and the spin-orbit split-off parameter Δ. κ and the Luttinger parameters $\gamma_{1,2,3}$ define the valence bands including anisotropy. For an isotropic axial-symmetry model, neglecting valence band warping, μ is simply set to zero. Taking this term into account leads to a non-axial, cubic symmetry. $\{A, B\}$ and $[A, B]$ represent the usual (anti-)commutators.

The Hamiltonian above is given for the case where the layer growth direction coincides with the [0 0 1] crystal direction, i.e. the z axis. For such a growth direction, the Hamiltonian has the highest possible symmetry. For lower symmetry growth directions, additional off-diagonal coupling terms are required in the Hamiltonian. As all samples investigated in this work are grown along the [0 0 1] direction, further discussion of these terms is omitted.

The material specific band parameters are taken directly into account by fixed numeric values given in table 2.1.

2.1.2. Layered structures

For (thin) layered structures, as investigated in this work, the plane-wave expansion eq. (2.3) is only valid in the two in-layer dimensions. For the out-of-plane, layer-growth dimension there is generally no sufficient periodicity to justify a simple plane-wave expansion, as material parameters change abruptly at the layer boundaries. The spacial confinement of the wave

function in a thin layer splits the bulk bands into sub-bands, separated by the confinement energy.

Previous extended discussions in literature [46, 47, 48, 49, 50, 51] have shown, that the envelope-function approximation (EFA) serves to describe such structures accurately. Instead of a plane-wave expansion, the quickly oscillating Bloch functions are modulated by a slowly varying[4] envelope function along the layer-growth direction, labeled z from here on. With this expansion, eq. (2.3) now reads

$$\Psi_n(\boldsymbol{r}) = \sum_{\boldsymbol{k}} F_n(\boldsymbol{r}) u_{n\boldsymbol{k}}(\boldsymbol{r}) = \sum_{\boldsymbol{k}} \exp(ik_x x) \exp(ik_y y) f_n(z) u_{n\boldsymbol{k}}(\boldsymbol{r}). \tag{2.24}$$

As in the bulk case, inserting this new expansion into eq. (2.2) yields the $\boldsymbol{k}\cdot\boldsymbol{p}$ Hamiltonian eq. (2.4), but the derivative with respect to the z coordinate can not be resolved to k_z from a plane-wave component. Thus, powers of k_z in eq. (2.4) and the Kane Hamiltonian eq. (2.22) are replaced with respective orders of derivatives $\frac{\partial f_n(z)}{\partial z}$.

After left-sided multiplication of eq. (2.4) with $u^*_{n\boldsymbol{k}}$, insertion of the expansion eq. (2.5) and real-space integration over a unit cell[5] yields a set of coupled second-order differential equations for the envelope functions $f_n(z)$.

It can be converted into a matrix eigenvalue problem either by expanding $f_n(z) = \sum_i c_n^{(i)} g_i(z)$ in terms of a complete basis set $\{g_i(z)\}$ (e.g. Legendre polynomials up to a certain order [32, 45, 49]), discrete Fourier transformation (FT) combined with quadrature methods [52] or discretization of envelope functions, material parameters and derivatives in z dimension. The Python script collection `kdotpy` [37] used for $\boldsymbol{k}\cdot\boldsymbol{p}$ calculations throughout this thesis utilizes the latter method[6].

2.1.3. Perpendicular magnetic fields and Landau levels

So far, magnetic fields have not been included explicitly in this discussion of the $\boldsymbol{k}\cdot\boldsymbol{p}$ Hamiltonian. Zeeman splitting can be added easily by additional terms in the Hamiltonian with linear magnetic field dependence. But in order to cover the orbital movement of electrons in magnetic fields, one has to exchange the *canonical* momentum $-i\hbar\nabla$ with the *kinetic* momentum $-i\hbar\nabla + e\boldsymbol{A}$. For comparison with a typical magneto-optical experiment in Faraday geometry ($\boldsymbol{B} = (0, 0, B_z)$) a possible vector potential $\boldsymbol{A}$ would be

$$\boldsymbol{A} = \begin{pmatrix} 0 \\ xB_z \\ 0 \end{pmatrix}. \tag{2.25}$$

There is in fact no gauge, that would not include the in-plane dimensions x or y. Therefore, one also gets coupled differential equations for the envelope functions $F_n(\boldsymbol{r})$ also in at least one additional dimension. As described in the previous section, this leads to a multiplicative increase of the basis dimension, which comes at the price of higher computational effort.

In practice [37] it has been proven that a different approach can be used to keep the computational effort lower. For a magnetic field in growth direction as defined above, one can

[4] With respect to the crystal unit cell.

[5] As the envelop function is slowly varying over a unit cell, it can be separated from the integration as constant factor.

[6] This collection is a successor of the original code used in [32, 45] and compatibility of solutions have been verified.

introduce the Landau level ladder operators [32, 40, 45]

$$\begin{aligned} a &= \frac{l_c}{\sqrt{2}} k_- = \frac{l_c}{\sqrt{2}}(k_x - ik_y), \\ a^\dagger &= \frac{l_c}{\sqrt{2}} k_+ = \frac{l_c}{\sqrt{2}}(k_x + ik_y), \end{aligned} \tag{2.26}$$

with $l_c = \sqrt{\frac{\hbar}{eB}}$.

For the Kane Hamiltonian eq. (2.22) in axial symmetry approximation this results in the following LL eigenstate

$$|\Psi^{(N)}\rangle = \begin{pmatrix} \psi_1^{(N)} \,|+\tfrac{1}{2}, n_1 = N\rangle \\ \psi_2^{(N)} \,|-\tfrac{1}{2}, n_2 = N+1\rangle \\ \psi_3^{(N)} \,|+\tfrac{3}{2}, n_3 = N-1\rangle \\ \psi_4^{(N)} \,|+\tfrac{1}{2}, n_4 = N\rangle \\ \psi_5^{(N)} \,|-\tfrac{1}{2}, n_5 = N+1\rangle \\ \psi_6^{(N)} \,|-\tfrac{3}{2}, n_6 = N+2\rangle \\ \psi_7^{(N)} \,|+\tfrac{1}{2}, n_7 = N\rangle \\ \psi_8^{(N)} \,|-\tfrac{1}{2}, n_8 = N+1\rangle \end{pmatrix} \tag{2.27}$$

Where $N = -2, -1, 0, 1, \ldots$[7] is the $|\Psi^{(N)}\rangle$ eigenstate's LL number, $\psi_i^{(N)}$ are the envelop functions for each LL N and orbital i (see eq. (2.21)) and $|n_i\rangle$ is the LL state of each orbital upon which the $a^\dagger, a$ ladder operators act like

$$\begin{aligned} a^\dagger a \,|n\rangle &= n \,|n\rangle\,, \\ a \,|n\rangle &= \sqrt{n} \,|n-1\rangle\,, \\ a^\dagger \,|n\rangle &= \sqrt{n+1} \,|n+1\rangle\,. \end{aligned} \tag{2.28}$$

In the axial approximation the LL quantum number N is a conserved quantity (i.e. a "good" quantum number) and each LL Hamiltonian can be solved separately. Outside of the axial approximation, the μk_+^2 term in R (eq. (2.23)) couples Landau levels N with $N+4, N+8, \ldots$ and the true eigenstate of the non-axial, cubic Hamiltonian has contributions from every fourth LL[8]. Typically only one or two different LLs dominate the eigenstate. In this case, the total Hamiltonian is not block diagonal for different LLs anymore[9] and in principle infinite dimensional. However, for most applications it is sufficient to only consider LLs up to a certain number. Only in low magnetic fields, where LLs for very high numbers are filled, this leads to inaccurate description of the real system.

Note, that even in the cubic approximation the Hamiltonian is still dividable into four individual parts, corresponding to the four sets of coupled LLs. The quantity N mod 4 is conserved in this level of symmetry.

[7] The eigenstates are constructed in a way that for each orbital component the sum of the total angular momentum and n (which also carries $\hbar n$ angular momentum) is equal. Starting the LL count at $N = -2$ follows the usual convention to have $n = N$ for the $+\frac{1}{2}$ orbital [40].

[8] The coupling of LLs is directly linked to the m-fold axial rotational symmetry C_m of the Hamiltonian, inducing couplings between N and $N+nm$ ($n \in \mathbb{N}$) [45, 53]. In this case it is reduced to a fourfold rotational symmetry (plus translation).

[9] While this leads to drastically reduced performance of numerical eigensolvers, it is still faster than solving a similar system in k-space [37].

2.1.4. Bulk inversion asymmetry

The Kane Hamiltonian presented so far does not take into account that zinc-blende type materials have two distinct chemical elements at the atomic lattice. Compared to the single element diamond type lattice, this breaks the inversion symmetry of the system. Since this asymmetry is caused by the microscopic properties of the material bulk itself, this effect is called bulk inversion asymmetry (BIA).

As broken symmetries come with additional coupling terms, the Kane Hamiltonian eq. (2.22) so far is extended by adding

$$H_{\mathrm{BIA}} = \begin{pmatrix} 0 & H_{6c,8v} & H_{6c,7v} \\ H_{6c,8v}^{\dagger} & H_{8v,8v} & H_{8v,7v} \\ H_{6c,7v}^{\dagger} & H_{8v,7v}^{\dagger} & 0 \end{pmatrix}, \tag{2.29}$$

where the individual block matrices are defined as follows [40]:

$$H_{6c,8v} = \begin{pmatrix} \frac{1}{\sqrt{2}}B_8^+ k_- k_z & \frac{1}{2\sqrt{6}}\left((B_8^+ - B_8^-)k_+^2 - (B_8^+ + B_8^-)k_-^2\right) & \frac{1}{\sqrt{6}}B_8^+ k_+ k_z & \frac{1}{3\sqrt{2}}B_8^-(2k_z^2 - k_+k_-) \\ -\frac{1}{3\sqrt{2}}B_8^-(2k_z^2 - k_+k_-) & \frac{1}{\sqrt{6}}B_8^+ k_- k_z & \frac{1}{2\sqrt{6}}\left((B_8^+ + B_8^-)k_+^2 - (B_8^+ - B_8^-)k_-^2\right) & \frac{1}{\sqrt{2}}B_8^+ k_+ k_z \end{pmatrix} \tag{2.30}$$

$$H_{6c,7v} = \frac{B_7}{\sqrt{3}} \begin{pmatrix} -\frac{1}{4}(k_+^2 - k_-^2) & -k_+ k_z \\ k_- k_z & \frac{1}{4}(k_+^2 - k_-^2) \end{pmatrix} \tag{2.31}$$

$$H_{8v,8v} = \frac{C_8}{2} \begin{pmatrix} 0 & -k_+ & 2k_z & -\sqrt{3}k_- \\ -k_- & 0 & \sqrt{3}k_+ & -2k_z \\ 2k_z & \sqrt{3}k_- & 0 & -k_+ \\ -\sqrt{3}k_+ & -2k_z & -k_- & 0 \end{pmatrix} \tag{2.32}$$

$$H_{8v,7v} = \frac{C_8}{2\sqrt{2}} \begin{pmatrix} k_+ & 2k_z \\ 0 & -\sqrt{3}k_+ \\ \sqrt{3}k_- & 0 \\ 2k_z & -k_- \end{pmatrix} \tag{2.33}$$

Note: Reference [40] presents the 8×8 Kane Hamiltonian including BIA terms in explicit matrix form in Table C.8. Here the sign of B_8^- is flipped with respect to the definitions given in Tables C.5 and 6.2.

As BIA also reduces the symmetry with respect to the magnetic field axes down to a two-fold rotational symmetry (still assuming growth and magnetic field directions along the z-axis), the coupling in the LL description also increases. Eigenstates of the model including BIA are now built from every second LL. This can again also be seen from the H_{BIA} elements themselves, which couple now also LL states with quantum number N to those with $N \pm 2$. In analogy to the cubic case, the Hamiltonian and the eigenstates can now be divided into two separate sets and N mod 2 is now a conserved quantity.

2.1.5. Structure inversion asymmetry

The macroscopic structure itself can give also give rise to asymmetry along the growth direction. This is called structure inversion asymmetry (SIA). In the 8×8 Kane Hamiltonian such an

Material	C_8 (meV nm)	B_8^+ (meV nm^2)	B_8^- (meV nm^2)	B_7 (meV nm^2)
HgTe	−7.40	−106.46	13.77	−100.0
CdTe	−2.34	−224.1	−6.347	−204.7

Table 2.2.: BIA parameters used in this work. CdTe values are taken from [40], whereas HgTe values are derived from a yet unpublished density functional theory calculation conducted by Dr. Domenico Di Sante (TP1, JMU Würzburg). The validity of these parameters has been investigated as part of a Bachelor thesis by Moritz Siebert under supervision of the author (see also section 5.2.4). Interpolation for HgCdTe materials is linear.

effect is introduced as asymmetric, z-dependent electron potential on the matrix diagonal. This covers sources like electrostatic potentials from gate structures and inhomogeneous charge carrier distribution, as well as potential asymmetries of confinement potentials given by the layer stack itself (e.g. different barrier materials). The confinement is already included in eq. (2.22) via the material parameters $E_{c|v}$.

Note, that the $k = 0$ spin splitting effect caused by this asymmetry is also commonly known as Rashba splitting. However, this term is generally only linked to effective models exclusively for the conduction bands. Such a simplified model can be derived from a Kane Hamiltonian by means of Löwdin partitioning [40], which gives rise to the effective Rashba splitting parameter α and an addition to the simplified Hamiltonian by terms linear in $k_\pm$. This additional Rashba term only compensates for the missing interaction between conduction and valence bands in the simplified model. When SIA is included in the 8×8 Kane Hamiltonian, such a splitting parameter is not necessary, as the interactions are taken into account for explicitly.

2.1.6. Interface inversion asymmetry

Another possible source of asymmetry is given by the microscopical termination of each material layer. As an example, for the mercury telluride samples, the layer can be interfacing to the barrier layers with either mercury or tellurium atoms, which can give rise to an asymmetric situation at the two interfaces.

However, we have no means to determine the actual situation at such interfaces. Also, for thick layers, the wavefunctions generally extend much less into the barriers, so this influence can be considered less important in this case, as compared to the situation in narrow quantum wells.

Furthermore, the microscopic asymmetry can be approximated by localized interface potentials and therefore influences the Hamiltonian in the same way as SIA [40]. Interface inversion asymmetry will therefore not be separately discussed further in this thesis.

2.1.7. In-plane magnetic fields

Other than perpendicular magnetic fields, as discussed in section 2.1.3, field components inside the layer dimensions x, y fully break the rotation symmetry around the growth direction. This leads to coupling of LLs with quantum number N to those with $N \pm 1$ (linear B scaling) and $N \pm 2$ (quadratic B scaling).

Other than for out-of-plane fields, the in-plane field gauge can be chosen such that there is no explicit x or y dependency added to the Hamiltonian by introduction of the *kinetic* momentum $-i\hbar\nabla + e\boldsymbol{A}$, e.g.:

$$\boldsymbol{A} = \begin{pmatrix} zB_y \\ -zB_x \\ 0 \end{pmatrix} \tag{2.34}$$

Since an explicit z dependence of the Hamiltonian is already present due to the envelope function approximation, there is no further dimension required to incorporate in-plane fields into $\boldsymbol{k}$ dispersion or LL magnetic field dependence studies.

Assuming a small tilt of the magnetic field axis by just one degree with respect to the growth direction, the in-plane field component at a total magnetic field of 6 T already exceeds 0.1 T. However, test calculations using a 45 nm thick mercury telluride layer yields only few additional LL band crossings being avoided with an energy splitting on the order of 0.2 meV and no further notable differences to a model involving BIA.

Under realistic experimental conditions, the tilt of the magnetic field axis is not known to suitable precision and varies between different measurements. For the spectra discussed during this work, the influence of in-plane fields is further not resolvable. Thus, in-plane field components are ignored in this work. Note however, that the additional avoided crossing is crucial to understand the LL fan charts acquired by magneto-transport experiments at dilution fridge temperatures well below 4 K.

2.2. Optical transitions and spectra

This section derives the transition matrix from the Hamiltonian. This matrix is used to calculate the strength of transitions between two LL states and the resulting ellipticity spectra expected from an optical polarimetry measurement. The code of `kdotpy` [37] has been rewritten by the author to correctly calculate optical spectra, following this derivation[10].

2.2.1. Perturbation Hamiltonian for electromagnetic waves

Starting out from the $k \cdot p$ Hamiltonian describing the sample band structure in static electric and magnetic fields, the influence of electromagnetic (EM) waves is treated by another perturbative ansatz.

$$\begin{aligned} H_{\mathrm{pert}} &= \frac{(\boldsymbol{p} + e\boldsymbol{A})^2}{2m} + V \\ &= \frac{(\boldsymbol{p} + e\boldsymbol{A}_0 + e\boldsymbol{A}_{\mathrm{EM}})^2}{2m} + V \\ = H + H_{\mathrm{EM}} &= \left[\frac{(\boldsymbol{p} + e\boldsymbol{A}_0)^2}{2m} + V\right] + \left[\frac{e\boldsymbol{A}_{\mathrm{EM}} \cdot \boldsymbol{p}}{m}\right] \end{aligned} \tag{2.35}$$

where the vector potential $\boldsymbol{A}$ is split into the static part A_0 of the electric and magnetic fields applied to the `kdotpy` eigenstate calculation from H_0 and $\boldsymbol{A}_{\mathrm{EM}} = \frac{\boldsymbol{E}}{\omega}\cos(\omega t - \boldsymbol{q}\cdot\boldsymbol{r})$ for the EM wave. The identity $\boldsymbol{p}\cdot\boldsymbol{A} = \boldsymbol{A}\cdot\boldsymbol{p}$ valid for divergence free fields of EM waves is used and the energy offset terms $\boldsymbol{A}_{\mathrm{EM}}^2 + 2\boldsymbol{A}_0 \cdot \boldsymbol{A}_{\mathrm{EM}}$ are neglected.

Using the dipole approximation ($\frac{c}{2\pi\omega} = \lambda \gg r$ or $\vec{q} \to 0$) and Euler's formula $\boldsymbol{A}_{\mathrm{EM}}$ can be rewritten

[10] The derivation given here has been written by the author as part of the documentation wiki for the `kdotpy` project in a similar form.

$$\boldsymbol{A}_{\mathrm{EM}} = \frac{\boldsymbol{E}}{2\omega}\left(e^{-i\omega t} + \text{c.c.}\right) \tag{2.36}$$

The time-varying phase factor and its complex conjugate can be identified as the two terms responsible for positive and negative frequencies in Fermi's Golden Rule. These can be connected to absorption and emission processes. With this definitions in mind, the notation can be simplified by dropping the time-varying phase factor altogether from here on. It is useful to write $\boldsymbol{E}$ in a circular basis[11]

$$\boldsymbol{E} = \begin{pmatrix} E_x \\ E_y \\ E_z \end{pmatrix} = \frac{1}{\sqrt{2}}\left(E_+ \begin{pmatrix} 1 \\ i \\ 0 \end{pmatrix} + E_- \begin{pmatrix} 1 \\ -i \\ 0 \end{pmatrix} \right) + E_z \begin{pmatrix} 0 \\ 0 \\ 1 \end{pmatrix}, \tag{2.37}$$

equivalent to the definition $E_\pm = \frac{1}{\sqrt{2}}\left(E_x \mp iE_y\right)$. Thus the above vector product can be written as

$$\begin{aligned} \boldsymbol{E}\cdot\boldsymbol{p} &= E_x p_x + E_y p_y + E_z p_z \\ &= \tfrac{1}{\sqrt{2}}(E_+ p_+ + E_- p_-) + E_z p_z \end{aligned} \tag{2.38}$$

with the usual definition $p_\pm = p_x \pm ip_y$. For light incident along the layer growth direction (i.e. perpendicular to the sample surface) E_z is zero and following derivation can be restricted to the x, y plane and $\pm$ components.

2.2.2. Transition matrix elements

Since the commutator $[H, H_{\mathrm{EM}}]$ does not vanish, both Hamiltonians do not have the same eigenstates and H_{EM} will introduce transitions between eigenstates of H.

To simplify the notation, the operator $O = H_{\mathrm{EM}}$ is introduced, written in terms of the velocity operator $\boldsymbol{v} = \boldsymbol{p}/m$ and using eq. (2.38).

$$\begin{aligned} O = O_+ + O_- = O_x + O_y &= \frac{e}{2\omega}\left(E_x v_x + E_y v_y\right) \\ O_\pm &= \frac{e}{2\sqrt{2}\omega} E_\pm v_\pm \end{aligned} \tag{2.39}$$

As the operator can be written as sum velocity operators weighted by the respective electric field components in both linear and circular polarization basis, the effect of EM waves polarized in terms of one of these basis states can be analyzed separately.

The transition rate $\Gamma_{i\to f}$ from initial state $|\psi_i\rangle$ to final state $|\psi_f\rangle$ is given by Fermi's Golden Rule

$$\Gamma_{i\to f} = \frac{2\pi}{\hbar}\left|M^{(fi)}\right|^2 \delta(\hbar\omega_{fi} - \hbar\omega), \tag{2.40}$$

with the transition matrix element

$$\begin{aligned} M^{(fi)} &= \langle\psi_f|O|\psi_i\rangle \\ &= \frac{e\boldsymbol{E}}{2\omega}\langle\psi_f|\boldsymbol{v}|\psi_i\rangle \end{aligned} \tag{2.41}$$

[11] The electric field components carry a complex phase describing the full polarization state.

where energy conservation is given by $\hbar\omega = \hbar\omega_{fi} = E_f - E_i$, assuming delta-peak sharp energy levels. The explicit time dependence of the electric field is not present in the matrix element, as this part is responsible for the δ distribution in eq. (2.40).

With the definition

$$v_x = -\tfrac{i}{\hbar}[x, H_{\text{pert}}] \approx -\tfrac{i}{\hbar}[x, H] = \frac{\mathrm{d}H}{\mathrm{d}p_x} = \frac{\mathrm{d}H}{\mathrm{d}(\hbar k_x)}, \tag{2.42}$$

which holds analogously for the y-direction, the matrix representation $O_k^{(mn)}$ in the orbital basis for each operator component $O_k (k \in x, y, \pm)$ can be written in terms of the Kane Hamiltonian H (eq. (2.22)):

$$\begin{aligned} O_{x,y}^{(mn)} &= \frac{eE_{x,y}}{2\hbar\omega} \frac{\mathrm{d}H^{(mn)}}{\mathrm{d}k_{x,y}}, \\ O_{\pm}^{(mn)} &= \frac{eE_{\pm}}{\sqrt{2}\hbar\omega} \frac{\mathrm{d}H^{(mn)}}{\mathrm{d}k_{\mp}}, \end{aligned} \tag{2.43}$$

where use was made of the identity $\frac{\mathrm{d}}{\mathrm{d}k_\pm} = \frac{\mathrm{d}k_x}{\mathrm{d}k_\pm}\frac{\mathrm{d}}{\mathrm{d}k_x} + \frac{\mathrm{d}k_y}{\mathrm{d}k_\pm}\frac{\mathrm{d}}{\mathrm{d}k_y} = \frac{1}{2}\left(\frac{\mathrm{d}}{\mathrm{d}k_x} \mp i\frac{\mathrm{d}}{\mathrm{d}k_y}\right)$.

`kdotpy` uses a symbolic representation of the Hamiltonian with respect to $k_\pm$ and the required operators can obtained efficiently. After evaluation of the vector-matrix-vector product eq. (2.41) for all calculated eigenvectors, the transition rate $\Gamma_{i\to f}$ is multiplied by the state density and the states occupation factor $P_{i\to f}$.

The occupation factor required to calculate the effective photon absorption is given by

$$\begin{aligned} P_{i\to f} &= P_{fi} - P_{if} \\ &= f(E_i)\cdot(1 - f(E_f)) - f(E_f)\cdot(1 - f(E_i)) \\ &= f(E_i) - f(E_f), \end{aligned} \tag{2.44}$$

where the first term P_{fi} describes absorption as transition from a filled initial state with energy E_i to an empty state at higher energy E_f and the second term is contributed by stimulated emission with flipped roles of final and initial energies (which is in this case expressed by flipped indices). Note that this notation reduces the double sum over all indices f and i to a single summation over pairs of states (f, i) where $E_f > E_i$, which is easier to handle numerically.

2.2.3. Action of transition operator on Landau level states

Spectra of magneto-optical measurements are calculated from eigenstates computed in `kdotpy`'s LL mode. The eigenstate basis is changed to Landau level states $|\Psi^{(N)}\rangle$ as defined by eq. (2.27).

The action of the transition operator $O_\pm$ on $|\Psi^{(N)}\rangle$ can be quickly worked out from the color coded Kane Hamiltonian in eq. (2.22). After derivation with respect to $k_\mp$, all remaining terms in the matrix scale with $k_\pm$, $k_\mp$ or are constant with respect to $k_\pm$.

In the LL representation $k_\pm$ terms in the Hamiltonian are replaced by ladder operators $(k_-, k_+) \to (a, a^\dagger)$ acting on the orbital LL quantum numbers $n_i (i \in [1, 8])$.

Thus $k_\pm$ terms in the main-diagonal elements of the operator do not change the orbital character of the eigenstate, but change the orbital LL n_i by $\Delta n = \pm 1$.

Terms without ladder operators do not change the orbital LLs at all, but change the orbital character in a way such that total angular momentum j changes by $\Delta j = \pm 1$.

Finally, the R term couples orbitals with $\Delta j = \pm 2$. In the axial approximation the remaining ladder operator introduces changes of $\Delta n = \mp 1$. The cubic term, scaling with μk_+^2 in eq. (2.23), does causes the opposite $\Delta n = \pm 1$.

In the axial approximation the operator product of two states $\langle \Psi^{(M)} | O_\pm | \Psi^{(N)} \rangle$ has thus only non-zero value if $M = N \pm 1$. Hence the usual selection rule $\Delta N = \pm 1$ for the eigenstate LL number N holds.

This is also in line with conservation rules: As the transition between LL states requires energy, a photon must be absorbed to provide the required energy. As the kinetic momentum of the massless photon is only a small fraction of the crystals Brillouin zone, it's contribution can be neglected. However, the photon also carries spin angular momentum $s = \pm 1$ associated with circular polarized light $E_\pm$. The angular momentum operator for Landau levels $L_z = \hbar \left(a^\dagger a - b^\dagger b \right)$ associates a change of $\Delta n = \pm 1$ also with a change of angular momentum of $\pm\hbar$.

A transition in the axial approximation therefore conserves the total angular momentum by absorption of a photon and the combined increase or decrease of total angular momentum of the orbital character and orbital LL quantum number n.

Outside of the axial approximation the $\Delta N = \pm 1$ selection rule is broken and more transitions are enabled by the $O_\pm$ operator. While this is covered in the numerical calculation, the strength of additional transitions allowed by this effect is small enough to be irrelevant for analysis under the conditions of this thesis. A much higher effect on the strength and additional occurrence of the transitions is given by the intermixing of LL basis states in the eigenstates of asymmetric models. As angular momentum is not a conserved quantity without axial symmetry of the model, there is also no conversation of angular momentum for transitions in such cases.

2.2.4. Calculation of spectra

Absorption

From Fermi's Golden Rule one obtains a transition rate between initial and final states (see eq. (2.40)) where each transition absorbs a photon with energy $\hbar\omega$. Therefore, $\Gamma_{i\to f} \cdot G \cdot P_{i\to f}$ is a photon absorption rate density (with degeneracy area density of LL states $G = \frac{eB}{2\pi\hbar}$).

From these results, the 2D absorption coefficient α_{2D} may be calculated directly using the three above defined quantities [40]. As derivations of absorption coefficients from $\boldsymbol{k} \cdot \boldsymbol{p}$ theory calculations are often given in the context of k resolved bulk calculations [39] or do not use SI units throughout, a short derivation suitable for the calculation type employed in this work is given in the following.

Since `kdotpy` calculates the eigenvectors on a discrete grid along growth direction z, the number of eigenvector elements is equal to the number of basis orbitals (eight in this work) times the number of grid points. The eigenvectors and the calculation of the matrix element may be decomposed into the orbital and spatial parts.

Within each finite grid element Δz the partial vector product sum over the orbital components in $\langle \psi_f | O | \psi_i \rangle$ yields the local transition rate $\gamma_{i\to f}$ within the grid element. Multiplying the local photon absorption rate density with the photon energy $\hbar\omega$ yields the local energy absorption rate per volume:

$$\frac{dI}{dt} = -\gamma G P \hbar\omega \tag{2.45}$$

$$= \frac{dI}{dz}\frac{dz}{dt} = -\frac{c}{n}\alpha I \tag{2.46}$$

with refractive index[12] $n = \sqrt{\epsilon_r \mu_r}$. c is the speed of light in vacuum and $\epsilon_r\epsilon_0$ the (relative) permittivity. Here dropping the index $i \to f$ implies a summation over all possible transitions.I describes the local energy volume density of the electromagnetic wave.

The local energy volume density of the electromagnetic wave I can be calculated from the time-averaged Poynting vector $\boldsymbol{S}$ divided by the propagation speed of the wave as

$$\begin{aligned} I &= \frac{\langle \boldsymbol{S} \rangle}{\frac{c}{n}} \\ &= \tfrac{1}{2}\epsilon_r\epsilon_0|E|^2 \\ &= \tfrac{1}{2}\epsilon_0 n^2 |E|^2, \end{aligned} \tag{2.47}$$

where relative permeability $\mu_r = 1$ is used in the last identity.

Thus, the following differential equation is obtained from equations eq. (2.39) to eq. (2.41) and eq. (2.45) to eq. (2.47):

$$\begin{aligned} -\frac{\frac{dI_\pm}{dz}}{I_\pm} = \alpha_\pm &= \sum_{i,f} G P \hbar\omega \frac{n}{c} \frac{\frac{2\pi}{\hbar}\frac{e^2 E_\pm^2}{8\omega^2}\left|\langle f|v_\pm|i\rangle\right|^2 \delta(\hbar\omega_{fi} - \hbar\omega)}{\frac{1}{2}\epsilon_0 n^2 E_\pm^2} \\ &= \sum_{i,f} G P \frac{e\pi}{2}\frac{e}{\epsilon_0}\frac{1}{cn}\frac{1}{\omega}|v_{\pm,fi}|^2 \delta(\hbar\omega_{fi} - \hbar\omega) \end{aligned} \tag{2.48}$$

Here, the z dependent local absorption factor $\alpha_\pm(z)$ for both circular polarization modes can be identified.

Solving the differential equation eq. (2.48) by integration yields

$$I_\pm(z) = \exp\left(-\int_0^z \alpha_\pm(z')dz'\right) I_\pm(0) \tag{2.49}$$

After traversing the full calculated layer stack with thickness d, the energy density is by definition $I_\pm(d) = \exp\left(-\alpha_\pm^{\mathrm{2D}}\right) I_\pm(0)$. The 2D absorption coefficient is thus the integral over the local absorption factors. As n is assumed to be a constant value with respect to z in this approximation, the integral over local absorption factors is identical to the summation also over the Δz grid elements, when $\langle\psi_f|O_\pm|\psi_i\rangle$ is calculated by `kdotpy`.

We can relate the detected photons to the incident photons of each circular polarization mode by the relative absorption $A_\pm = \frac{I_\pm(d)}{I_\pm(0)} = \exp(-\alpha_\pm^{\mathrm{2D}})$. Note that the values output by `kdotpy` correspond to the 2D absorption coefficient, not relative absorption. Additional transmission loss due to reflection at impedance missmatched interfaces requires the knowledge of the dielectric functions of every layer in the sample and is out of the scope of `kdotpy` and this thesis.

[12] `kdotpy` uses a constant refractive index $n = 21$ [54] here. Strictly, n should also depend on ω, but the dependence is usually considered small [40, 55]. More concerns arise about the validity of the above value, determined in reference [54] for bulk semi-metal crystals, with respect to semiconducting strained thin layers. Nevertheless, this constant only scales the amplitude of calculated ellipticities, not the resonance photon energy, which is the key property of this work.

Ellipticity

As ellipticity ε is defined by $\tan(\varepsilon) = \frac{E_+ - E_-}{E_+ + E_-}$ and $E_\pm \propto \sqrt{I_\pm(d)}$, it can be calculated using $I_+(0) = I_-(0)$ and the definition of the relative absorption $A_\pm$ above:

$$\varepsilon = \arctan\left(\frac{\sqrt{A_+} - \sqrt{A_-}}{\sqrt{A_+} + \sqrt{A_-}}\right) = \arctan\left(\frac{\exp(-\alpha_+^{\mathrm{2D}}/2) - \exp(-\alpha_-^{\mathrm{2D}}/2)}{\exp(-\alpha_+^{\mathrm{2D}}/2) + \exp(-\alpha_-^{\mathrm{2D}}/2)}\right) \tag{2.50}$$

So far there are only delta peaks in the absorption and ellipticity spectrum, but experimental spectra always have a finite linewidth. To obtain a good comparison with experimental spectra the delta peaks of all transitions are broadened by Cauchy-Lorentz distributions to account for natural broadening by finite state lifetimes. Unless noted otherwise a full width at half maximum (FWHM) of 0.4 meV is used for all spectra calculations in this work. Even though the experimental linewidth varies between different samples, the above value is in sufficiently good agreement with most measurements.

Note again that the goal of this works is not in quantitative comparison of ellipticity strength and lineshapes, but rather in determination of the correct models to match energetic position of transition features and general trends as best as possible.

2.2.5. Kubo-Greenwood formula and dielectric functions

Generally, one could also make use of Kubo's formula [56, 57, 58] to calculate the dielectric functions $\epsilon_{xx}, \epsilon_{xy}$ [37, 55] and therefrom e.g. ellipticity and Faraday rotation spectra [59, 60] from the same matrix elements. This requires more eigenstates from a larger energy range around the electro-chemical potential (ECP), such that the sum over all transitions is not cut off at too low optical frequencies. Unfortunately, the calculation of a larger energy range in LL mode ultimately requires both a higher number of basis Landau levels and more eigenstates requested from the Hamiltonian matrix eigensystem solver. As the total calculation time scales linearly with both values, it scales approximately quadratic with the requested energy range. The evaluation of Kubo's formula is thus not considered further along this thesis.

3 Polarization resolved time-domain Terahertz spectroscopy

3.1. Properties of Terahertz radiation

The definition of the term Terahertz radiation is vague and most often given by the photon frequency range of 0.1 to 10 THz, which is equivalent to wavelength ranging from few millimeters down to multiple tens of microns or the energy range from about 0.1 to multiple tens of meV. This regime connects the microwave region, where electronics, cables and waveguides dominate the technical realizations, to the infrared and visible domain, which is exploited using optical elements like lenses, gratings up to dynamical polarization state changing devices like photo-elastic modulators.

The THz region is thus in between two different technologies, but not well covered by any of those two alone. The lack of commercially available sources and sensors with high stability and SNR has started to decrease over the past decade, as this frequency range is also becoming more and more important for high bandwidth communication devices, according to the planned 6G standard.

Nowadays, there exists a range of THz sources like photoconductive antennas, crystals for high harmonics generation, backward wave oscillators, quantum cascade lasers or even free electron lasers. For detection one can choose from photoconductive antennas and calorimetric devices like bolometers or Golay cells, as well as sampling based on the electro-optical effect. Most available tabletop systems with broadband or tuneable frequency output provide a peak SNR up to 100 dB in the range from 0.2 to approximately 5 THz.

For the investigation of surface states of topological insulator materials, the probing photon energy should be smaller than the the bulk bandgap and cover the energetic range of transitions in between or from the topological states. For the strained mercury telluride samples investigated here, the gap between valence and conduction bands is on the order of 20 meV and more, thus THz radiation is a reasonable tool for this thesis.

3.2. Time domain spectroscopy

Compared to continuous wave (CW) approaches the time-domain spectroscopy (TDS) offers some benefits for our thin film polarimetry.

In TDS all information comes from sampling the electrical field of coherent THz pulses. Thus, internal reflections from sufficiently[1] thick layers can be sampled separately. This eliminates a set of challenges that is very important with CW radiation, where standing waves can emerge by reflection from the sample and optical elements in the beam path. By choosing the pulse that arrived first at the detector one can guarantee, that the signal stems from a single transmission through each element without added interference effects[2].

Additionally, these internal reflections (within the sample stack) can be used to investigate effects originating from reflections at layer boundaries [19], as depicted in Figure 3.1. However,

[1] The necessary thickness depends on the refractive index of the layer material and the desired frequency resolution after Fourier transformation. A few hundred µm up to some millimeter thickness is sufficient in most cases.

[2] This does not hold for transmission through thin films with a pulse travel time comparable to the pulse length. In this case more care needs to be taken at data analysis [61].

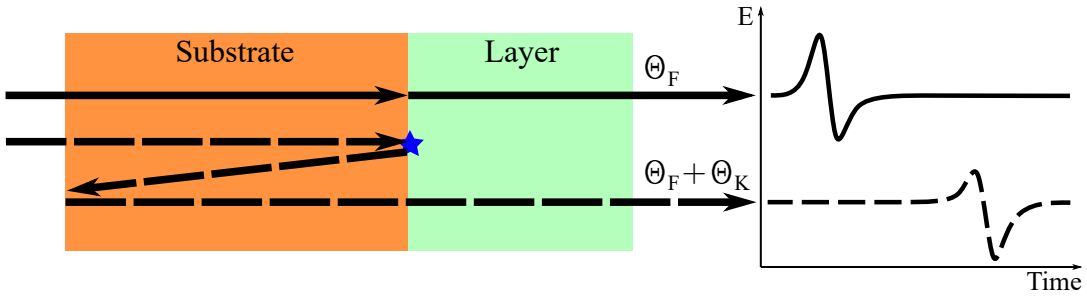

Fig. 3.1.: Working principle for reflection measurements in transmission geometry. If the additional pulse travel time of internal reflections is large than the pulse length, plain transmission (continuous line) and reflected pulses (dashed line) may be measured separately. In the given example the pulse is reflected at the substrate-layer interface (blue star, arrows offset for clarity), picking up a Kerr signal Θ_K in addition to the Faraday signal Θ_F.

in order to clearly separate contributions from different boundaries the layer and substrate thicknesses must be large enough to temporally separate pulses reflected at different interfaces. In case of the material system investigated in this thesis, the mercury telluride layer thickness is too small by multiple orders of magnitude to resolve different boundaries in the signal. As the layer thickness is much smaller than the wavelength, the treatment of interface reflections does not make sense and the layer is treated as an infinitely thin boundary instead[3]. Furthermore, the additional information gained from pulses reflected within the substrate does not yield additional information concerning the energetic position of optical transitions, which is the most relevant information for this work. Furthermore, recording a longer time signal to also cover reflection pulses doubles the overall measurement time, which is already quite long to begin with. For all of these reasons, this work is limited to the investigation of the pure transmission signal only.

FT of the time resolved signal gives frequency resolved amplitude and phase[4] information for the selected pulse. The achievable frequency resolution is fundamentally limited by the length of the acquired time signal.

The basic principle of THz-TDS employs a set of gated antennas, one acting as emitter of the THz pulse and another as receiver that is used to sample the incoming pulse (see Figure 3.2). To this day, all commercially available systems use optical gating via femtosecond laser pulses to activate the antennas. The emitted pulse length t is typically few ps and propagates to the detector in the time T (on the order of ns). Thus, for sampling of the pulse the receiver must be activated at equidistant time intervals Δt between T and $T + t$. This can be done in a pure electro-optical manner by using two asynchronous lasers with slightly different repetition rates [62, 63]. This is called asynchronous optical sampling (ASOPS). It is, however, more common and much cheaper to use one laser and split it's output on separate beam paths for emitter and receiver. A precise mechanical delay stage can then be used to vary the propagation time

[3] This is known as the thin-film or two-dimensional limit.

[4] Most CW methods gain access to the phase only via a Mach-Zehnder interferometer setup, which requires broad band beam splitters and an additional beam path. This further complicates the optical alignment process.

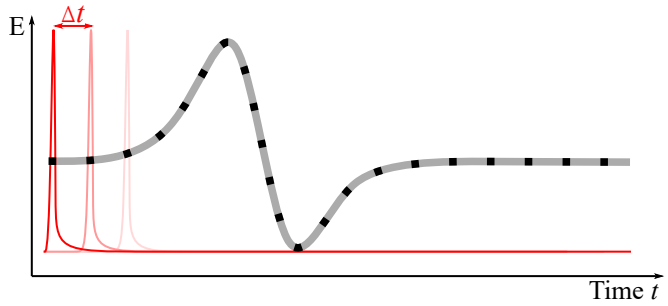

Fig. 3.2.: Sampling of the THz pulse (gray) over the time scale t at discrete time intervals Δt. Each sample point (black dots) is acquired by activation of an electric field sensor via a short optical gating pulse (red colors).

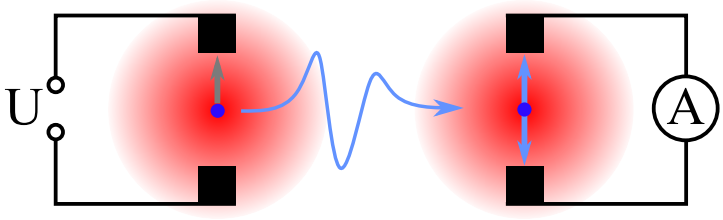

Fig. 3.3.: Sketch of a pair of photoconductive antennas. Laser radiation (red spots) excites charge carriers (blue) in a gap between electric contacts (black rectangles). Carriers are accelerated either by an excitation voltage U (gray arrow) and emit radiation (light blue wave) or by the electric field of incident radiation (light blue arrows) causing a measurable photocurrent.

delay between both paths up to t. Care has to be taken for both variants to set up the laser beam paths with the correct time delay T.

Competing technologies also exist for the antennas: Optical rectification of the gate laser pulse in nonlinear optical crystals can be used to generate THz radiation. It is often paired with detectors based on the Pockels electro-optic effect, where the THz electric field induces birefringence in a crystal. The transmitted gate laser pulse will experience a detectable change of polarization linear to the THz electric field. For both antennas ZnTe can be used a crystal material. This approach typically yields high bandwidth, with acceptable SNR.

Another possibility is the use of photoconductive antennas (PCA, also called Auston switch) for both emitter and detector. As of today, it offers the best SNR in commercially available systems. The setup introduced in this thesis employs PCAs for this very reason. The bandwidth strongly depends on geometric and material parameters of the antenna design, but is typically lower than with optical rectification and electro-optic sampling.

Basically the PCA design is a gapped transmission line on a semiconductor substrate, see Figure 3.3. The gate laser pulse is focused on the gap, exciting charge carriers and bridging the gap.

In case of the emitter the activated carriers (lifetime $\tau \lesssim 1$ ps) are accelerated by a static bias voltage that is supplied by the transmission line. This emits the THz pulse in a radially broad distribution comparable to dipole radiation which is focused by an attached high resistivity float zone (HRFZ) Si lens. The emitted THz power is linked to the photocurrent through the emitter.

The detector can be built identical[5] to the emitter and works similar. Here, the electrical bias is the field of the THz pulse during the activated carrier life time. The acceleration of the charge carriers will create a current flow in the transmission line proportional to the electrical field. This current is pulsed with the repetition rate of the laser and a pulse length depending on the carrier life time. In most cases — with the exception of the aforementioned ASOPS — the current detection electronics has a rather low bandwidth compared to the laser repetition rate and thus detects a time averaged DC signal[6].

The high SNR of PCAs originates from the low duty cycle laser gating technique. Most of the time, the detector is in a state of very high output resistance (typically > 99.9 % of the time > 1 MΩ), yielding a very low Johnson-Nyquist thermal noise. The remaining noise component is mostly shot noise caused by incident laser radiation [64].

3.3. Polarization sensitivity

This section shows how polarization states are treated mathematically and introduces the techniques commonly used to detect polarization of THz radiation.

3.3.1. The Jones matrix formalism

A common way to express the polarization state of electro-magnetic waves is the Jones matrix formalism. The polarization state of the electric field $\boldsymbol{E}$ is expressed as a vector in an arbitrary two dimensional orthonormal basis perpendicular to the propagation direction of the wave.

$$\boldsymbol{E} = \boldsymbol{J}\ \mathrm{e}^{i(kz-\omega t)}, \text{ where } \boldsymbol{J} = \begin{pmatrix} E_\mathrm{x} \\ E_\mathrm{y} \end{pmatrix} \tag{3.1}$$

and the basis was chosen to be Cartesian coordinates with wave propagation along the z-axis[7]. E_x and E_y are complex quantities with their respective phase being the argument. For the polarization state only the phase difference $\Delta\phi$ matters while the common phase can be factored out into the wave propagation exponential.

Transmission through an optical element is then simply represented by a matrix-vector product:

$$\boldsymbol{J}_\text{transmitted} = T\boldsymbol{J}_\text{incident} \tag{3.2}$$

For a linear polarizer rotated by an angle φ with respect to the x axis and a leakage ratio η for unwanted polarization

$$T_\mathrm{P}(\varphi) = \begin{pmatrix} \cos^2(\varphi) + \eta\sin^2(\varphi) & (1-\eta)\cos(\varphi)\sin(\varphi) \\ (1-\eta)\cos(\varphi)\sin(\varphi) & \eta\cos^2(\varphi) + \sin^2(\varphi) \end{pmatrix}. \tag{3.3}$$

Transmission through multiple elements are represented by multiplication with further matrices. Since matrix multiplications are generally non-commutative the order (from right to left) is important.

[5] As the carrier lifetime determines the activation duration and thus the achievable sampling time resolution it can be beneficial to produce the emitter and detector on different substrates, focusing on low carrier lifetimes for the detector and high mobilities (resulting in high photocurrent) for the emitter.

[6] This signal can be further modulated to achieve higher SNR, e.g. modulation of the emitter bias voltage or the polarization modulation technique introduced in section 3.3.3.

[7] To distinguish the reference frame of the optical beam path from the sample-based one used in chapter 2, coordinates are written in an upright font

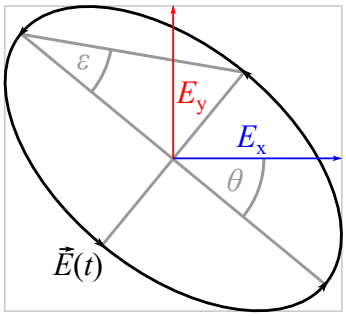

Fig. 3.4.: Representation of $\boldsymbol{E}$ using linear components (E_x, E_y) and ellipsometric quantities (rotation θ, ellipticity ε).

Another common parametrization for polarization states uses the degree of ellipticity ε (i.e. the ratio of the main axes of the polarization ellipsis) and rotation of the elliptic polarization main axis θ, see Figure 3.4. It is useful for presentation purposes but cumbersome to use in beam path calculations. It is linked to the Jones vector components by [65]:

$$\theta = \mathrm{Re}\left(\arctan\left[\frac{E_y}{E_x}\right]\right) \tag{3.4}$$

$$\varepsilon = \frac{1}{2}\arcsin\left(\tanh\left(2\,\mathrm{Im}\left(\arctan\left[\frac{E_y}{E_x}\right]\right)\right)\right) \tag{3.5}$$

3.3.2. Polarimetry with static polarizers

Classical polarimeters employ two static linear polarizers and the transmitted signal t is measured in both parallel (t_p) and crossed (t_c) alignment configurations of the polarizers.

While motorized rotation stages can align the polarizers with a precision well below 0.1 degrees, the achievable instrumental resolution is limited by THz antenna properties. This can be shown by analyzing the expected measurement signal for both polarizer configurations using the Jones matrix formalism. For simplicity of the example, imaginary parts are neglected and only the rotation θ is considered.

$$t_\mathrm{p} = T_\mathrm{P}(0)\cdot T_\mathrm{Sample}\cdot T_\mathrm{P}(0)\begin{pmatrix}E_\mathrm{x}^\mathrm{i}\\E_\mathrm{y}^\mathrm{i}\end{pmatrix} \tag{3.6}$$

$$= \begin{pmatrix}1&0\\0&\eta\end{pmatrix}\begin{pmatrix}t_\mathrm{xx}&t_\mathrm{yx}\\t_\mathrm{yx}&t_\mathrm{yy}\end{pmatrix}\begin{pmatrix}1&0\\0&\eta\end{pmatrix}\begin{pmatrix}E_\mathrm{x}^\mathrm{i}\\E_\mathrm{y}^\mathrm{i}\end{pmatrix} \tag{3.7}$$

$$= \begin{pmatrix}E_\mathrm{x}^\mathrm{i}t_\mathrm{xx}+\eta E_\mathrm{y}^\mathrm{i}t_\mathrm{xy}\\ \eta E_\mathrm{x}^\mathrm{i}t_\mathrm{yx}+\eta^2 E_\mathrm{y}^\mathrm{i}t_\mathrm{yy}\end{pmatrix} \tag{3.8}$$

$$|t_\mathrm{p}| \approx E_\mathrm{x}^\mathrm{i}t_\mathrm{xx}+\eta E_\mathrm{y}^\mathrm{i}t_\mathrm{xy},\ \text{for}\ \eta\to 0 \tag{3.9}$$

$$t_\mathrm{c} = T_\mathrm{P}\left(\frac{\pi}{2}\right)\cdot T_\mathrm{Sample}\cdot T_\mathrm{P}(0)\begin{pmatrix}E_\mathrm{x}^\mathrm{i}\\E_\mathrm{y}^\mathrm{i}\end{pmatrix} \tag{3.10}$$

$$= \begin{pmatrix}\eta E_\mathrm{x}^\mathrm{i}t_\mathrm{xx}+\eta^2 E_\mathrm{y}^\mathrm{i}t_\mathrm{xy}\\ E_\mathrm{x}^\mathrm{i}t_\mathrm{yx}+\eta E_\mathrm{y}^\mathrm{i}t_\mathrm{yy}\end{pmatrix} \tag{3.11}$$

$$|t_\mathrm{c}| \approx E_\mathrm{x}^\mathrm{i}t_\mathrm{yx}+\eta E_\mathrm{y}^\mathrm{i}t_\mathrm{yy},\ \text{for}\ \eta\to 0 \tag{3.12}$$

$$\tan(\theta) = \frac{|t_c|}{|t_p|} = \frac{E_x^i t_{yx} + \eta E_y^i t_{yy}}{E_x^i t_{xx} + \eta E_y^i t_{xy}} \tag{3.13}$$

$$\approx \frac{t_{xy}}{t_{xx}} \left(1 - \eta \frac{E_y^i}{E_x^i}\right) + \eta \frac{E_y^i}{E_x^i}, \text{ for } \eta \to 0 \text{ and } \begin{matrix} t_{yx} = t_{xy} \\ t_{yy} = t_{xx} \end{matrix} \tag{3.14}$$

However, eq. (3.12)ff. are only valid if the detector itself has a uniform polarization sensitivity which is generally not the case, especially with time-domain THz detectors. Instead one has to consider a reduced sensitivity $\delta \lesssim 1$ along one of the orthogonal components. In the following, the receiver is assumed to be aligned with it's maximum sensitivity direction along the parallel polarized configuration.

$$t_c^* = \begin{pmatrix} 1 & 0 \\ 0 & \delta \end{pmatrix} t_c \tag{3.15}$$

$$\left|\frac{t_c^*}{t_p}\right| = \begin{cases} \delta \frac{t_c}{t_p} & \text{for } \delta \frac{t_c}{t_p} >> \eta \\ \sqrt{\eta^2 + \left(\delta \frac{t_c}{t_p}\right)^2} & \text{for } \delta \frac{t_c}{t_p} \approx \eta \end{cases} \tag{3.16}$$

Therefore, the non-uniform polarization sensitivity adds at least an a priori unknown frequency dependent factor $\delta(\omega)$ which needs to determined in reference measurements. Additionally, this factor reduces the primary signal t_c^* and the achievable SNR. In case $\delta \approx \eta$ linearity and sensitivity for small rotations is also lost.

A fixed rotation of the receiver shifts the the problem between t_c^* and t_p^* components. The only solution is to rotate the receiver together with the analyzing polarizer for crossed and parallel configurations. This is a challenging construction and alignment task and it's likely to introduce other systematic errors.

Furthermore, this method requires two sequential measurements. Fluctuations in the THz source intensity and environmental conditions will additionally influence the evaluated rotation.

Using two synchronized detectors for both components (a polarizer can be used as beam splitter) the challenges above are lifted, but introduces higher costs and complexity.

3.3.3. Polarization modulation

Better resolution is typically achieved by employing a modulation method as described in great detail by reference [65]. This section shortly summarizes the description of the method.

The modulation technique uses two parallel static and one continuously rotating polarizer. While the static polarizers improve the linear polarization response of the emitter and detector systems, which might have some elliptic polarization character, the rotating polarizer is placed after the sample under investigation between the static polarizers. Such a system is described

by the Jones matrix formalism as

$$\begin{aligned}
\begin{pmatrix} E_{\mathrm{x}}^{\mathrm{f}} \\ E_{\mathrm{y}}^{\mathrm{f}} \end{pmatrix} =& T_{\mathrm{P}}(0) \cdot T_{\mathrm{P}}(\Omega t) \cdot T_{\mathrm{Sample}} \cdot T_{\mathrm{P}}(0) \begin{pmatrix} E_{\mathrm{x}}^{\mathrm{i}} \\ E_{\mathrm{y}}^{\mathrm{i}} \end{pmatrix} && (3.17)\\
=& \begin{pmatrix} 1 & 0 \\ 0 & \eta \end{pmatrix} T_{\mathrm{P}}(\Omega t) \begin{pmatrix} t_{\mathrm{xx}} & t_{\mathrm{yx}} \\ t_{\mathrm{yx}} & t_{\mathrm{yy}} \end{pmatrix} \begin{pmatrix} 1 & 0 \\ 0 & \eta \end{pmatrix} \begin{pmatrix} E_{\mathrm{x}}^{\mathrm{i}} \\ E_{\mathrm{y}}^{\mathrm{i}} \end{pmatrix} && (3.18)\\
=& \begin{pmatrix} E_{\mathrm{x}}^{\mathrm{i}}[t_{\mathrm{xx}}(\cos^2(\Omega t) + \eta' \sin^2(\Omega t)) + t_{\mathrm{yx}}(1-\eta')\cos(\Omega t)\sin(\Omega t)] \\ \eta E_{\mathrm{x}}^{\mathrm{i}}[t_{\mathrm{xx}}(1-\eta')\cos(\Omega t)\sin(\Omega t) + t_{\mathrm{yx}}(\sin^2(\Omega t) + \eta' \cos^2(\Omega t))] \\ \quad +\eta E_{\mathrm{y}}^{\mathrm{i}}[t_{\mathrm{xy}}(\cos^2(\Omega t) + \eta' \sin^2(\Omega t)) + t_{\mathrm{yy}}(1-\eta')\cos(\Omega t)\sin(\Omega t)] \\ \quad +\eta^2 E_{\mathrm{y}}^{\mathrm{i}}[t_{\mathrm{xy}}(1-\eta')\cos(\Omega t)\sin(\Omega t) + t_{\mathrm{yy}}(\sin^2(\Omega t) + \eta' \cos^2(\Omega t))] \end{pmatrix} && (3.19)\\
=& \frac{1-\eta'}{2} \begin{pmatrix} E_{\mathrm{x}}^{\mathrm{i}}[t_{\mathrm{xx}}\cos(2\Omega t) + t_{\mathrm{yx}}\sin(2\Omega t)] \\ \eta E_{\mathrm{x}}^{\mathrm{i}}[t_{\mathrm{xx}}\sin(2\Omega t) + t_{\mathrm{yx}}\cos(2\Omega t)] \\ \quad +\eta E_{\mathrm{y}}^{\mathrm{i}}[t_{\mathrm{xy}}\cos(2\Omega t) + t_{\mathrm{yy}}\sin(2\Omega t)] \\ \quad +\eta^2 E_{\mathrm{y}}^{\mathrm{i}}[t_{\mathrm{xy}}\sin(2\Omega t) + t_{\mathrm{yy}}\cos(2\Omega t)] \end{pmatrix} && (3.20)
\end{aligned}$$

Again, for simplicity of the example, imaginary parts are neglected and only the rotation θ is considered. The signal picked up by the detector is:

$$S = \frac{1-\eta'}{2} \left(\cos(2\Omega t)\left[E_{\mathrm{x}}^{\mathrm{i}} t_{\mathrm{xx}} + \eta E_{\mathrm{y}}^{\mathrm{i}} t_{\mathrm{xy}}\right] + \sin(2\Omega t)\left[E_{\mathrm{x}}^{\mathrm{i}} t_{\mathrm{yx}} + \eta E_{\mathrm{y}}^{\mathrm{i}} t_{\mathrm{yy}}\right]\right) + \mathcal{O}(\eta^2) \tag{3.21}$$

Using a lock-in amplifier one can demodulate both sine (S_{Y}) and cosine (S_{X}) components separately and obtain

$$\tan(\theta) = \frac{S_{\mathrm{Y}}}{S_{\mathrm{X}}} = \frac{E_{\mathrm{x}}^{\mathrm{i}} t_{\mathrm{yx}} + \eta E_{\mathrm{y}}^{\mathrm{i}} t_{\mathrm{yy}}}{E_{\mathrm{x}}^{\mathrm{i}} t_{\mathrm{xx}} + \eta E_{\mathrm{y}}^{\mathrm{i}} t_{\mathrm{xy}}}, \tag{3.22}$$

which is equivalent to eq. (3.13).

Unlike with static polarizers, the modulation method is not influenced by non-uniform polarization sensitivity when the antennas are aligned correctly. However, due to the modulation, about half of the primary signal for both components is lost (first factor in eq. (3.21)). This loss of signal strength is usually made up for by the reduction of the $1/f$ noise level through the modulation technique.

With this method, the measurement of both polarization components is inherently simultaneous with synchronized THz pulse sampling rate, which suppresses the influence of signal drift onto measured ellipsometric values. Compared to synchronous static polarizer techniques it is generally easier to align the optical components and maintain this alignment over long time periods.

3.4. Instrumentation

3.4.1. Overview

Figure 3.5 gives an overview of the TD-THz detection setup used in this work. Details of the components are given in the next subsections.

3.4.2. Terahertz generation and detection

The setup built for this work is based upon a *Menlo Systems Tera15* fiber-coupled TD-THz spectrometer. It uses a pulsed 1550 nm fiber laser system with dispersion-compensated split

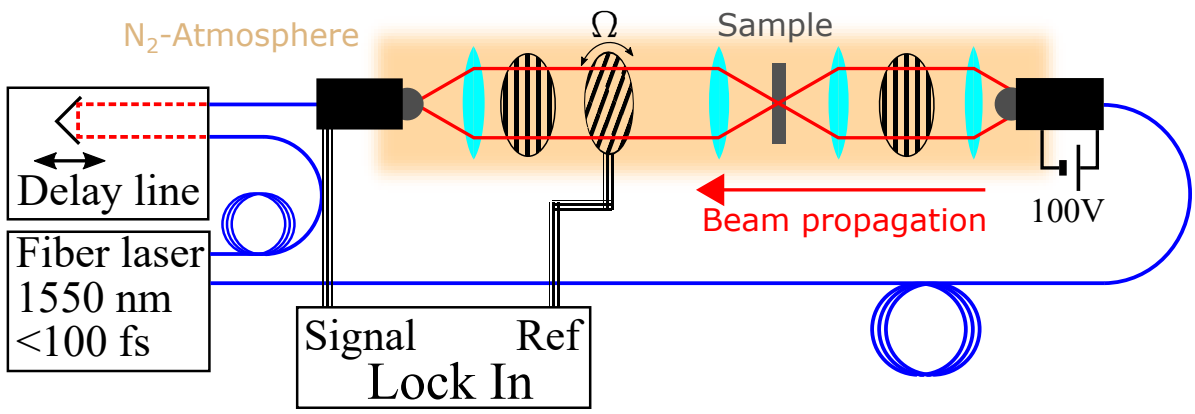

Fig. 3.5.: Schematic view of the TD-THz spectrometer. Synchronized laser pulses activate the THz antennas. Adjusting the delay between pulses enables the time resolved detection of the pulses' electrical field component. The sample is mounted inside a *Oxford Instruments Spectromag* cryostat (not depicted). Details are given in the following subsections.

outputs ($2\times \lesssim 40$ mW time averaged power) at a repetition rate of 100 MHz. The compensation is chosen such that a minimum pulse time below 100 fs is achieved after traveling through 5 m of polarization-maintaining fiber. At this point the fiber is terminated to the Austin switch type antennas.

While the emitter antenna is biased with a constant voltage of 100 V (supplied by a low-noise *AimTTi PLH120*), the receiver's electrical contacts are connected to a *FEMTO LCA-400k-10M* transimpedance amplifier to boost the THz electrical field-dependent photocurrent.

The adjustable delay between emitter and receiver activation is accomplished by inserting a free beam line into the fiber leading to the receiver. There, the pulse travel time is delayed by reflections from a fixed mirror and a movable retroreflector on a motorized linear mechanical stage (optical delay line). In this configuration, driving the stage position changes the travel distance for the activation pulse by four times the position difference. The linear motor is remote controlled using an *Aerotech Ensemble HPe10 MXH* driver, combined with a high-accuracy (± 1.0 µm) *Heidenhain LIP* incremental encoder system. This system enables sufficiently accurate positioning and very low position jitter (≈ 10 nm) in step mode as well as fast scan modes useful during system alignment.

The pulse is fed into and picked up from the optical delay unit using a *Thorlabs CIR-1550PM* fiber optic circulator. To compensate for the travel time differences in free beam paths to the receiver between optical activation and THz pulses, a dispersion shifted fiber [66] is also inserted into the fiber leading to the receiver.

3.4.3. Terahertz beam path

Since the polar molecules of water vapor have multiple absorption lines in the THz spectrum generated by TD-THz setups [67] the complete THz beam path from transmitter up to the receiver is additionally enclosed in a separate housing and continuously purged with dry nitrogen gas. As unpolar nitrogen molecules do not posses any transitions in the spectrum of the used THz radiation, this improves the overall signal strength and suppresses contributions of water transitions to the signal. This measure also keeps the cold outer windows of the cryostat free from water condensation, which would further obstruct transmission.

Beam collimation and focus make use of a set of 1.5 inch (*Menlo Systems*) and 2 inch (*Tydex*) diameter lenses made from the material TPX. Outer windows of the cryostat are also made from TPX which offers a very similar refractive index in the visible as well as in the THz spectrum. This is an important benefit compared to other materials when it comes to initial component alignment using a visible pilot laser or if a simultaneous optical excitation of the sample is desired. As for the inner cryostat windows, sealing the sample chamber against vacuum, a thin Mylar foil is used.

3.4.4. Polarization detection

The heart piece of the polarization modulation technique is the rotating polarizer. It's diameter must be big enough to match the collimated THz beam. Commercially available THz polarizers typically have outer diameters ranging from 1 to 2 inch, including their mounting enclosure. As no product on the market could host such an optic in a hollow shaft and rotate it around the shaft axis with sufficient speed of at least a few tens of Hertz a suitable motor was developed in house. A brass hollow shaft hosts a *Tydex* polarizer fabricated on a high-density polyethylene (HDPE) substrate with a clear aperture of 25 mm. The shaft is rotated by a *thin gap TG3842* motor assembly and mounted in two *FAG XC71910* high-precision ceramic bearings. The motor is driven in closed-loop pulse amplitude modulation mode by a *Celeroton CC-75-500* sensorless controller. This is necessary, as the usual approach of using Hall sensors to detect the actual phase of the motor failed in the stray field of the nearby cryostat magnet. A reference signal for the lock-in technique is generated by an LED illuminating a photodiode through a small bore diametric to the rotating shaft.

The modulated signal detected by the THz receiver is demodulated with a *Zurich Instruments MFLI* amplifier locked onto this reference.

As the polarization emission and sensitivity of the *Menlo Systems Tera15* antennas is not strictly linear polarized, an additional set of parallel polarizers (*Tydex* HDPE and *Infraspecs P01*) is placed in front of the antennas.

3.4.5. Sample positioning

Samples are mounted in an 18-pin ceramic chip carrier facing the THz emitter inside an *Oxford Instruments Spectromag* 10 T split-coil cryomagnet system. A hole drilled through the chip carrier acts as an aperture for the THz radiation. It's diameter is matched to the region of interest on the sample. Two samples can be mounted and electrically connected at the same time on the sample rod inside the cryostat.

The vertical position of a sample inside the cryostat with respect to the THz beam axis can be monitored with a camera viewing the sample rod from the side though an additional window. By using markers on the side of the sample slots, accurate sample positioning is possible. Automatic compensation of sample rod length changes upon temperature changes could be implemented optionally. Typical sample rod contraction when cooling down the sample in the variable temperature insert (VTI) of the cryostat from 300 to 1.5 K is on the order of 5 mm.

The cryostat is controlled by *Oxford Instruments Mercury iTC* (heaters, He flow control, level meters) and *Mercury iPS* (magnet power supply) controllers. Cryogenic fluids (liquid nitrogen and helium) inside the cryostat are automatically refilled from external dewars using in-house built devices. This reduces necessary user interaction to a minimum level, typically once per week during measurement campaigns for refilling of the dewars. Not only does this

make long-term measurements possible without 24/7 attendance, but also limits the influences on the measurement caused by changes in the environmental conditions.

3.4.6. Sample gating and Van-der-Pauw measurements

Samples with a lithographically defined gate structure come with contacts that allow for Van-der-Pauw (VdP) measurements [68] simultaneous to the THz experiment. The gate voltage is provided by one of the auxiliary output ports of the *Zurich Instruments MFLI*. The current is limited by a series resistor of 1 MΩ to protect the sample in case of a shorted gate dielectric. The VdP test current is also sourced from a constant voltage auxiliary output of the *MFLI* device over a 100 kΩ series resistor. The large resistance compared to the typical longitudinal resistance of the sample under test provides an almost constant test current of 2 µA.

The voltage drops over both series resistors are measured using *Agilent 34420A* nanovolt meters to determine the respective gate leakage and VdP test currents. The voltage drop over the sample is measured with the same instruments.

Since the measurement of the sheet resistance at zero magnetic field and the Hall resistance in presence of magnetic fields require a different configuration of sample contacts with respect to current drive and voltage sampling, the connection of the four VdP sample contacts is managed by a self-built analog multiplexer board. This way, all eight/four measurement configurations suggested by the NIST standard can be automatically probed at any gate voltage and magnetic field configuration.

From those measurements one can determine an estimate of charge carrier density individually for each magnetic field. However, the exact determination of charge carrier densities in a large scale VdP geometry is generally not as reliable as transport experiments on Hall bars. For the HgTe samples measured in this work, the determination of carrier densities close to the charge neutral point (CNP) is further obstructed due to the simultaneous presence of charge carrier populations with opposite sign and different mobilities. In such cases, the low magnetic field response is usually dominated by highly mobile electrons, whereas at larger magnetic fields the Hall signal shows a hole type slope [69]. A reliable automated evaluation of such a complex Hall signal is challenging, but for a simple estimation of a total charge carrier density, the following strategy has proven to be useful:

From all densities determined by individual measurement and evaluation of Hall resistances over the full magnetic field range, potential outliers[8] in form of the outer 10% of data points are removed. From the remaining data the mean and standard deviation are calculated. While the standard deviation does not represent a pure statistical error in this case, it serves as an indicator for the quality of the total estimate nonetheless. Furthermore, the values derived from minimal and maximal magnetic fields are also given in plots visualizing the gate action. While the minimal magnetic field value indicates the two-carrier behavior, the maximum magnetic field value serves as an indicator how much quantum hall plateaus influence the simple density estimate. Even when there are multiple quantum Hall plateaus in the Hall signal, the individually evaluated densities are fluctuating between over- and underestimates of the true charge carrier density, which makes the mean value reliable enough for the purpose of this work.

[8] Those can be caused by random spike like noise events, but also due to small constant voltage offsets in the different measurement ranges of the nanovolt meters, whenever Hall voltages are low in comparison. The emergence of quantum Hall plateaus also influences the evaluated density.

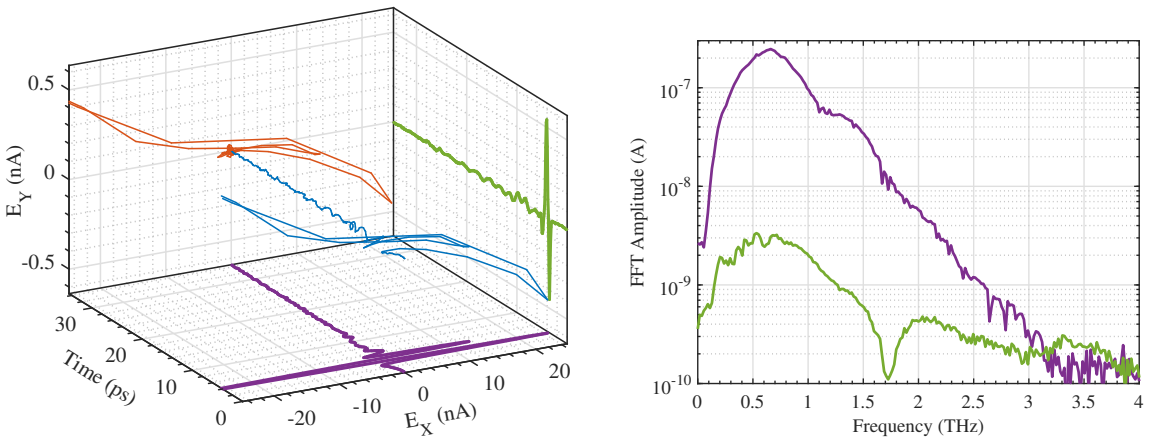

Fig. 3.6.: Left: Recorded electric field intensities by means of the demodulated detector photocurrents. Purple and green thick lines represent the orthogonal linear basis E_X, E_Y, while the blue line represent the total field vector time trace. The red line is a planar projection along the time axis. Right: Intensity spectrum calculated from the individual time traces via FT. Color code as in left panel. The pulses consist of a broadened spectrum with a maximum at 0.7 THz. In the low and high frequency limits, the intensity approaches the instrument noise floor.

3.5. Instrument characterization

In the following, the performance of the instrument under various conditions is discussed in detail. This establishes a common ground on how to judge the quality of the results discussed later on.

3.5.1. Intensity spectrum

After a single scan of the optical delay unit positions one obtains the time-resolved orthogonal electric fields that span the polarization state space. This signal, which must only contain a single pulse (i.e. no further reflections), is Fourier-transformed to resolve it's frequency components (see Figure 3.6). In order to be able to efficiently apply a fast FT algorithm the time-domain signal is padded with zeros such that its length equals a power of 2.

The intensity spectrum of a THz pulse is highly non-uniform and covers a bandwidth of approximately 3 THz before the signal is covered by the instruments noise floor. The instrument's performance is stable in the full operable magnetic field range, as displayed in Figure 3.7.

However, in the limit of high magnetic fields water vapor absorption lines emerge in the spectra [67]. This can be explained by magnetically forced air convection, which counteracts dry nitrogen gas purge of the optical beam path [70]. The forced convection is caused by the gradient of the stray magnetic field exerting a pulling force on surrounding air[9] while pushing diamagnetic nitrogen out of the field gradient. The resulting air flow thus effectively pulls water vapor into the stray field gradient of the cryostat's magnet. Those kinds of phenomena including water and magnetic fields are commonly labeled with the term "Moses effect" [71, 72].

[9] As air contains weakly paramagnetic oxygen which still is a much higher contribution as the diamagnetic susceptibility of the remaining gas mix.

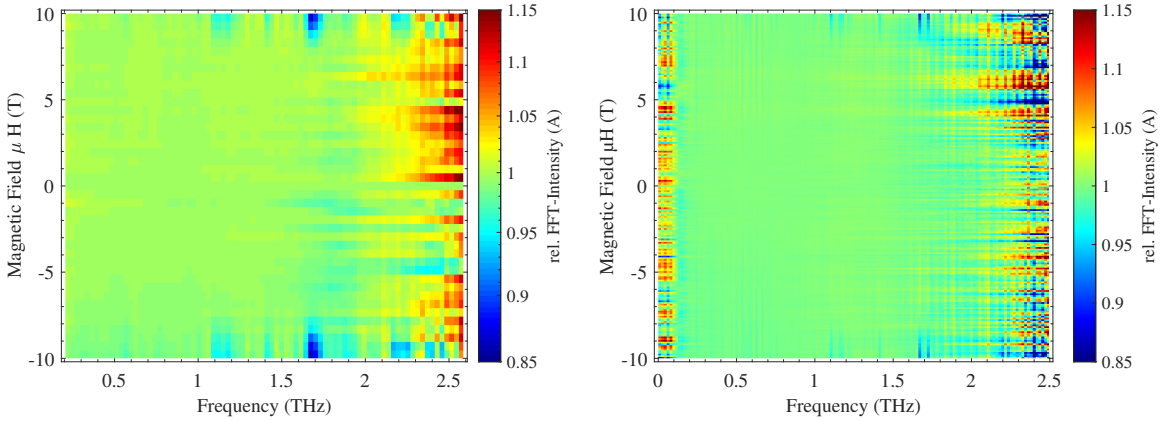

Fig. 3.7.: Intensity spectra relative to zero field. At high magnetic fields absorption lines are visible, but absorption was reduced after improving the dry nitrogen purge conditions (right). The origin of those absorption lines is discussed in the text. Data from [D1] (left) and [D2] (right).

After further improving the tightness of the beam path housing and adjusting the dry nitrogen flow parameters this effect was reduced. In order to completely remove the absorption lines from the spectra the beam path must be sealed against entering water vapor, for example by using silicone seals. As this would reduce the accessibility of optical components and the remaining absorption lines do not reduce the quality of the measured ellipsometric parameters, the setup remains unchanged.

The above hypothesis is investigated with a measurement series probing the THz transmission through the empty cryostat in the presence of high magnetic fields. Figure 3.8 shows how the transmitted signal evolves over time and with magnetic field changes. To enhance the effect, a small slit of approximately 5 mm is left open in the beam path housing near a cryostat window. For low fields the transmission is stable and free of noticeable absorption, but beginning at approximately 7 T water vapor absorption lines emerge in the spectra[10]. At this point the dry nitrogen purge is not strong enough to keep air from begin sucked into the beam path by the magnetic field gradient.

With the magnetic field being increased even further, water begins to condense at the cold cryostat windows. The amount of condensed water keeps increasing while a sufficient magnetic field is applied. The reduction of transmission is weakest around 0.2 THz. If the reduced transmission would only be caused by absorption, a monotonic increase of the absorption coefficient is expected in this frequency region [73]. Refraction must therefore also play an important role. The refractive index strongly increases in the low frequency limit [73], matching the observed reduction below 0.2 THz. The wavelength corresponding to 0.2 THz is 1.5 mm which is also the same order of magnitude of typical water condensate droplets size observed at the cryostat windows.

If water droplets grow large enough, they run down the window and temporarily leave a cleared path through which transmission is increased again. The clear path will quickly be filled with new condensate and the process can be repeated. This is the origin of the two brighter vertical lines after the 40 h mark in the top panel of Figure 3.8.

The evaporation and purging of the water takes time, therefore absorption remains present

[10] Exact values will depend strongly on environmental conditions as this effect is a result of forced air convection.

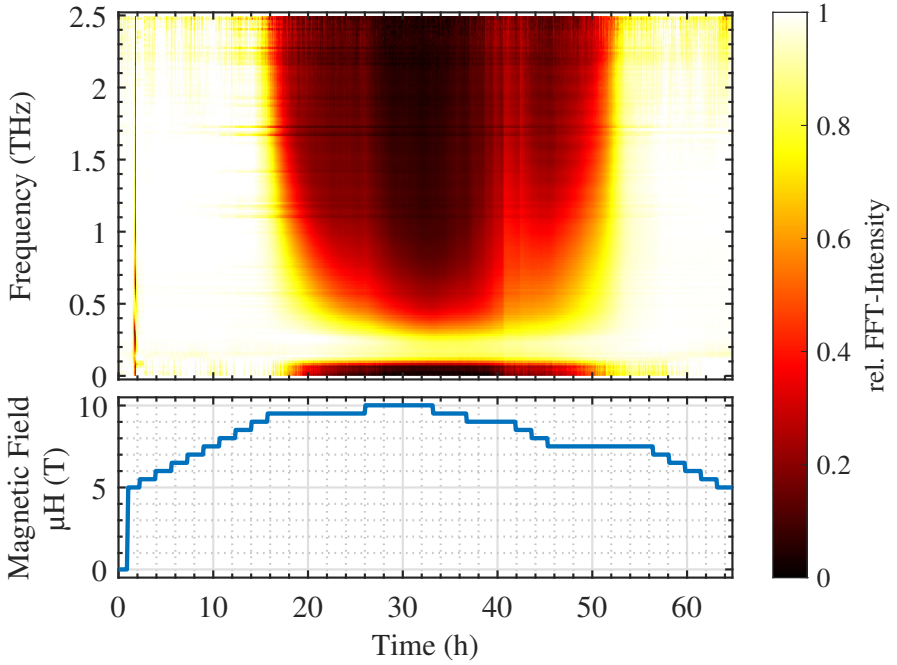

Fig. 3.8.: Spectra of THz pulses transmitted through the empty cryostat (top). Step-wise changes of the magnetic field during the measurement series is displayed in the bottom graph. At magnetic fields above 7 T signal absorption increases over time. The early feature shortly before the 2 h mark is caused by refraction at the surface of the liquid helium level temporarily rising through the beam path inside the VTI. Data from [D3].

after reduction of the magnetic field strength.

To complete the discussion of primary signal spectra the phase of the Fourier transformed signal is shown in Figure 3.9. A phase shift due to magnetic fields is visible.

The asymmetry comes from additional phase shift over time which is due to changes in environmental conditions, which influences the travel time of excitation laser pulses through the fibers. This is a rather small effect as identical changes in travel time in the fiber pair leading to the antennas will cancel out. However, localized changes of the temperature along the fiber paths can influence only one of the antennas and introduce a measurable pulse delay. With a temperature sensitivity of $\frac{\mathrm{d}n}{\mathrm{d}T} \approx 10^{-5}/\mathrm{K}$ [74] this introduces time delays on the order of 0.04 ps K^{-1} m^{-1}.

Magnetic fields affect optical fibers by means of the Faraday effect, which rotates the light polarization state as it passes through the fiber [75]. This effect splits the laser pulse traveling through the fiber into left and right circular polarized pulses moving with different speed. As the length of the laser pulse is shorter than 0.1 ps, a time delay of 0.2 ps would yield two separated excitation pulses with reduced power for each antenna. Therefore, the THz signal would be distorted rather than shifted in time.

Earlier arrival of the THz pulses by 0.2 ps can also be explained by a reduction of the THz free beam path by approximately 60 µm. The stray field of the split-coil magnet extends preferentially along the axis of the beam path and affects optical component mounts, including the THz antennas. The field significantly changes the power necessary to drive the motor rotating the polarizer, thus a small pull of the antennas towards the cryostat is a valid assumption.

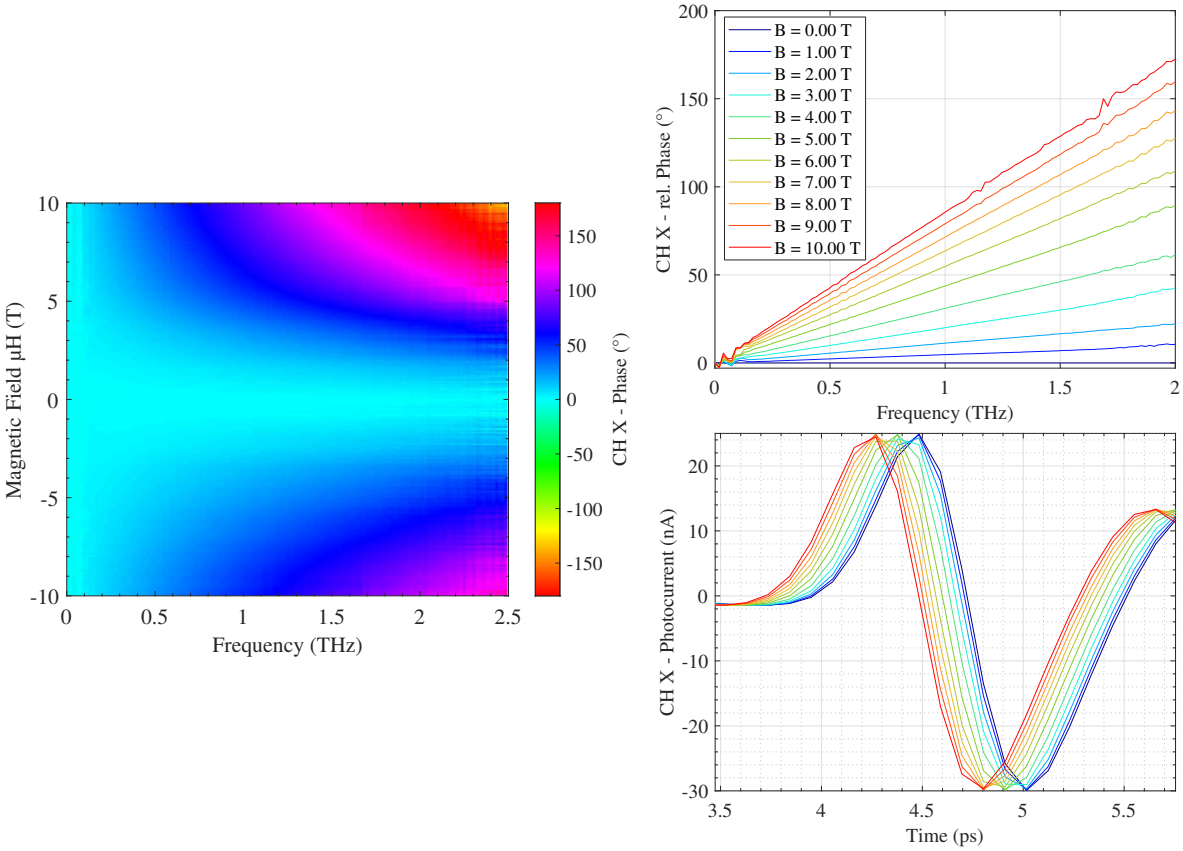

Fig. 3.9.: Left: Spectra of X channel phase relative to zero magnetic field. Phase shifts depend on magnet field magnitude and additional environmental influences. Top right: Line cuts along equidistant magnetic fields. Phase shifts follow the relation $\Delta\phi = -2\pi \cdot \nu \cdot \Delta t$. Bottom right: The detection of the time domain signal is shifted to earlier times in magnetic fields. Color code identical to left figure. Data from [D2].

As one of the benefits of the modulation technique, both polarization states E_X, E_Y are measured simultaneously and phase shifts affect both channels uniformly. As ellipsometric values only depend on relative changes between the X and Y channel, the observed phase shifts can be neglected.

3.5.2. Spot size

The spot size of the focal point at sample position was estimated by measuring the THz peak intensity transmitted through a 1 mm diameter aperture at a range of vertical positions inside the cryostat, as shown in Figure 3.10. Ideally, one would use a knife-edge scan, but no sample rod was readily available with a well defined metallic edge. Using a chip carrier with a hole instead still gives a good result, as can be seen in Figure 3.11.

Up to wavelengths comparable to the size of the aperture the measured spot sizes increase with wavelength. In the region used for ellipsometric measurements, the FWHM increases almost linearly from 1 to 3 mm. For wavelengths larger then approximately 600 µm, the hole is comparable or even smaller than the wavelength, which reduces signal transmission and distorts the wavefronts.

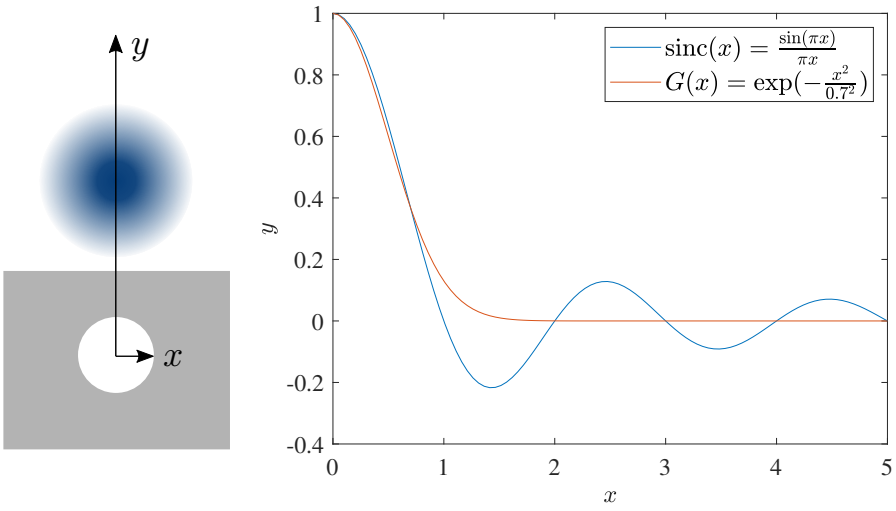

Fig. 3.10.: Left: Focus spot (blue) field strength distribution along y axis is measured by moving the chip carrier (gray) upwards. For each infinitesimal slice perpendicular to the x direction a different height of the hole contributes enters the convolution along y. Right: Approximation of the sinc function by a Gaussian profile. Here x, y denote general axes not related to real dimensions.

The graph also shows the diffraction limited FWHM spot size $4\sqrt{2\ln(2)}\frac{f\lambda}{\pi n D}$, calculated with the properties of the spot focusing lens (diameter $D = 50$ mm, focal length $f = 140$ mm), where λ is the wavelength and $n = 1$ the refractive index of the surrounding medium, air.[11]

However, as the spot is probed with a finite sized aperture, the measured signal is a convolution of the real spot profile and the hole geometry. An approximated closed expression for the FWHM after convolution with the hole is derived as follows.

As the repeated convolution of the rect function, which defines the real space geometry of the hole along a single dimension, with itself approaches a Gaussian function, the convolution of rect and Gaussian functions also result in a Gaussian function.[12] Additionally, the convolution of two Gaussian functions is also a Gaussian. Therefore, there must be a Gaussian function that approximates the rect function with respect to convolutions.

The rect transforms to the sinc function in Fourier space. This function is approximated by a Gaussian function as shown in Figure 3.10. As the FT of a Gaussian is again a Gaussian, a hole with diameter d can be approximated by a Gaussian with a real space 1/e radius of $w = \frac{d}{1.4\pi}$. The width of the convolution is then the root mean square of both Gaussian widths.

As the height of the hole varies in the direction x perpendicular to the position scan direction y, the effective value of parameter $d'(x) \leq d$ for each one-dimensional convolution along the scan direction y get smaller when x deviates from the hole center. It can be shown on a back of an envelope, that the measured signal is a weighted mean of many convolutions and the resulting FWHM is smaller than given by the approximated convolution above.

[11] As conventionally the measured quantity of light is intensity rather than electric field, FWHM is often defined from the intensity distribution. Here, the FWHM is defined with respect to the absolute value of the electric field. For the derivation of the diffraction limited spot size, the $1/e^2$ beam width has been set equal to D.

[12] This approximation is a consequence of the Central Limit Theorem and valid as long as hole diameter is not much larger as the sampled Gaussian. Otherwise the resulting convolution is a smoothed rect function instead of a Gaussian.

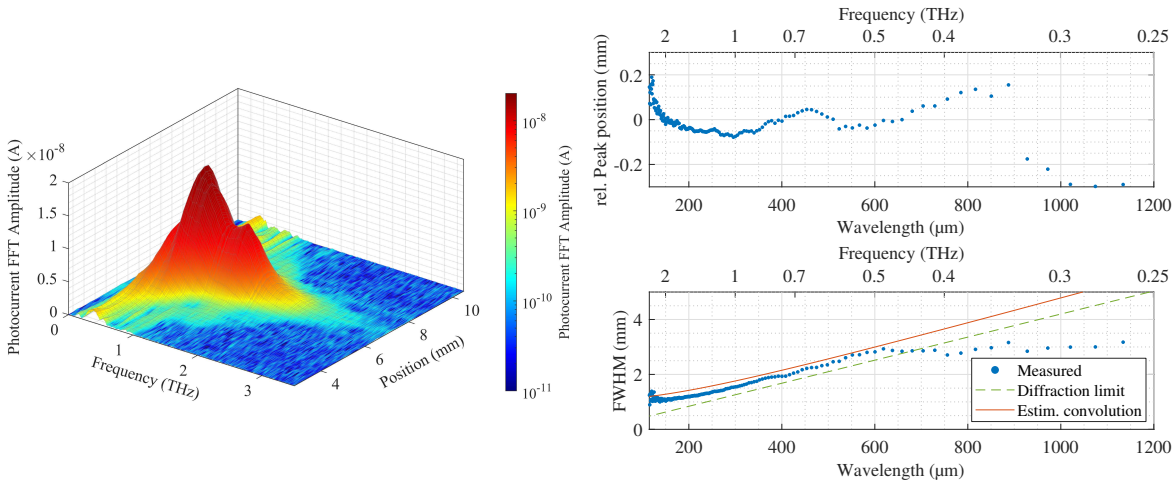

Fig. 3.11.: Left: THz field amplitude profile measured vertically through sample space. Right: Evaluated parameters from fitting Gaussian profiles for each frequency. Measured spot sizes are compared to the diffraction limit, see text. Data from [D4].

Therefore, the estimated convolution in Figure 3.11 is a theoretical upper bound[13] in case the system has a diffraction limited spot size. As measured spot widths are located in between both theoretical bounds for all wavelengths with significant transmission through the chip carrier hole, it is valid to assume that the system performs at the diffraction limit.

3.5.3. Initial polarization

Figure 3.12 shows the polarization state of the spectrum transmitted through an empty cryostat. For an ideal system one would expect a pure linear polarization, but in a real system there are always undesired effects that influence the polarization state.

The deviations from zero measured in the low frequency region are to be expected as they are still well within the specifications of the used polarizers. As an estimation one can take a rotation of 6 degrees of the linear polarization which evaluates to a ratio of 0.1 between crossed and parallel transmission of field amplitudes by a polarizer. For intensities, one has to take the square of this value, which is comparable to the degree of unwanted polarization (1%) of the *Tydex* HDPE polarizers when approaching wavelength of 2 mm (0.15 THz).

Further changes of the polarization state are introduced by misalignment of lenses against each other, lens defects and clipping effects at apertures of optical elements [65].

To correct the acquired spectra for these inherent deviations a subtraction of a reference signal is possible. Throughout this work spectra are presented with their zero magnetic field spectrum subtracted per default. One can verify in Figure 3.13, that this approach effectively cancels all static contributions inherent to the system, as these are not depending on the applied magnetic field.

In practice, the zero field correction introduces two issues: If just one single reference spectrum is subtracted from all other spectra, deviations on the order of the standard deviation may be added to all spectra, which introduces vertical lines in Figure 3.13 (upper row). Additionally, the effective field at the sample position is not truly zero, even if no currents run

[13] As the beam path was set to minimize possible clipping effects at lens apertures the beam width is smaller than given by the lens diameter. For the upper bound a smaller value of $D = 45$ mm was used.

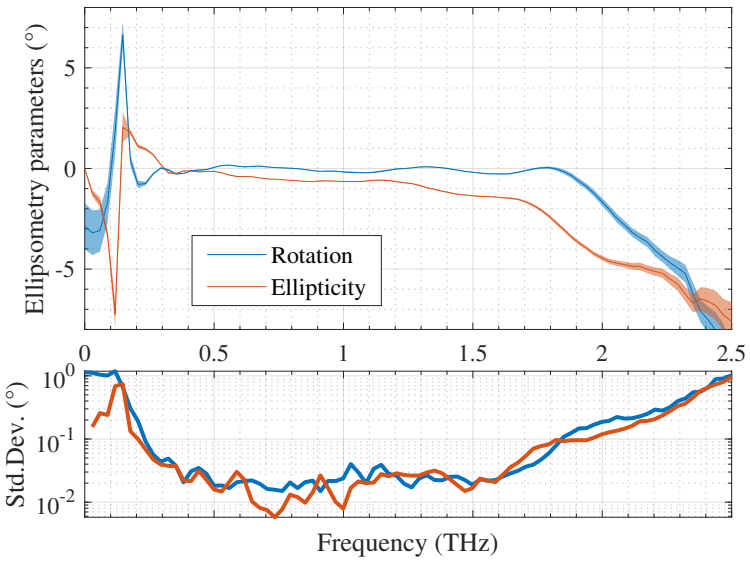

Fig. 3.12.: Polarization state of transmission spectrum through empty cryostat. Shaded areas denote the standard deviation calculated from 286 measurements, which is also shown separately below. The lock-in filter time constant for this scan was set to 0.5 s. With 278 sample points at 5 µm steps of the delay stage, a single scan takes 24 minutes. Data from [D5].

in the superconducting split coil magnet. Instead, a small field remains depending on the field ramping direction. Close to zero magnetic fields, such small offsets can notably influence the helicity and strength of transitions in a sample. In case any rotation and ellipticity features of the sample are fully anti-symmetric with respect to magnetic field, one may also use the mean spectrum from multiple spectra at maximum magnetic fields and opposite sign (e.g. -10, -9.9, +9.9 and +10 T) to obtain an effective, low-noise zero field reference (Figure 3.13, bottom row). As small hysteresis offsets are negligible compared to high fields, the mean of spectra at opposite high magnetic field cancels out anti-symmetric contributions from the sample, while preserving the static contributions of the elements in the beam path. The validity of this methods is checked for each measurement[14] and used preferably over the simple zero field spectrum correction wherever possible.

[14]In some cases purely technical issues, like defective power supplies or liquid helium level rising and falling through the beam path, lead to invalid spectra at some magnetic fields and forbid the application of this method.

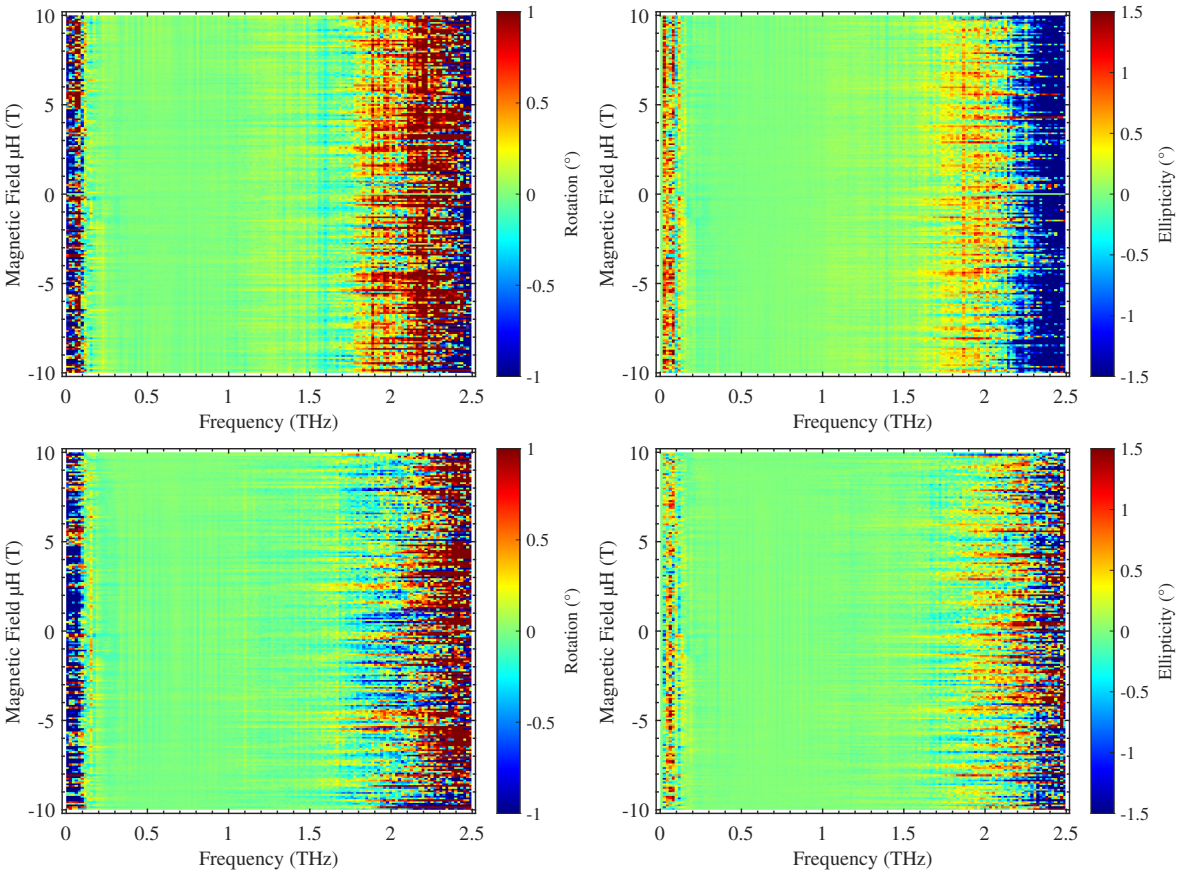

Fig. 3.13.: Polarization state of transmission spectrum through empty cryostat is not affected by applied magnetic fields up to ±10 T. Upper row: Background correction using zero magnetic field. Bottom row: Correction using maximum magnetic field amplitudes. Data from [D2].

3.5.4. Noise limits

It would be dishonest to define a fixed noise level for the ellipsometric quantities of Figure 3.12. As a motivation, the noise level σ_θ is derived in the limit of small rotations.

$$\theta = \tan^{-1}\left(\frac{E_Y}{E_X}\right) \tag{3.23}$$

$$\theta \approx \frac{E_Y}{E_X}, \text{ for } \lim_{\theta\to 0} \tag{3.24}$$

$$\left(\frac{\sigma_\theta}{\theta}\right)^2 = \left(\frac{\sigma_{E_Y}}{E_Y}\right)^2 + \left(\frac{\sigma_{E_X}}{E_X}\right)^2 \tag{3.25}$$

$$\sigma_\theta^2 = E_X^{-2}\left(\sigma_{E_Y}^2 + \sigma_{E_X}^2 \frac{E_Y^2}{E_X^2}\right) \tag{3.26}$$

$$\sigma_\theta \approx \frac{\sigma_{E_X}}{E_X}, \text{ for } \sigma_{E_X} \approx \sigma_{E_Y} = \sigma_E \tag{3.27}$$

Equation (3.27) shows that the noise level is mainly determined by SNR of the transmitted THz field $E \approx E_X$. While the measurement noise σ_E depends on the lock-in filter bandwidth

f_{BW} and the modulation frequency f_0 as given in eq. (3.30), the transmitted electrical field component depends on reflectivity and absorption within the sample stack, the focus aperture (i.e. hole diameter of the chip carrier), quality of the focal alignment and spectral density of the THz pulse (see Figure 3.6).

The integrated noise passing through the lock-in filter bandwidth is dominantly given by:

$$\sigma_E^2 = \int_{f_0-\frac{f_{\mathrm{BW}}}{2}}^{f_0+\frac{f_{\mathrm{BW}}}{2}} \left(\frac{S_{\mathrm{Pink}}}{f} + S_{\mathrm{White}} \right) \mathrm{d}f \tag{3.28}$$

$$\sigma_E^2 = S_{\mathrm{Pink}} \ln \left(\frac{f_0 + \frac{f_{\mathrm{BW}}}{2}}{f_0 - \frac{f_{\mathrm{BW}}}{2}} \right) + S_{\mathrm{White}} f_{\mathrm{BW}} \tag{3.29}$$

$$\sigma_E^2 \approx \left(\frac{S_{\mathrm{Pink}}}{f_0} + S_{\mathrm{White}} \right) f_{\mathrm{BW}}, \text{ for } f_{\mathrm{BW}} << f_0 \tag{3.30}$$

$$\sigma_E \propto f_{\mathrm{BW}}^{1/2} \propto T^{-1/2} \tag{3.31}$$

Here S_{Pink} and S_{White} denote constant factors for the contribution of pink (flicker) and white (thermal, shot) noise to the measured signal.

As the lock-in filter bandwidth f_{BW} scales inversely proportional to the filter time constant T and the filter settling time, which are directly proportional to the measurement time, a reduction of the transmitted THz field to a fraction x needs to be compensated by a x^{-2}-fold measurement time. For typical sample geometries and layer stacks x is on the order of 20–50 %.

During initial tests the best SNR performance was achieved by setting the lock-in filter order to 4 and the polarizer rotation frequency $f_0/2$ to 8008 rpm (133.5 Hz). This frequency is a compromise between reduced pink ($1/f$) noise and increased noise caused by motor vibrations at higher frequencies.

3.5.5. Resolution limits

While the resolution limit for the ellipsometric quantities is directly given by their noise limit, the resolution of the frequency axis is defined by fundamental FT properties. The resolution of a signal in frequency domain is reciprocal to its length in time domain (and vice versa).

For a evaluation that only takes a single pulse without additional reflexes into account, the maximum scan time is 0.17 ns before an additional pulse is picked up from a reflection between the inner windows (distance 25 mm) of the cryostat. In that case the frequency resolution limit is 6 GHz.

This limit is further increased once a thick sample is under investigation. In that case, the first reflection to arrive at the detector is caused by internal reflection at the sample's interfaces. In this work, this is caused by the samples substrate with a thickness of 1 mm after approximately 20 ps. Therefore, the typically achievable frequency resolution is 50 GHz.

Due to the low positional jitter of the optical delay unit the signal is sampled with a very low timing jitter of $\lesssim 0.2$ fs. Assuming typical measurement parameters, this leads to an FT amplitude bias factor below $\left(1 + 10^{-10}\right)$, as well as relative amplitude and absolute phase standard deviation below 10^{-5} [76]. Compared to other error sources, positional jitter can thus be completely neglected.

3.5.6. Thermal stability

The optical table is surrounded by a housing to limit free air convection. Inside, the temperature of all components is stabilized within 0.1 K by a set of water-cooled radiators. Hence, the influence of room temperature fluctuations can be neglected.

Temperature stability inside the cryostat, however, is of much more importance. Temperature changes in the sample chamber above approximately 50 K influence the optics alignment due to length contraction. And the temperature of the sample itself is of direct consequence for it's physical properties.

Above 4.2 K the thermal stability is only limited by the settings of the PID loop and typically is below 10 mK. For temperatures below the boiling point of liquid helium long-term thermal stability is often much harder to achieve and depends strongly on environmental conditions, settings for PID controllers and helium flow valve. Typically a *continuous base temperature* at 1.5 K can be achieved with a stability below 10 mK over multiple hours. However, this base temperature can drift to higher temperatures of 2–3 K over days, especially after refilling the cryostat's liquid helium reservoir. The sample temperature is thus recorded with every THz spectrum.

The temperature sensors are affected by magnetic fields. In the maximum field limit, the error is typically below 0.1 K.

3.5.7. Long term stability

The instrument provides a very good long term stability of measured polarization over more than a full month (see Figure 3.14[15]). This is achieved by the elimination of the influences through temperature fluctuations, optics mounted in rigid cage systems and the operation stability of the fiber laser system coupled to the THz antennas. Due to the almost complete automation of the instrument, disturbances (room illumination, vibration, etc.) by user interactions are also limited to a minimum amount — once per week.

In the presented example, the VTI temperature has been kept stable at 5 K for multiple days and afterwards the VTI was left to heat up naturally to the equilibrium temperature, given by radiation heat exchange with outer cooling shields. The large change of temperature slightly changes the elongation of the VTI and its position in the beam path. This has minor influences on the measured values, which can usually be ignored.

Automated filling processes for cryogenic fluids can temporarily influence the transmission of the THz signal by a few percent, which is most likely due to pressure changes and slight deformations inside the cryostat. As the signal level quickly stabilizes back to the previous level, this influence can be suppressed by pausing the measurement process shortly while refilling. Changes in ellipsometric values are not observed above the noise level of measurements with samples inside.

[15] Note that the standard deviation for these measurements is larger compared to Figure 3.12. This is due to a much shorter lock-in filter time constant of 0.1 s.

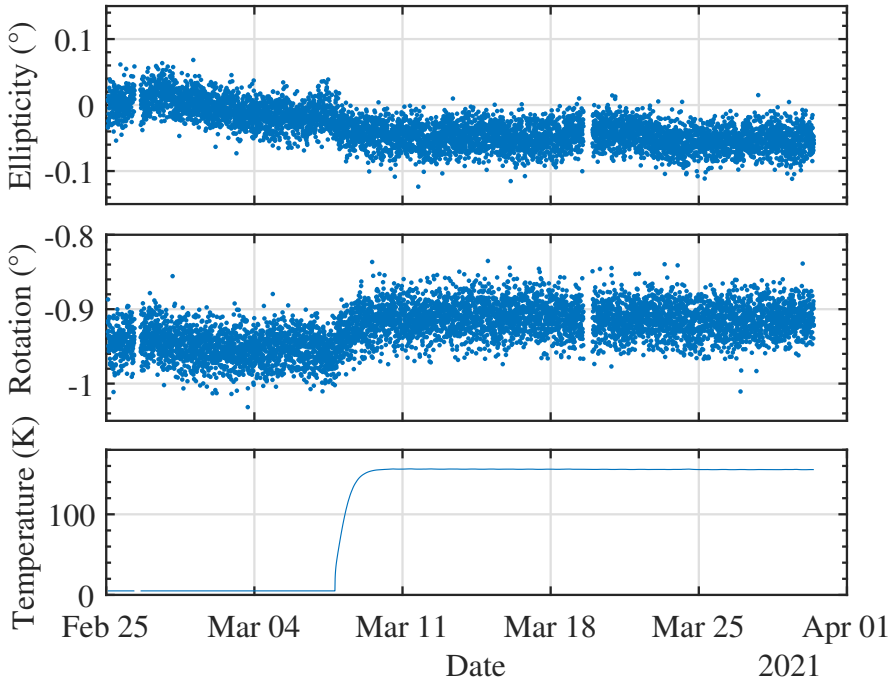

Fig. 3.14.: Long term evolution of measured ellipticity (top panel) and rotation (middle panel) of the linearly polarized THz signal transmitted though the empty cryostat. Both values are averaged over the minimum-noise frequency range from 0.5 THz to 1.5 THz. Bottom panel: Measured cryostat VTI base temperature in the same time interval. The two missing data slices are caused by temperature controller and PC issues which required manual restarts of the measurement series. Data from [D6].

4 Materials

This thesis focuses on the material system of tensile strained mercury telluride, grown as thin films using molecular beam epitaxy (MBE). As can be seen in later chapters, even though mercury telluride has a long history in scientific research and generally counts as reasonably well understood, it still provides more than enough challenges.

4.1. Mercury cadmium telluride material systems

After silicon and gallium arsenide, the material systems made from the elements mercury, cadmium and tellurium count as one of the well established material systems. Due to the good tuneability of the crystal bandgap in the sub-eV energy range, it has a long history as basis for infrared sensor and emitter applications [77, 78]. The improvement in growth and analysis techniques and substrate quality driven by commercial sensor industry lays the ground for the high-quality samples needed for modern research on the topological properties of the material system. At the university of Würzburg, the MBE growth of mecury cadmium telluride (MCT) material systems has further been optimized for high purity. The extensive infrastructure for advanced lithographic processing enables the fabrication of well defined gate structures and good ohmic contacts to the individual layers of samples. This allows for probing and adjusting the charge carrier density independently from optical methods.

Very detailed information about general properties of MCT material systems can be found in countless textbooks, dissertations and papers on the topic, which are cited throughout this chapter. Nevertheless, a short introduction into the bandstructure properties is given to introduce some of the notation that is used throughout this thesis.

Both mercury telluride (HgTe) and cadmium telluride (CdTe) crystallize in the zinc-blende structure with lattice constants of $a_{\mathrm{HgTe}} = 0.6462$ nm and $a_{\mathrm{CdTe}} = 0.6482$ nm (at 25 °C) [79].

Figure 4.1 shows the bulk bandstructure around the Γ point calculated by `kdotpy` [37] using the approach introduced in chapter 2. Note that relativistic corrections shift the energetic positions of the bands and due to the large atomic mass of mercury invert the normal band ordering [80]. For unstrained mercury telluride this leads to a zero-gap bandstructure, where conduction and valence bands meet exactly at the Γ point.

While bulk mercury telluride is a zero-gap semiconductor (semi-metal), both the introduction of tensile strain and confinement in HgTe - CdTe quantum wells (QWs) above a critical thickness open up a bulk band gap at the Γ-point. The band inversion in HgTe gives rise to intrinsic surface states that cross the the bulk band gap. More details concerning these topological properties can be found in section 1.1 and references given therein.

The existence of interface-bound states in the MCT material system has already been discussed in the 1980s and was investigated in the context of superlattices and quantum wells [5, 81, 82, 83, 84, 85, 86, 87, 88], but with the upcoming concept of topological materials this kind of interface states have been intensively studied again for almost 20 years [13, 14, 20, 69].

Figure 4.2 shows bandstructures calculated using `kdotpy` for QWs below and above the critical point and for a thicker strained layer. The original eight bulk Γ-orbital bands are now split into many subbands, which arise from confinement to a finite thickness. Thinner layers lead to larger confinement energy which causes the energetic separation of the subbands. With increasing thickness subband spacing gets denser, the E1 subbands approach the L1 subbands and dive under more and more H subbands.

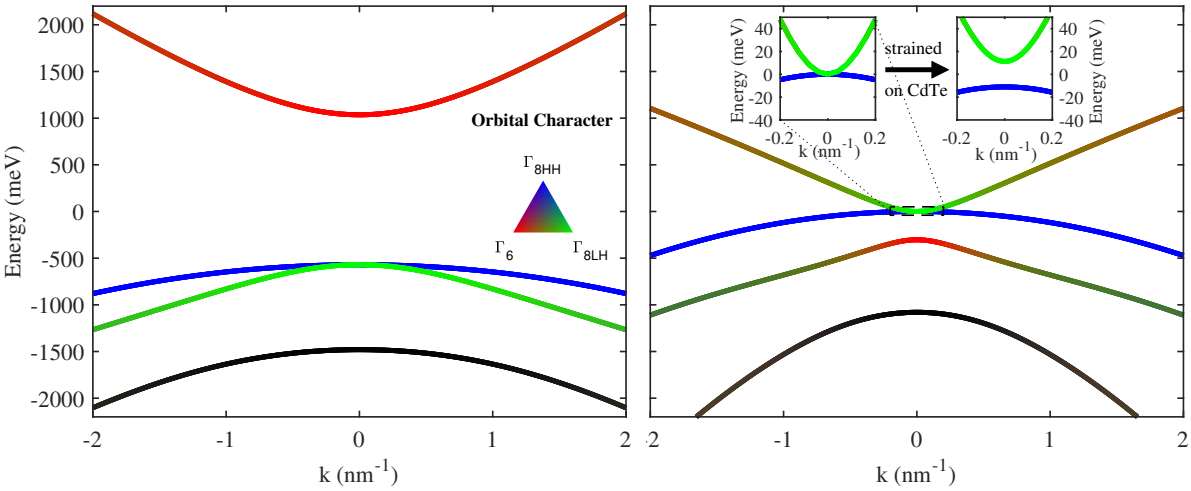

Fig. 4.1.: Bulk band structures around the Γ-point for CdTe (left) and HgTe (right). The color triangle shows how the orbital character for each band and black is the Γ_7 split-off band. The insets show how lattice strain opens a small bandgap at the touching point of unstrained HgTe valence and conduction bands. All bands are doubly degenerate. Calculated by `kdotpy`[C1, C2, C3].

This thesis employs the usual notation to label subband states [12, 32, 37, 45], which is derived from the orbital character of the subband at the Γ point. With normal band ordering the label letters can be interpreted as:

E — *electronic* conduction band states
H — *heavy* hole valence band states
L — *light* hole valence band states
S — *split-off* hole band states

The definition is chosen such that is consistent over the critical band crossing point, even though not all subbands are "pure" in terms of the Γ orbital contributions at $\boldsymbol{k} = 0$, but formed from linear combinations [12, 37]. The change in orbital character can be seen in Figure 4.2 as well: For small thicknesses of the HgTe QW the orbital character of the conduction bands is similar to the bulk character of the surrounding CdTe layers. This orbital character changes more towards the situation in bulk HgTe with increasing thickness, with additional intermixing of orbital character for the upper valence band states.

The number following the letter denotes the subband quantum number (i.e. the number of extrema in the orbital wavefunction that defines the character). The last symbol is the sign (+/-) of the angular momentum components of the orbitals involved at the Γ-point and is often omitted due to degeneracy.

4.2. Thin film strained mercury telluride layers

This section focuses on the preparation of samples used in this thesis, which are thin films (or very thick QWs) of mercury telluride, grown fully strained on cadmium telluride substrates. Due to lattice relaxation, fully strained mercury telluride layers can only be grown up to about 155 nm thickness [31, 35, 89]. These films have been claimed to be three dimensional

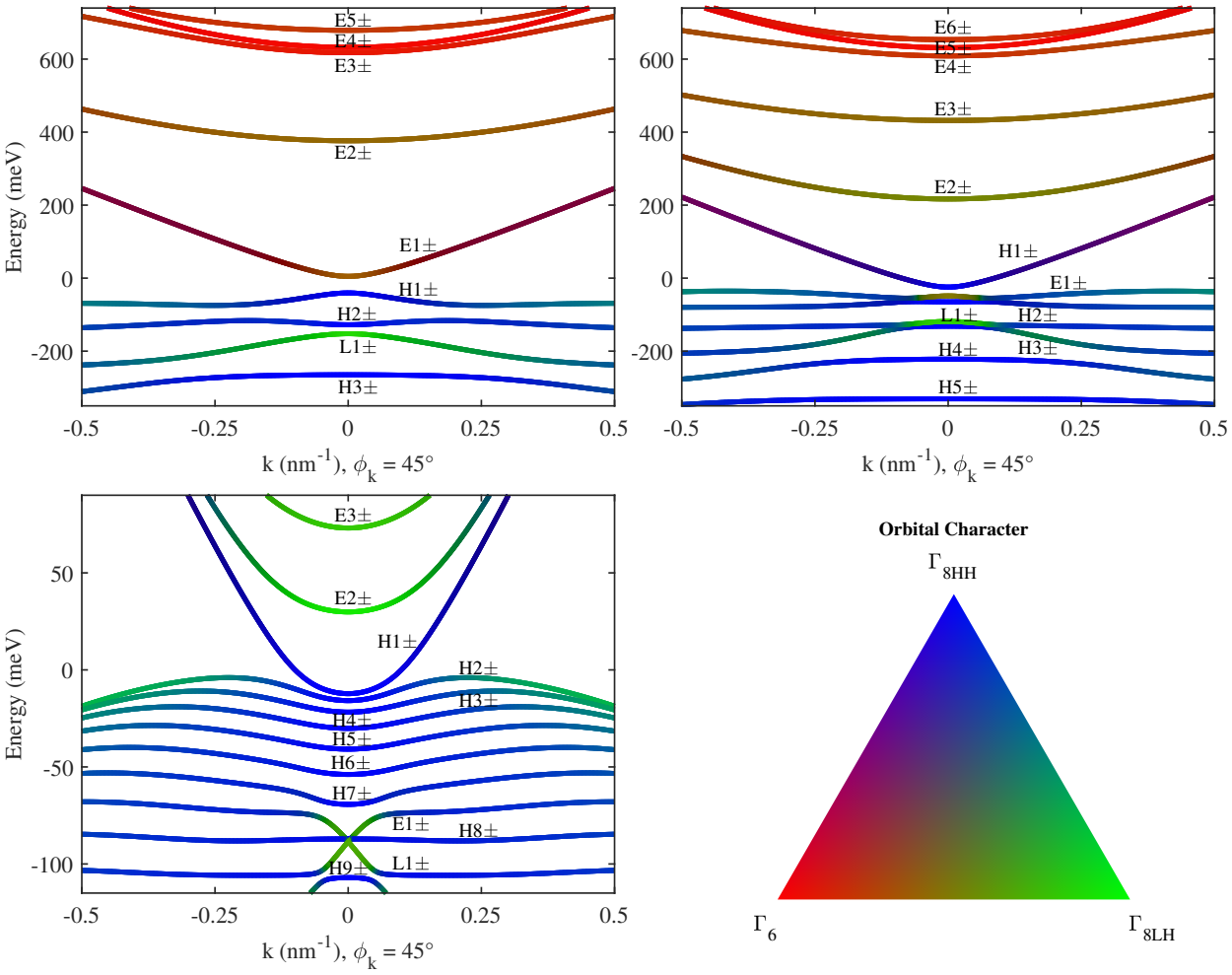

Fig. 4.2.: Bandstructures around the Γ-point for CdTe-HgTe-CdTe QWs, with HgTe layer thicknesses of 5 nm (top left), 8 nm (top right) and 30 nm (bottom left). Band labels are explained in the text. Orbital character is displayed by the color triangle (bottom right) as in Figure 4.1. Edge states are not displayed, as the `kdotpy`-calculations refer to layers extending infinitely perpendicular to the growth direction [C4, C5, C6].

topological insulators [27, 30].

4.2.1. Layer stack

Samples are grown in the MBE of the chair of experimental physics III (EP3) on commercially available $10 \times 10 \times 0.8$ mm^3 large CdTe substrates. In order to provide a clean interface, a $Hg_{0.32}Cd_{0.68}Te$ barrier layer is grown first with a typical thickness of 100 nm. It is directly followed by the HgTe layer with the desired thickness. To provide protection against oxidation and other property altering effects, a top $Hg_{0.32}Cd_{0.68}Te$ capping layer is grown last with thicknesses ranging typically between 20 and 60 nm. All three layers are grown in-situ in a single MBE chamber.

While the existence of the top and bottom barriers is important for the interface properties when modeling the sample, the exact thicknesses are not important, as the wavefunctions decay

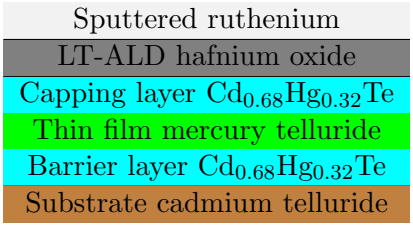

Fig. 4.3.: Cut of the layer stack along growth direction z (bottom up) as traversed by the THz beam. The top gate structure layers are also included.

rapidly towards zero within about 5 nm inside the barrier for the samples investigated here.

4.2.2. Lithographic preparation

To enable reliable and homogeneous gating of the sample over a region comparable to the spot size of the focused THz beam, a lithographic process was developed throughout this thesis. It is based on processes established within the chair of EP3 and has been adapted and optimized for the large geometry and gate transparency required for THz transmission experiments.

To make most use of the circular THz spot while maintaining an efficient sample size and compatibility to the laboratory environment of EP3 (chip carrier model, sample holders, etc.) and a good measurement quality, a quadratic mesa layout of about 2 mm length is chosen. In case the available sample piece is too small to accommodate the structure, all geometries can be scaled accordingly.

The final structure offers four contacts for Van-der-Pauw and Hall measurements and gate structure with a thin conductive layer on top to provide a equipotential surface without too much attenuation of the transmitted THz pulses.

In the following, the latest version of the preparation process is summarized, with micrographs taken between major steps shown in Figure 4.4. A detailed and up to date process protocol can be found in reference [90].

After MBE growth, the wafer is cleaved along [110] direction into rectangular pieces ranging from 3×3 to 4×5 mm^2.

For sample fabrication, a single piece is first covered with *MicroChemicals AZ ECI 3007* positive photo resist. The resist is then exposed with the mesa structure for VdP measurements using a *Durham Magneto Optics MicroWriter ML3*. After development of the photo resist with *MicroChemicals AZ MIF-726*, the layer stack outside of the mesa area is removed from the top side down into the substrate with a diluted KI:I_2:HBr:H_2O wet etch process, see Figure 4.4(a). The height of the remaining mesa with respect to the etched surrounding typically ranges between 200 and 300 nm.

All following steps use a *MicroChemicals AR-N 4340* negative photo resist exposed by the micro writer system and development with *MicroChemicals AR 300-47*.

The next photo resist mask defines the sample's gate structure. After development, the mesa surface is cleaned using a short O_2 plasma pulse which removes residues of previous photo resists. Directly afterwards the sample is inserted into a custom-built atomic layer deposition (ALD) system, operating with the sample at room temperature to protect the integrity of the mercury telluride layer. Here, a 15 nm thick insulating, amorphous layer of hafnium dioxide (HfO_2) is grown directly on top of the mesa structure.

Afterwards, an 8 nm thin, conductive layer of ruthenium is sputtered on top of the HfO_2 layer using the sample resist mask, which is lifted off thereafter. The finished gate structure

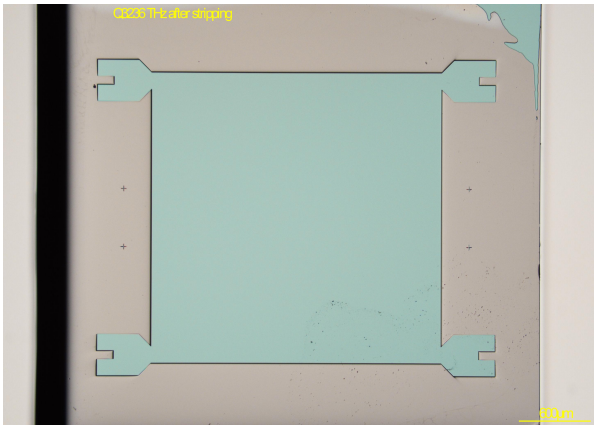

(a) Mesa (green) with HgTe layer after wet-etching process. Surrounding has been etched into the CdTe substrate.

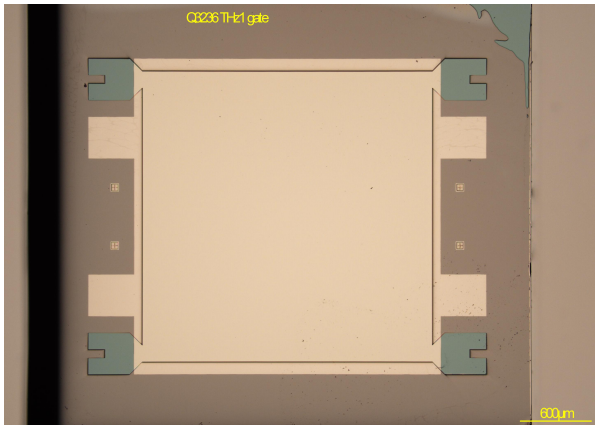

(b) HfOx and ruthenium gate layers (light brown) on top of the mesa structure. The gate fully covers all mesa edges.

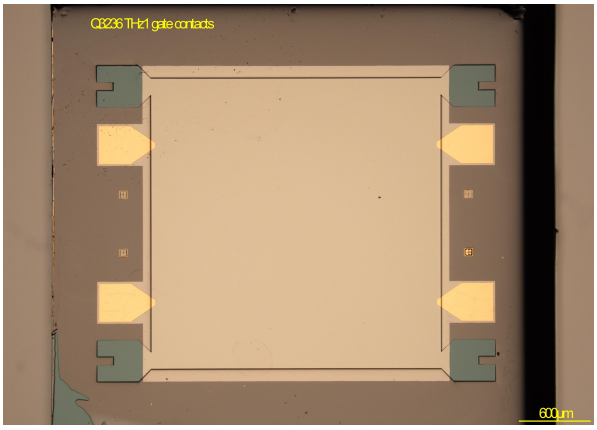

(c) Gate Ti/Au contacts (yellow) next to mesa structure. Reliable conductivity over the mesa edges is ensured by triangular tips of the contacts extending to the top of the mesa structure.

(d) Added Mesa AuGe/Au contacts (outer four yellow squares) on top of the mesa after etching through the capping CdHgTe layer.

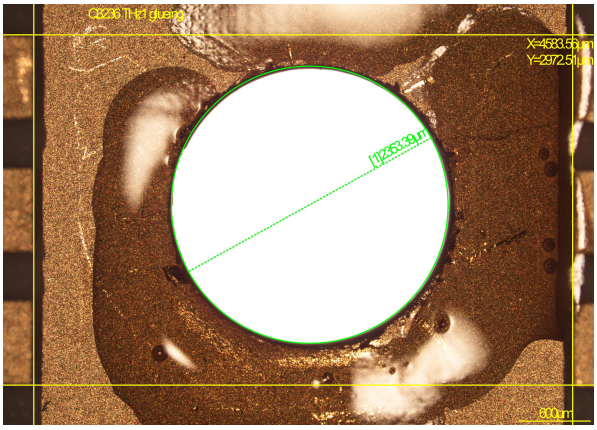

(e) Chip carrier prepared with hole and glue. Aligned under microscope.

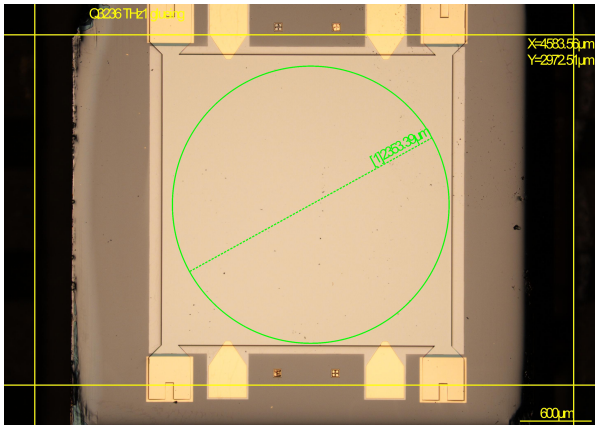

(f) Sample aligned and glued into the chip carrier. Green circular marker indicates the position of the hole for THz transmission through the chip carrier.

Fig. 4.4.: Micrographs during successive process steps of lithographic preparation. Provided with friendly permission by Christian Berger, who also prepared the shown sample.

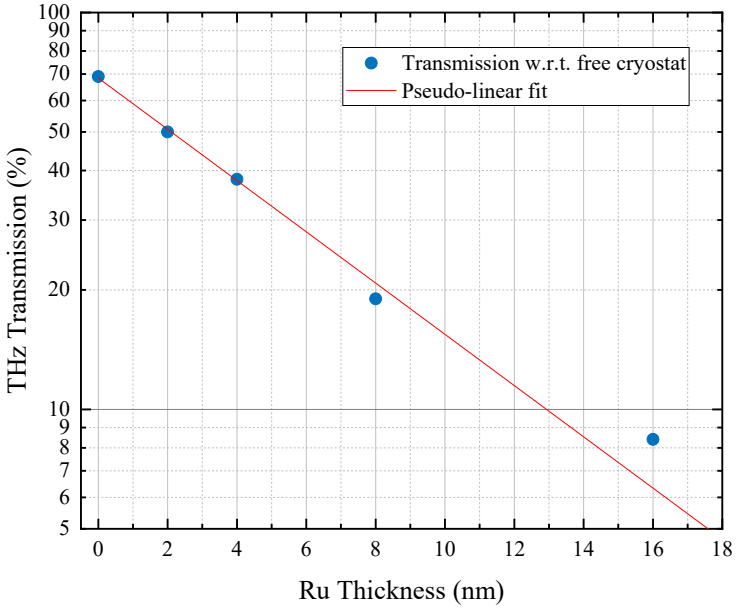

Fig. 4.5.: Reduction of transmission estimated from the peak in the time domain signal by the sample with respect to the free optical beam path with different thicknesses of the ruthenium layer.

can be seen in Figure 4.4(b). Reuse of the resist mask is crucial for the process, as the resist developer chemicals etch the HfOx layer, which would lead to shorted gates when defining a new mask on top of the bare insulator. A homogeneous and full coverage of the ruthenium layer is equally important to protect the insulating layer in the following step. This puts additional constraints on the mask geometry for following conductive layers. In sharp angled corners of the mesa (e.g. at the mesa contacts), a complete coverage of the insulator by ruthenium can not be guaranteed. The choice of ruthenium layer thickness is a trade-off between better protection of the underlying insulator (thicker layer) and increased THz signal transmission (thinner layer). Figure 4.5 shows how transmission of the THz pulse is reduced with increasing thickness.

With the next mask the gate contacts are metallized by a 5 nm Ti sticking layer and 100 nm Au. Bonding pads are placed outside of the mesa area on the substrate to protect the structural integrity of the gate layer stack during bonding. The thick Au layer ensures conductive contact over the mesa edge by small tips extending to the top of the structure (see Figure 4.4(c)). These tips are narrow to reduce the probability of hitting a spot where there has not been enough ruthenium coverage at the mesa edge to protect the gate insulator from the mask developing agent. To test the conductivity of the ruthenium layer and provide extra redundancy, four bonding pads are present in the layout.

Finally, mesa bond contacts are defined with a last photo resist mask. Before metallization with 50 nm AuGe and 50 nm Au, the contact areas are partly etched through the top barrier layer with in-situ Ar^+ ion beam etch to ensure a good ohmic contact. Figure 4.4(d) shows the finished structure.

The lithographically structured sample is then glued into a chip carrier such that the aperture defined by the chip carrier hole (Figure 4.4(e)) and the mesa with the layer stack are aligned (Figure 4.4(f)). Contacts are ultrasonically wedge bonded to the chip carrier with gold wires.

5 Results and discussion

Layered $Hg_{0.32}Cd_{0.68}Te$ - HgTe - $Hg_{0.32}Cd_{0.68}Te$ samples with HgTe thicknesses ranging between 30 and 70 nm have been measured in magnetic fields up to ±10 T. The layer's charge has been tuned between electron (n-type) and hole (p-type) conductivity up to about 10^{12} cm^{-2} carrier densities by the lithographically defined gate structure on top of the samples.

This way, the samples' band structures are indirectly probed within approximately 10 meV around the electro-chemical potential (ECP) for every gate voltage. Given the charge carrier density and the band structure states, the ECP position is calculated by `kdotpy` and shown in the Landau level (LL) state plots as dotted black line in order to visualize the filling of the band structure. While small errors in the carrier density can affect the position of the ECP line, this does not affect the energetic position of transition features, but only the filling factors of the transitions' states and thus the strength of the feature. In the region of small magnetic fields, the LL state degeneracy is very small and an accurate description of the band structure would require much higher LL quantum number states. Here the calculated ECP diverges which signals the end of the validity range of the LL state calculation.

The absorption of circular polarized photons by LL transitions yields the energetic differences between LL states in terms of the resonant photon energy. The ellipticity signal of the Terahertz (THz) measurement shows transitions resonances as distinct peaks and the sign (i.e. helicity) is directly connected to the sign of the LL number difference ΔN (see section 2.2). Thus, the measured ellipticity spectra are compared to spectra computed from band structure models, as described in previous chapters.

The presentation and discussion of data is structured along the line of charge carrier densities from n- to p-type. This corresponds to moving the electro-chemical potential downwards in energy from the conduction band over the topological band gap crossing states into the valence bands. Concomitantly, this requires increasing the level of asymmetry included in the $\boldsymbol{k} \cdot \boldsymbol{p}$ Hamiltonian.

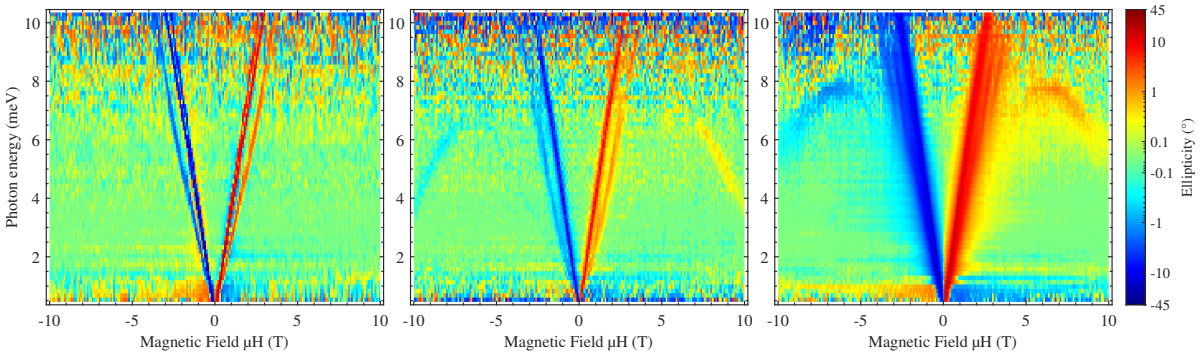

Fig. 5.1.: Measured THz ellipticity spectra in the n-type charge region for samples with HgTe layer thicknesses of 30, 45 and 58 nm (from left to right). Features are discussed in the text. Data from [D7, D8, D9].

5.1. Conduction bands in the n-type charge regime

5.1.1. Overview

In Figure 5.1 an overview of ellipticity spectra of three different samples gated into the n-type regime is presented. For all HgTe layer thicknesses, the features' helicities in the spectra are anti-symmetric with respect to the magnetic field. The features visible here can be classified into three categories:

- Up to magnetic fields of about 4 T cyclotron resonance mode like features cross through the measurable photon energy range. These features are present throughout the full accessible gate voltage range, but the ellipticity amplitude increases in the n-type regime. A splitting into multiple single lines can also be observed depending on the gate voltage.
- At higher magnetic fields additional features with the same helicity as the previous category can be found. They have a non-linear magnetic field dependence and while they are also caused by similar Landau level transitions as before, one would not use use the term cyclotron resonance in this context. These features are often caused by a single pair of final and initial states which are well separated in energy from other transitions. Their appearance evolves with the gate voltage.
- In the low photon energy limit the spectra show signatures of opposite helicity, which do not depend strongly on the magnetic field. These can be identified as plasmonic excitation of free charge carriers, which can follow the external electro-magnetic field fast enough to cause a (partial) reflection of the incident wave. For photons with a helicity opposite to the cyclotron resonance active (CRA) mode, the "effective frequency seen by the electrons" is higher and the plasmonic reflection is reduced for the cyclotron resonance inactive (CRI) mode [A1, 91]. This leads to a higher transmission for the CRI mode, as observed in the experiment. The plasma frequency and strength of this effect scales foremost with charge carrier density and mobility, but also effective mass and the dielectric constant. The comparison between different samples is thus challenging, as not all parameters are well known. However, this feature becomes stronger at higher charge carrier density for all samples. As these features at or even below the lower frequency limit of the spectral window of the setup, their discussion is limited in the scope of this thesis.

5.1.2. Comparison to the axial model

Origin of spectral features

The measurement results shown in Figure 5.1 can be explained even with the axial symmetry level of approximation in the Kane Hamiltonian. Figure 5.2 shows the magnetic field dependence and the spectra calculated from the optical transitions.

The charge carrier density evaluated from simultaneous Van-der-Pauw (VdP) measurements is used to determine the ECP. For all three measurements, the carrier densities are high enough to partially fill LLs emerging from the E2 conduction band.

Features classified as cyclotron resonance (CR) in experimental spectra can be traced down to be caused by LL transitions within a LL subset emerging from the same subband that change the LL quantum number by $\Delta N = +1$ (black transition markers). In the axial model and the

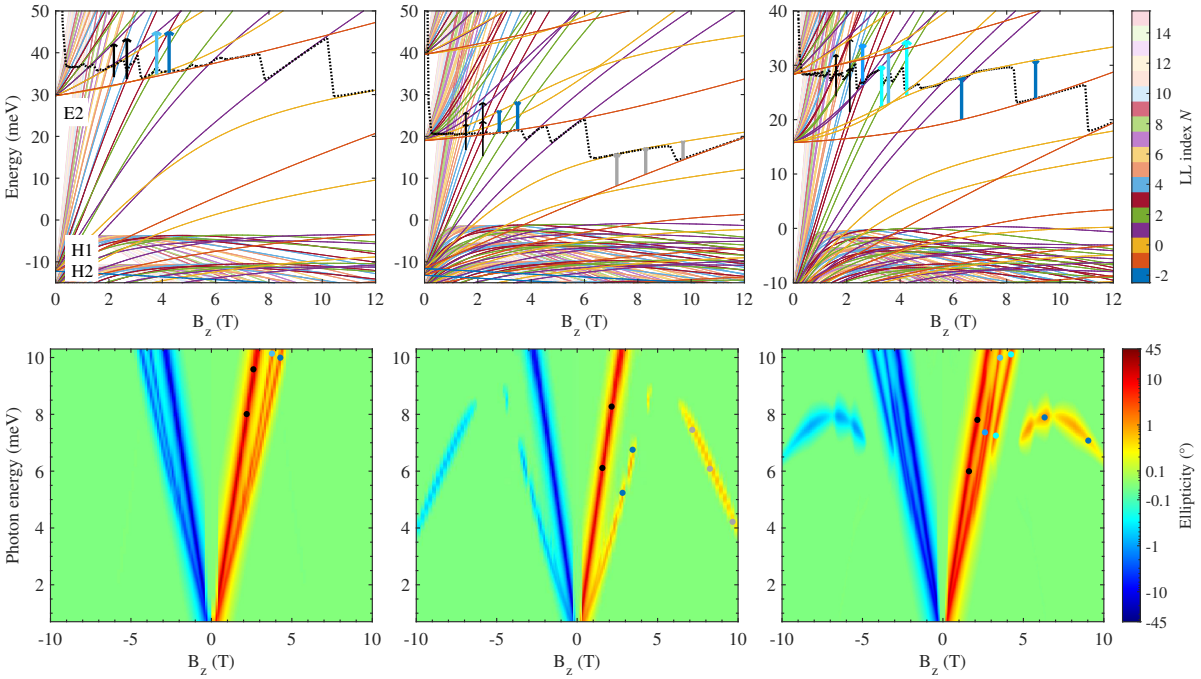

Fig. 5.2.: Calculation results for measurements of Figure 5.1 (from left to right: 30, 45 and 58 nm HgTe layer). Top row: Magnet field dependence of LL states in the axial approximation. Black dotted lines show the ECP, vertical arrows correspond to the transitions responsible for the features marked in the respective calculated spectra in the row below. Black arrow correspond to transitions between states evolving out of H1 valence bands, while shades of blue correspond to states evolving from E2 conduction bands. Subband labels are given in the 30 nm case (compare to Figure 4.2). Note the reduced energetic splitting between subbands with increasing layer thickness. Calculations [C7, C8, C9].

low magnetic field range required for the comparison with the measurements, the transition energies in the H1± subband LL fans are effectively degenerate, with respect to the observed broadening, even though the energy levels themselves are non-degenerate. These transitions are thus observed as a single line in all measured spectra.

The observed splitting of the CR-like features is due to the filling of the conduction band states. While these transition are still within only one subband (either E2+ or E2-), the LLs with higher quantum number N evolve differently than for H1 states: Transitions involving states with higher LL indices N still collapse on top of each other to strong CR-like modes, that have slightly different slopes for each subband (transition markers in different shades of blue).

States with low LL indices however, have a clearly distinguishable magnetic field dependence and the energetic difference of LLs with $\Delta N = \pm 1$ can give rise to the non-linear features that are observed at higher magnetic fields. Two examples are the $N = -1$ to $N = 0$ transitions in the E2 subbands of the 58 nm HgTe layer (dark blue markers) and in the H1 subbands of the 45 nm HgTe layer (gray markers). The existence of such unusual features in spectra is thus not linked to the so-called topological interface/surface states (i.e. the H1 subbands), as also bulk conduction bands can give rise to similar features. However, due to their peculiar shapes, these features show up far away from quasi-degenerate CR modes and are rather easy

to identify in experimental and computed spectra. This identification of single transitions and the LLs that cause them allows for detailed discussion of the influences of model parameters and symmetries in subsequent sections.

The features indicated by dark blue markers in the calculations for the 45 and 58 nm layers have a modulated elliticity intensity. This is caused by fluctuations in the occupation of the initial (45 nm) and final (58 nm) transition states. For example, in case of the 58 nm layer, around $B_z \approx 6\ T$ the $N = 1$ LLs of the H1± subbands cross the partially filled $N = 0$ states of the conduction band, which are the final states of the transition. Generally, with increasing magnetic field the degeneracy of all LLs states increases, but as the total number of electrons in the system is constant, the partial filling of the "final" state gets lower. This leads to an increase of the overall transition strength. But when the filled $N = 1$ bands cross above the partial filled band, these become first partially filled and continue to empty with rising magnetic field. At the same time, the final state of the transition becomes more occupied again, which decreases the strength of the transition. Such effects could potentially be used to determine the position of LL state crossings and the effective electron temperature, but the noise level of experimental data does not allow to resolve such fine details.

Discussion of envelope functions

Transitions between the ± sets of the subbands are not observed within the range of detectable ellipticity, as the matrix elements in the Kane Hamiltonian which would allow for such transitions are only weak, whereas transitions between even and odd subband index sets are "forbidden" by the opposite z-parity of the involved envelope functions.

Figure 5.3 shows example envelope functions for the bulk band crossing surface states calculated for a 45 nm thick HgTe layer. Transitions only take place between states in the same row of the figure. Transitions between states of the same column are not allowed by the $\Delta N = \pm 1$ selection rule, while transitions connecting the four states diagonally would fulfill the LL selection rule, but the integrated product of transition operator and the respective envelope function pairs cancel out due to multiplication of antisymmetric and symmetric functions with respect to the growth direction z.

Note that the surface state wavefunctions (Figure 5.3) are equally localized at both interfaces, as the structure is fully symmetric. Thus, the expectation value $\langle z \rangle$ of all eigenstates is exactly zero in this high symmetry model. This changes upon inclusion of structure inversion asymmetry (see section 2.1.5 and section 5.2.3).

For thin HgTe layers the envelope functions of the surface states extend well throughout the layer, with a notable probability also in the center of the layer. Thicker layers show a clearer separation of two surface probability maxima, but a finite probability remains in the layer's center, even for the largest thicknesses that can be grown with reliable strain using molecular beam epitaxy (MBE), see Figure 5.4.

In contrast to the notable interface character of surface states, the bulk valence and conduction band states envelope functions are localized throughout the bulk, as depicted in Figure 5.5. In analogy to the solutions of a simple particle-in-a-box problem the subbands with the lowest indices have more weight in the center of the well, whereas higher indices are related to higher kinetic momentum and a higher probability distribution also closer towards the interfaces.

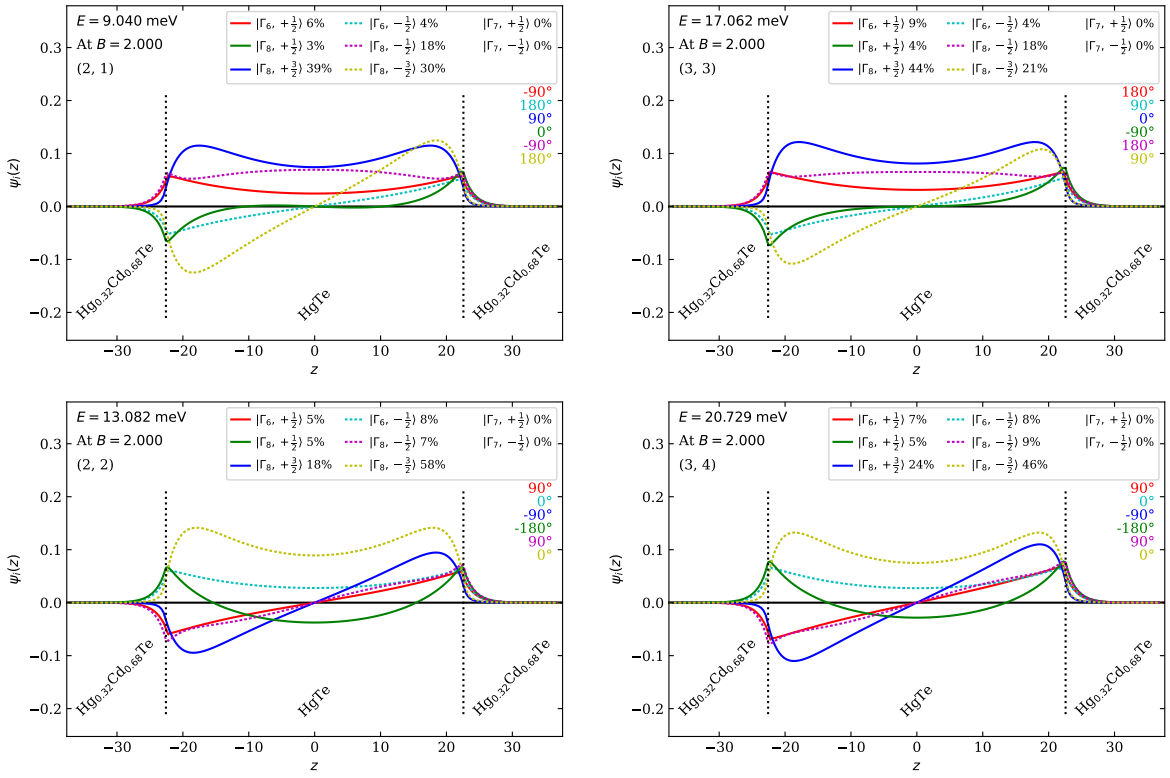

Fig. 5.3.: Eight-orbital envelope functions for surface states of a 45 nm HgTe layer at $B = 2$ T for Landau levels $N = 2$ (left) and $N = 3$ (right). Top/bottom rows show states from the +/- dominant total angular momentum sets (evolving out of the H1+/- subbands at $\boldsymbol{k} = 0$). Complex-valued orbital functions of z have been phase-shifted to real amplitudes with phase shifts given for each orbital in matching colors at the right. The total integrated weight for each orbital is given in the legend. Numbers to the left of the legend denote the eigenvalue, magnetic flux density, LL number N and an arbitrary band sorting index (assigned automatically by `kdotpy`). Output generated by `kdotpy`[37].

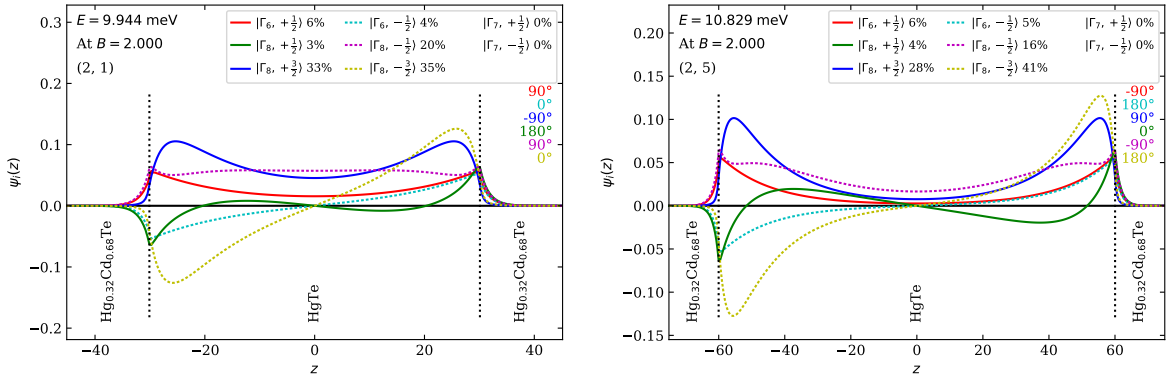

Fig. 5.4.: Eight-orbital envelope functions for surface state LL $N = 2$ at $B = 2$ T for 60 nm (left) and 120 nm HgTe layers (right). Analog to top left panel of Figure 5.3.

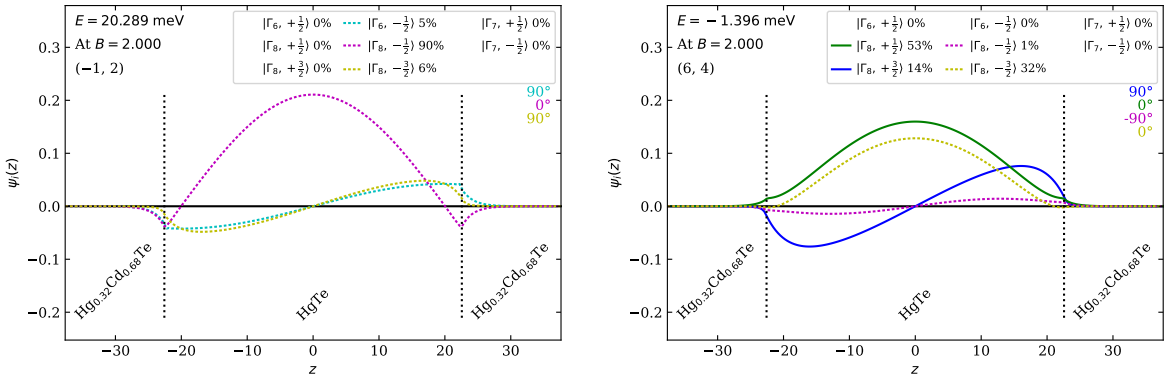

Fig. 5.5.: Eight-orbital envelope functions for bulk band states at $B = 2$ T for lowest energy conduction band LL (left, $N = -1$) and highest energy valence band LL (right, $N = 6$). These states evolve out of the E2- and H2 subbands at $\boldsymbol{k} = 0$, respectively.

Gate voltage dependence

When tuning the gate voltage applied to the samples, the charge carrier density inside the mercury telluride layer is changed and another ECP is required to describe the new filling of LL states.

However, in the current level of approximation, the electrostatic potential caused by the gate voltage does not enter the Kane Hamiltonian. Thus, the calculated bandstructure and LL magnetic field dependence remain unchanged. Only the occupation of states changes.

Figure 5.6 shows that for larger n-type charge carrier densities the spectra are still well described by the pure axial model. Most characteristic for the influence of gating is the changed occupation of the E2 subband LLs “-1” and “0” (dark blue markers). The transition between these LLs are notable in the spectral range of the THz setup for all measured samples with a thickness of 45 nm and larger.

With higher n-type charge carrier densities no further similar features are observed in the spectra, as the distinctive “-1” to “0” LL transitions in higher conduction subbands require photon energies higher than accessible with this setup to show the characteristic bow like shape. In fact, these transitions are part of the measured signal in lower magnetic fields, where they show an almost linear field dependence (see green, magenta and purple markers). Other transitions that can be measured in the given energy range also show up as CR modes, however the slope is slightly different for the subbands and especially for their lowest LL transitions. Due to broadening the single lines are mostly not identifiable. In existing publications concerning optical spectroscopy of mecury telluride samples [20, 34, 36, 92, 93], these transitions are thus often treated as CR modes of a single population of electrons with effective parameters for the electron effective mass m_e and the Drude scattering time τ_D. These parameters are then fitted to the data and depend on other parameters as the charge carrier density (or gate voltage) and temperature.

The $\boldsymbol{k} \cdot \boldsymbol{p}$ model on the other hand does not generally rely on fitting, but with suitable material parameters and known layer dimensions has a predictive power which covers the important trends without further input. The variation of effective parameters m_e and τ_D can be explained and calculated directly, even from the axial symmetry version of the model.

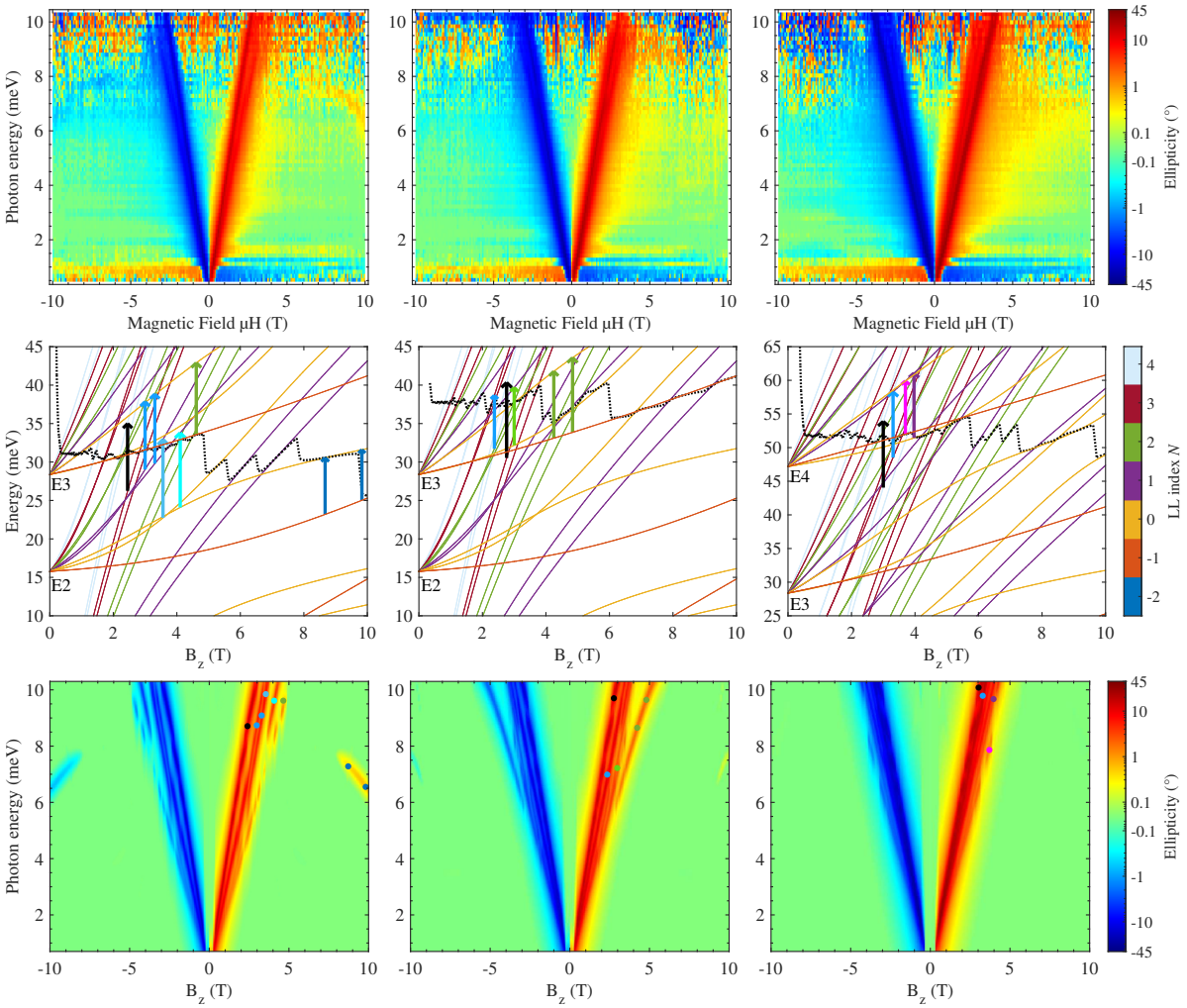

Fig. 5.6.: Gate voltage dependency for a 58 nm HgTe sample. Top to bottom: Measured spectra, calculated LL bands (only shown up to $N = 4$ for clarity), calculated spectra. Charge carrier densities from left to right: $(1.0, 1.3, 2.1) \cdot 10^{12}$ cm^{-2}. Selected transitions have been marked in the calculation plots, where the marker and arrow colors are related to the subband set as: H1 (black), E2 (shades of blue), E3 (shades of green), E3 (magenta and purple). Details are given in the text. Data from [D9], calculations from [C10].

Mismatches

While the axial model generally gets the qualitative feature evolution of the samples right, there is often a difference in the energetic position of some of the spectral features by less then 1 meV. Given that fact, that the material parameters for CdHgTe have been established decades ago with methods offering less precision than THz spectroscopy, this level of accuracy is quite remarkable.

In some rare cases, as for the 45 nm HgTe layer in Figure 5.2, the mismatch can get larger. In this specific example the “-1” to “0” LL transition of the E2 subband has steeper slope in the measured spectra. Further larger differences can also be found for “-1” to “0” transitions in the E3 and H1 subbands of a 58 nm HgTe layer (Figure 5.6 (green markers) and Figure 5.7

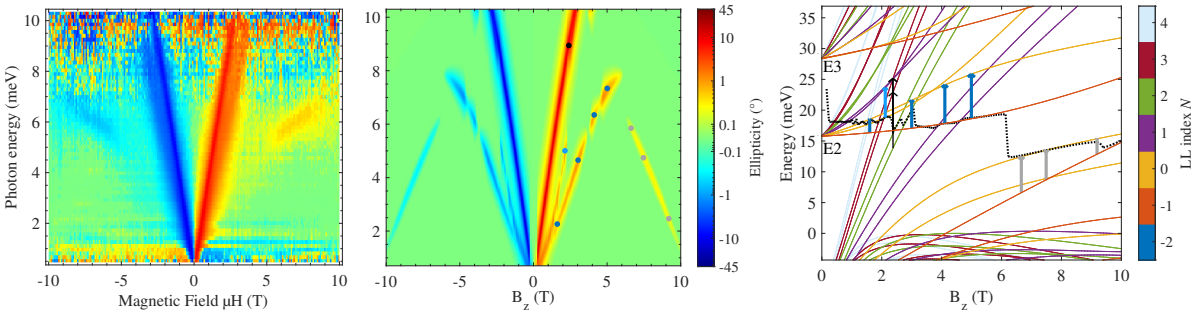

Fig. 5.7.: Mismatch between measured and calculated spectra, when ECP is in the bulk band gap. From other gate voltages, one can conclude that the E2 band LLs are not filled at high magnetic fields. Data from [D9], calculations from [C10].

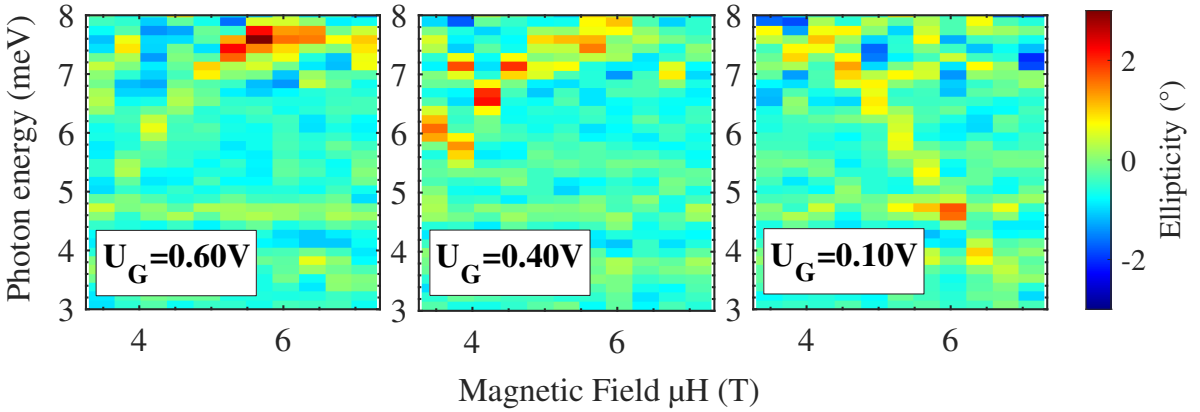

Fig. 5.8.: Low resolution data for a 70 nm HgTe layer sample from [D10]. n-type charge density decreases with lower gate voltages. The sample has a high quality but could not be measured again with better resolution due to issues with contacts and gating. The measurement series did only include the displayed magnetic fields, so no zero field offset correction could be applied here. Nevertheless, characteristic features as the bowed E2 "-1" to "0" transitions (left and middle pane) and the diagonally descending H1 "-1" to "0" (right panel) are observable.

(gray markers)), but not for its E2 subband.

The crossing of the H1 "-1" LL through the H1 and H2 "0" LLs should be a prominent feature in both THz and magneto-transport (LL fan chart) measurements. While in all LL fan chart measurements of 70 nm HgTe layer samples this crossing is missing[1], the spectral signature predicted by `kdotpy` can be found in measurements on a 70 nm sample with high mobility (see right panel in Figure 5.8) and the 45 nm sample shows a perfect match for the the spectral signatures of the involved LLs (see Figure 5.1 and Figure 5.2, grey markers). For the 30 nm sample, the energetic splitting is too large to have a transition observable in the spectral range of the instrument.

It is plausible that the origin of these mismatches lie in the energetic position of the "-1" LLs. This LL state may only contain contributions by three of the eight basis orbitals (see

[1] This summarizes the results of many measurements done at the chair of EP3 up to first half of 2022. As briefly mentioned in section 2.1.7, LL state crossings in such measurement can be lifted by small anti-crossings due to in-plane magnetic fields. A detailed investigation of this effect is ongoing.

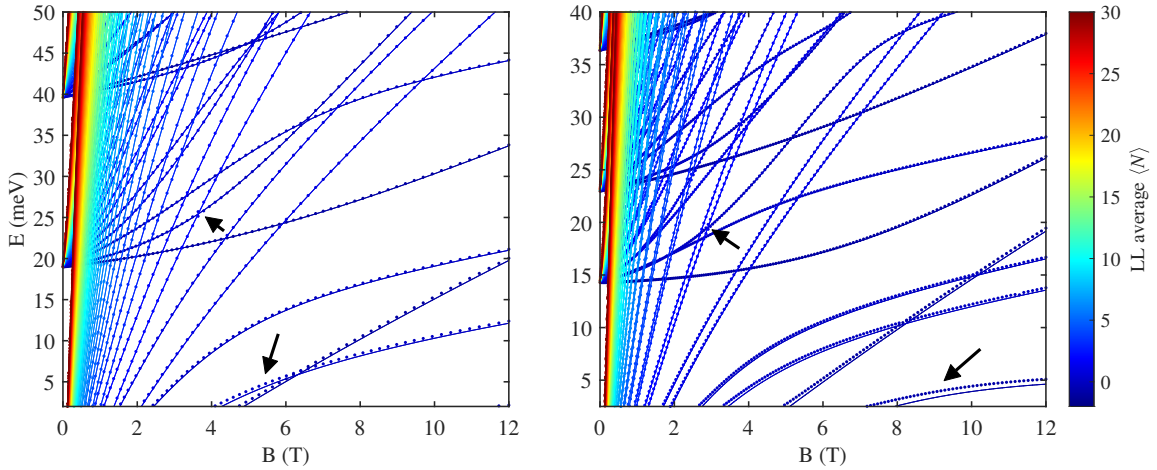

Fig. 5.9.: Comparison of LL magnetic field dependence in axial symmetry (full lines) and asymmetric (dots) model including valence band anisotropy and bulk inversion asymmetry. Calculated for 45 (left) and 70 nm (right) HgTe layers in the energetic range of the bulk band gap and conduction bands. Black arrows point to the largest deviations in each region.

eq. (2.27)) and the energy eigenvalue is not as much influenced by off-diagonal orbital interaction terms in the Hamiltonian. Therefore, the influence of electrostatic potentials entering on the main diagonal could be higher for these LLs compared to ones with higher indices N. Other than material parameters, the electrostatic potentials in the HgTe layers can be very different between individual samples, which would explain why the mismatch of these features is different throughout the investigated samples. Further discussion on electrostatic potentials continues in sections 5.2.3 and 5.3.

Another observation concerns the broadening of transitions in the spectra. Especially in comparison to the thinner samples in Figure 5.1, the measurements on the 58 nm sample show generally a larger broadening of features and for higher carrier densities the features seem to bleed out also towards higher magnetic fields (compare to Figure 5.6). This is not covered by the $\boldsymbol{k}\cdot\boldsymbol{p}$ model directly, but is due to increased disorder and the reduced carrier mobility in older samples of lower growth quality. Those broadening effects are not linked to the layer thickness, but for the thinner samples discussed here, better material quality has been available at the time of investigation. By the time of writing this thesis, thicker samples are also available with equally high quality and similar sharp spectral features.

5.1.3. Asymmetric models

In recent work on mercury telluride systems an often raised question concerns the inclusion of higher order asymmetry terms in the Hamiltonian [36, 93, 94]. The investigation of structure inversion asymmetry by inclusion of electrostatic potentials is, due to its complexity, postponed to section 5.2.3.

In this section the results of the axial model is compared against a model that includes both valence band anisotropy (i.e. $\mu \neq 0$ in eq. (2.23)) and bulk inversion asymmetry terms (see eq. (2.29)). Therefore, all important material specific asymmetries have been accounted for to the lowest order of momentum $\boldsymbol{k}$.

Figure 5.9 shows the eigenvalues relevant for samples with pure n-type charge transport in magnetic fields up to Landau levels with index $N = 30$ for both the axial model, as well as the model including asymmetries. Independent of the LL number both calculations yield practically the same results. Towards the valence band edge the energetic differences increase, but for both layer thicknesses reside well below 1 meV.

At some of the crossing LLs (examples marked by upper black arrows), the inclusion of asymmetries creates a small avoided crossing. Here the energy eigenvalues deviate slightly from the axial approximation also in the conduction subbands, but the differences can not be resolved with the energy resolution given by the THz spectrometer. Such avoided crossings do not occur in the axial approximation, as the Hamiltonian has no interaction terms between different LL states, making the Hamiltonian block-diagonal with respect to LL eigenstates. This changes upon inclusion of asymmetry terms, which add interaction between every forth (with anisotropy) or even every second (with bulk inversion asymmetry (BIA)) axial eigenstate.

It is actually quite notable that the addition of asymmetry terms does barely change the eigenstates of mercury telluride conduction bands. While the name *valence* band anisotropy implies that the conduction bands are not concerned, this is not quite correct in a system with inverted band structure. From Figure 5.5 it is clear that conduction band states are dominated by Γ_8 light hole orbitals, which are getting additional interaction terms through anisotropy (R in eq. (2.22)) and BIA (eq. (2.32)).

While the intermixing of orbitals rises for both valence and conduction subbands with higher LL indices, the energy differences between interacting states are larger in the conduction band. Similarly, the surface states have a similar orbital mix as valcence band states, but are well separated from other states, as soon as they leave the valence bands to cross the bulk band gap. When treating the asymmetry terms perturbatively on top of the axial eigenstates, the energy correction does not just depend on the matrix elements of the participating unperturbed eigenstates, but also scales inversely with the energy difference of those states. Thus, the energetic density of states also determines the influence of higher asymmetry corrections.

As most of the terms added by asymmetry scale with $k_\pm$ which are replaced by latter operators $a^\dagger, a$ in the Landau level picture and thus scale with the magnetic field strength, the effects are also small when energetic differences between LLs become smaller in lower magnetic fields.

For the description of samples that show n-type conductance, a more complex model including anisotropy and bulk inversion asymmetry is not required. Here, the axial approximation is therefore a good way to drastically reduce the required computational effort with minimal implications for the validity of the solution.

In section 5.2.2 the quality of the axial model outside of the pure n-type regime will be reviewed.

5.1.4. Conclusions about topological insulator properties

From analysis of experimental and calculated spectra in the previous sections one may summarize the persistent presence of CR mode like spectral signatures. The analysis of the underlying LL magnetic field dependence shows that these signatures are caused by LL transitions in the conduction band states, if the charge carrier density is high enough[2], but also always[3] from

[2]The exact density required to start filling conduction band states depends on the layer thickness but for investigated samples is typically on the order of $n \approx 5 \times 10^{11}$ cm^{-2}.

[3]In the gateable charge density range of all investigated samples, these features are at least partially observable in any measurement. This is also discussed in following sections.

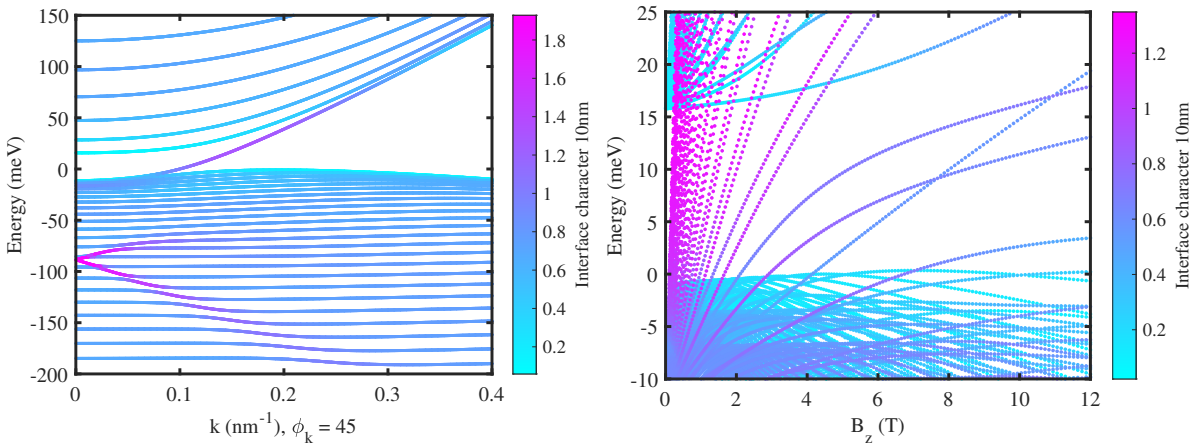

Fig. 5.10.: Interface character of eigenstates calculated for a 58 nm HgTe layer given by the probability density within 10 nm around the interfaces, normalized by the integral of a homogeneous probability density in the same area. This property is available as observable in `kdotpy`. (Left) Subband dispersion along [1 1 0] direction at zero magnetic field [C11] and (right) LL state magnetic field dependence [C10].

bulk band gap crossing states.

Figure 5.10 shows that these states are indeed interface states. However, neither the calculated dispersion nor the magnetic field dependence show clear signs of Dirac state physics *inside* the bulk band gap. Dirac like linear dispersive state can be found buried under valence band states and these states hybridize with each other.

But the surface state in the band gap has a quadratic dispersion character, very similar to the conduction band states. Another characteristic of quadratic dispersion can also be found from the LL magnetic field dependence, which is close to linear[4]. This linearity directly translates into the linear magnetic field dependence of CR modes, which are confirmed by measured spectra not only in the THz range, but also using Fourier transform infrared (FTIR) methods[5].

The linear k-dispersion of Dirac states, however, is linked by Peierls substitution to LL energies $E_n \propto \sqrt{nB}$ (where n is the LL index). Thus, LL transitions of Dirac states would not scale linear with magnetic field as the observed CR mode like spectral features do.

Nevertheless, a range of publications within the past years claimed to have observed Dirac states in tensile strained mercury telluride *bulk* layers [20, 27, 29, 30]. Reference [27] shows linear dispersive states within the valence bands in angle-resolved photoemission spectroscopy (ARPES) data from a 1 µm HgTe layer, but from the available data, no conclusions about the actual dispersion of bulk band crossing states could be made. Following publications analyzed the $1/B$ phase offset of Shubnikov-de-Hass oscillations or quantum Hall plateau steps in magneto-transport [30] and microwave transmission (resonator geometry) [20, 29] experiments.

In all cases, the authors find an unusual value of $(\pm)\frac{1}{2}$ they associate with Dirac state Landau

[4] Avoided crossings between different subbands for LLs with the same index are a cause for non-linearity of LLs. Furthermore, only the LL state $N = -2$ consists of just one orbital LL, whereas $N > -2$ states are built from multiple orbitals which weights are changing with variation of magnetic field. Therefore, only the $N = -2$ LL is expected to be truly linear.

[5] FTIR measurements are currently conducted by Dr. Leonid Bovkun and Vladimir Marković and yet unpublished.

levels[6] [10], instead of the usual zero phase expected from normal quantum Hall effect (QHE). Unfortunately, various errors have been made in the analysis:

In Figure 3(d) of [30] the fits are forced to a fixed offset at $-\frac{1}{2}$ and are not a true least squares fit to the presented data points and error bars. Furthermore, the assigned Landau-level indices are in contradiction to the figure caption and raw data (presented in Figure 1) and must be offset by +1. With correct data analysis, one obtains the normal zero phase offset.

In Figure 4(c) of [29] the issue is again in the fit to the data. Error bars are not plotted, but from Figure 4(b) one can see that the oscillation amplitude is larger for small values of $1/B$ and the minima can be assigned with higher precision. Thus, the linear fit should weigh those data points more than those for larger $1/B$. In fact, data points in Figure 4(c) do not follow a strict straight line, but there is some curvature. Fitting of small $1/B$ values also yields a zero offset rather than $\frac{1}{2}$.

In [20] both of the above issues play a role[7]. Generally, one needs to be cautious about extrapolation from LL index vs $1/B$ data, as the magnetic field position can shift from the usual regular $1/B$ spacing when the energy difference of LLs is smaller than the thermal or LL state broadening.

The three band model[8] constructed by references [27, 30, 95] may be useful in the absence of magnetic fields, but Figure 5.10 and Figure 5.11 clearly demonstrate that the interface character of current carrying states inside the "bulk band gap" slowly vanishes with increasing magnetic field. The conductive surface area at low magnetic fields is gradually transformed into a conductive bulk state. Due to the magnetic field, currents are forced onto a circular orbit, leading to the development of a two-dimensional edge channel in the center of the layer. Thus, high enough magnetic fields can force the 3D Topological Insulator into a 2D Quantum Hall system.

A clear separation into different subsystems is thus not possible in higher magnetic fields, instead the system must be considered as a whole. As a consequence, the interpretation of magneto-optical and magneto-transport data should rather be based on a suitable $\boldsymbol{k} \cdot \boldsymbol{p}$ model instead of effective reduced band models.

5.1.5. Summary

So far the capabilities of the time-domain THz method in conjunction with $\boldsymbol{k} \cdot \boldsymbol{p}$ calculations have been demonstrated. The `kdotpy` package allows to directly calculate the ellipticity spectra for a given charge density in the sample. Without the use of fitting parameters, the results match very well with the measured spectra.

[6] In a true electron-hole symmetric Dirac system, the Dirac point is also the charge neutral point and the zeroth LL has no magnetic field dependence. This LL is thus both electron and hole state. The other way round this implies that only half of the density of states of the zeroth LL is available for electrons, which causes the offset. In graphene it has been experimentally observed [26]. However, in HgTe, the origin point of the linear dispersion is not equal to the charge neutral point (CNP) and there is no electron-hole symmetry to begin with. In fact, the actual Dirac point in tensile strained mercury telluride thin films is buried around 0.1 eV deep into the valence bands and its states do not contribute in magneto-transport experiments.

[7] The focus of this paper lies on the observation of a quantized topological magneto-electrical Faraday rotation. However, reference [A1] shows that such an universal quantization can not be observed in the used sample's layer stack. The observed constant rotation value at large magnetic fields is just the low-frequency limit of the rotation caused by the CR modes and can have any value, depending on state occupation and scattering times. Similar rotation curves can be picked from the data recorded for this work.

[8] This effective model consists of non-interacting top and bottom surface states independent from an insulating bulk with separate carrier populations that may be gated independently.

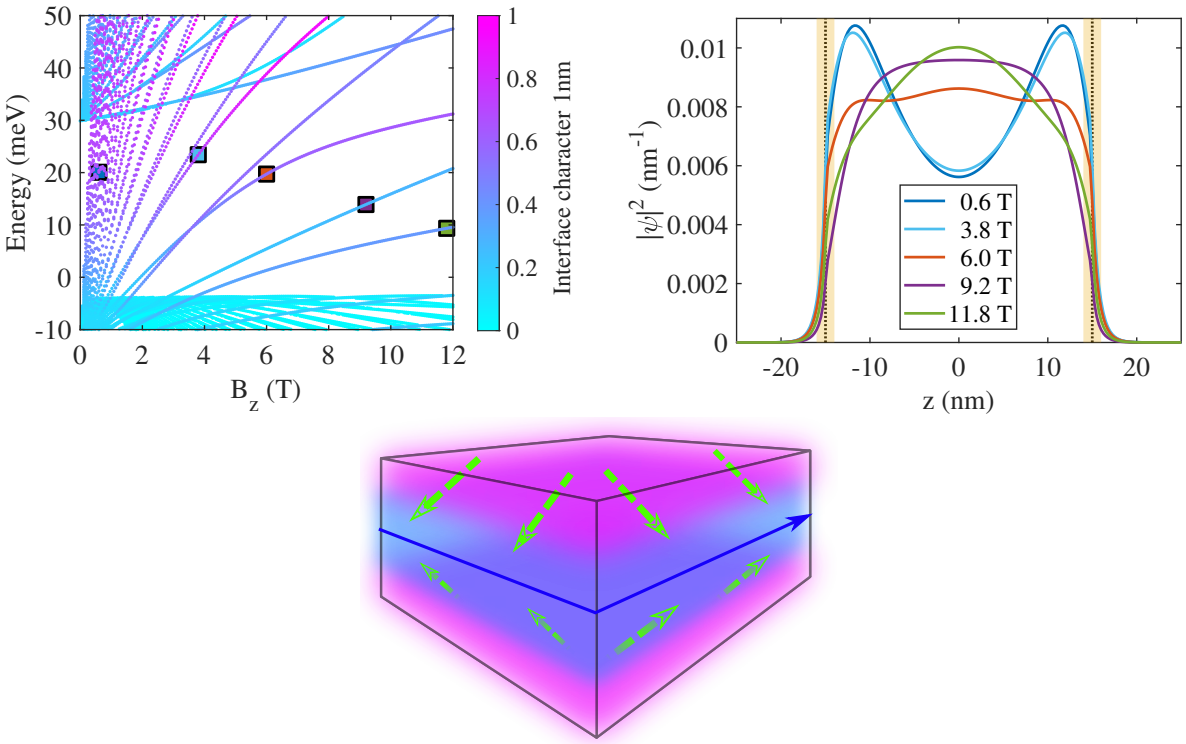

Fig. 5.11.: (Left) Interface character of eigenstates calculated for a 30 nm HgTe layer given by the probability density within 1 nm around the interfaces, normalized by the integral of a homogeneous probability density in the same area. This property is available as observable in `kdotpy`. Markers highlight eigenstates of which the envelope functions are shown in the right plot: The shown states are picked at roughly equal energy or charge density in the layer and show a change in the localization from the interfaces towards the center of the layer. The dotted vertical lines denote the interfaces of the HgTe layer and the interface integral region for the probability density shown in yellow. (Bottom) Pseudo-3D side view of the HgTe layer. Green arrows symbolize how the current carrying states evolve from interface localization (purple) towards the 2D quantum hall state limit (blue helical edge channel) at high magnetic fields. Calculations from [C12].

It was further shown, that for conduction band states an axial symmetry model is sufficient to achieve high accuracy, even in the case of a partially inverted band structure of strained mercury telluride layers. Since such a model does not require large computation resources, it is recommended to use it over other effective models with a strong focus on idealized topological insulator properties that can be found in the literature [12, 28, 30, 95]. Not only are some of these models based on inaccurate assumptions, they also serve merely as a tool to explain a subset of measurements and lack predictive power outside fitted regions.

The $\boldsymbol{k} \cdot \boldsymbol{p}$ model delivers much more insight into the band structure and eigenstates. As the envelope functions are also calculated, they can be used to gain further insight into the localization of states under investigation (see e.g. Figure 5.3) or to calculate any observable[9]

[9] In principle it would also be possible to simulate ARPES spectra [38]. However, this feature is not yet part of `kdotpy`.

that can be defined in terms of the orbital basis eq. (2.21).

Based on the calculated band structure and LL eigenstates, one may clearly separate features connected to states near the surface from other contributions originating from bulk band states, whenever they show up at different photon energies. This provides a method for direct verification of the existence of states, instead of having to estimate weights of different states in CR modes [28].

Notable deviation of measured spectra from theoretically predicted ones could be found with samples that also showed comparably low quality in magneto-transport measurements. The parasitic doping from growth adds at least an a priori unknown electrostatic background potential which requires further modeling. In the worst case, the material composition is altered far enough to require changes to the basic band parameters of the $\boldsymbol{k} \cdot \boldsymbol{p}$ model (see table 2.1).

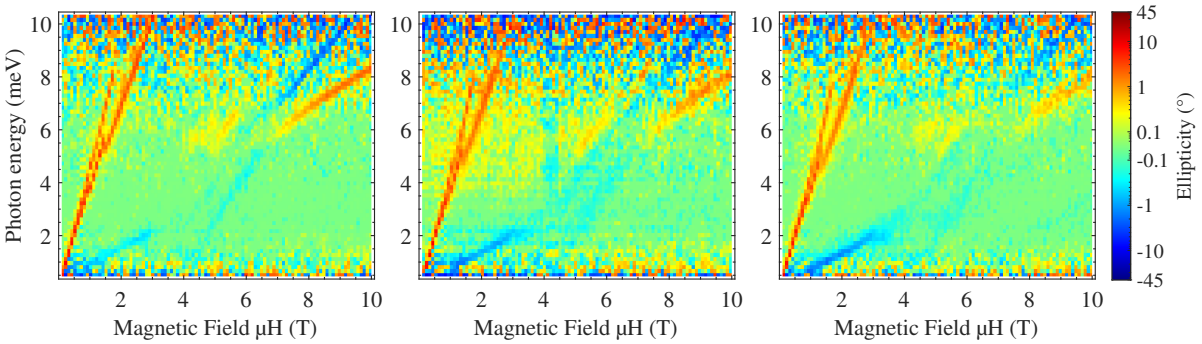

Fig. 5.12.: Measured ellipticity spectra for small charge densities around the CNP for a 30 nm layer of HgTe. The ECP is lowered from left to right, i.e. the sample is gated more towards p-type. Charge carrier densities from left to right: $n \approx 1 \cdot 10^{11}$ cm^{-2}, charge neutral, $p \approx 1 \cdot 10^{11}$ cm^{-2}. Data from [D7].

5.2. Surface states at the charge neutral point

5.2.1. Introduction

While the previous section focused on the region where the sample shows n-type behavior in transport experiments, the data and discussions presented here now revolve around the point of charge neutrality in the sample. This point is reached by application of more negative gate voltages as before.

In transport experiments, the samples start to show signatures of coexisting opposite charge type populations in the HgTe layer (see e.g. Fig. 5 in reference [69]), while in the THz ellipticity spectra features with opposite helicity appear, as shown in Figure 5.12. From now on, we restrict ourselves to showing only positive magnetic fields, as the spectra are still fully antisymmetric with magnetic field, but the focus is now put more onto single features.

For simplicity and clarity, only one layer thickness is discussed at this point. The 30 nm HgTe sample is chosen, as it has a high sample quality in terms of feature sharpness in optical spectra, as well as the highest mobility measured with VdP ($> 10^6$ cm^{-2}). This sample also has a larger gating range, compared to the 45 nm sample with similar quality. Apart from that, the trends observed in both samples are very similar, but scaled to different energies due to the dependence of the band structure on confinement energy.

As in the the n-type region, there still is a CR mode like signature with positive ellipticity. Even though the bulk conduction band is already depopulated, there still is a prominent splitting visible.

While the linear low magnetic field dependency of the strong feature with negative ellipticity up to 2 meV resembles very much a classical hole-type CR mode, it can not be explained from a quasi-classical model, why the ellipticity amplitude drops abruptly for magnetic fields larger than about 3 T.

Since the a Drude based model directly fails to explain the measurement, the $\boldsymbol{k} \cdot \boldsymbol{p}$ model is again used to gain more insight into the magnetic field dependence of the eigenstates and optical transitions in between them. In the next sections the quality of solutions obtained for different levels of asymmetry in the Hamiltonian is discussed in detail.

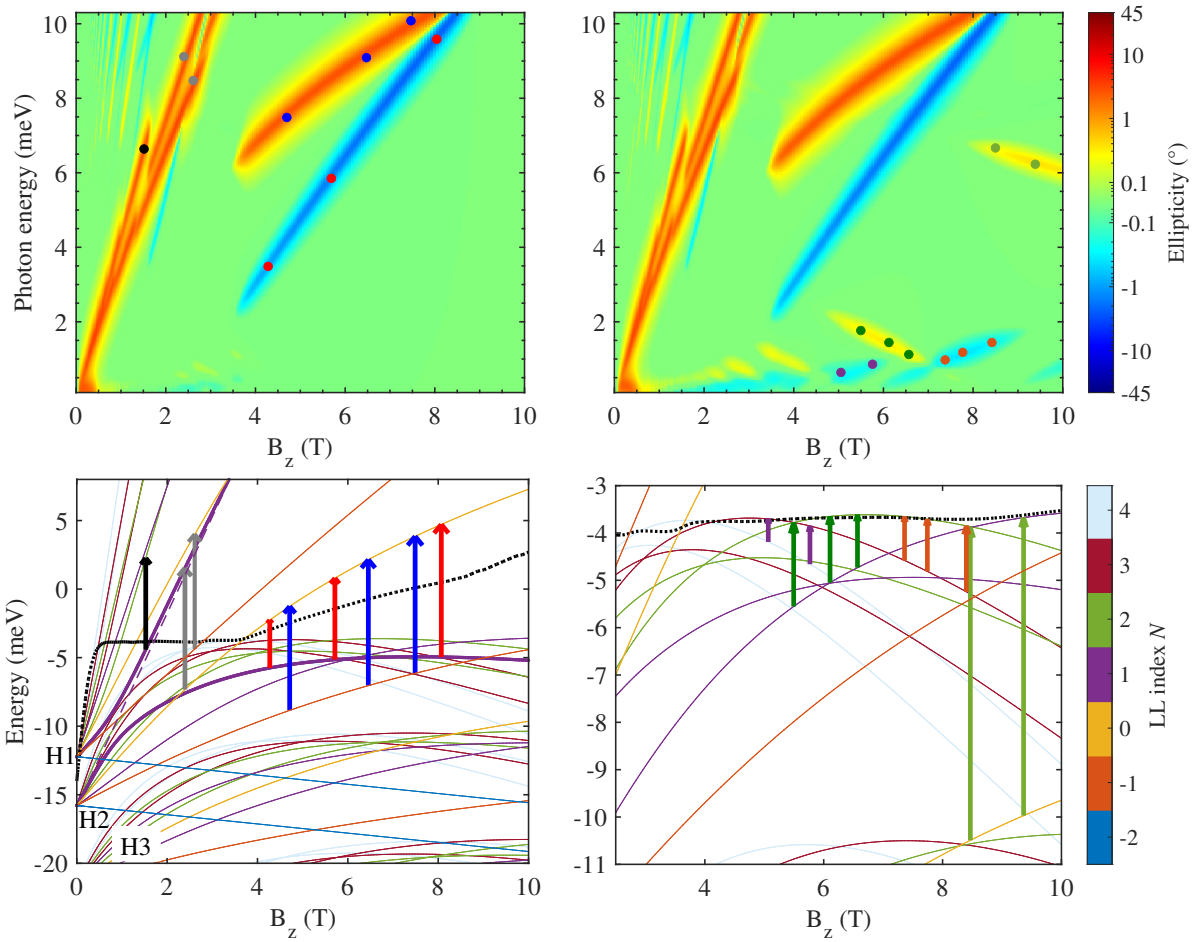

Fig. 5.13.: Calculated spectra (top) and LLs (bottom) for a 30 nm HgTe layer in axial approximation exactly at the CNP (left) and with slight ($p = 10^{11}$ cm^{-2}) p-type charge majority (right). Since the LL structure does not change, the p-type case focuses on the new transitions appearing when the ECP lowers into the valence bands. In the bottom left pane an avoided crossing between $N = 1$ bands has been highlighted by thicker lines and dashed tangential line. LLs above $N = 4$ are not shown for clarity. Calculations from [C13].

5.2.2. Breakdown of the axial model

While the axial model is sufficient to describe the sample when the ECP is away from the valence bands, the calculated spectra in Figure 5.13 clearly deviate from the experimental observations in Figure 5.12. Only the "n-type" CR mode like feature is reproduced rather well.

As long as the ECP is still above the valence bands, in case of charge neutrality or small n-type charge dominance in the sample, the dominant spectral features are foremost due to LL $\Delta N = +1$ transitions in the H1 and H2 subband LL states (black and blue markers).

As the valence subbands are very close in energy, states with the same LL index N have an avoided crossing at low magnetic fields ($\lesssim 1$ T), intermixing the H1 and H2 band characters. This allows for additional transitions (gray markers), responsible for the observed "splitting" of the CR mode like features. It is also the reason for the inverted LL order of the $N = 0$ and

$N = 1$ levels even at higher fields[10], which allows for transitions with opposite helicity (red markers).

As soon as the uppermost valence band states become partially emptied by lowering the ECP, many additional distinctive transitions are predicted from the axial model. These are characterized by falling/rising slope, positive/negative ellipticity signatures in the calculated spectra. They arise due to the interplay of the gradient in state occupation versus energy and the curvature of the LL magnetic field dependence.

The low energy transitions with dark green markers are discussed as example: At about 5 T, the $N = 2$ LL starts to provide some empty final states for the transmission and the spectral signature becomes visible. With rising magnetic field, the energetic difference between the initial $N = 1$ and the final $N = 2$ LLs reduces. While the transitions strength generally increases with smaller energy difference due to the $1/\Delta E$ scaling, the thermal occupation factors of both states also get more similar. This increases stimulated emission, reducing the total absorption factor of the transition. Futhermore, at 7 T another transition feature is crossing with opposite helicity (orange markers), reducing the observable ellipticity near the crossing point. Below a photon energy of about 1 meV in Figure 5.13, the feature continues to fade out until the crossing point of the involved LLs is reached at 8.5 T. The inverted states then enable transitions with negative ellipticity (visible in the spectral plot at 0.7 meV and 10 T in the bottom right corner).

Due to the strong intermixing of H subband states, there is also a transition from the H3 subband LL with $N = 0$ to the H2, $N = 1$ LL predicted from the axial model (green markers above 10 T). This is possible as the H2 and H1 states for $N = 1$ are intermixed and the H1 and H3 envelope functions have the same parity with respect to the growth axis z.

Even in the axial approximation there are more allowed transitions from valence band states due to the stronger intermixing of orbital and subband character, but the new spectral features do not line up with the experimentally observed transition energies. The axial symmetry is thus not sufficient to describe the sample properties outside of the n-type charge regime.

There is, however, one observation that can be made even in the axial approximation which explains the observed two-carrier behavior in charge transport experiments [69]. In the lower left panel of Figure 5.13 the sample is in a charge neutral state and the black dotted ECP line is identical to the CNP. This does not mean that there must be no charge at all in the HgTe layer, but only that n- and p-type charge carriers must have the same density. At high magnetic fields, the ECP is energetically far away from Landau levels, so at low enough temperatures, there are no free n- or p-type charges in the system and the layer becomes insulating. Towards low magnetic fields, the energetic density of states is much narrower and even with just small thermal broadening there will be some states filled above the ECP and some empty states below. Therefore, there will be both n- and p-type charges available for transport in the HgTe layer and no insulating behavior can be observed. This is a direct consequence of the topological band inversion, giving rise to bulk band gap crossing surface states.

5.2.3. Asymmetric models

While additional asymmetry terms do not notably influence the eigenstates above the valence band edge (compare to Figure 5.9), this is very different for the valence band states themselves. Due to the narrow energetic spacing of those states and the strong intermixing of orbital and

[10] The $N \leq 0$ LLs have only one heavy hole orbital contributing to the eigenstate ($|\Gamma_8, -\frac{3}{2}\rangle$, see eq. (2.27)), which is also dominant at low magnetic fields. Therefore, interaction between such states is drastically reduced compared to higher LLs.

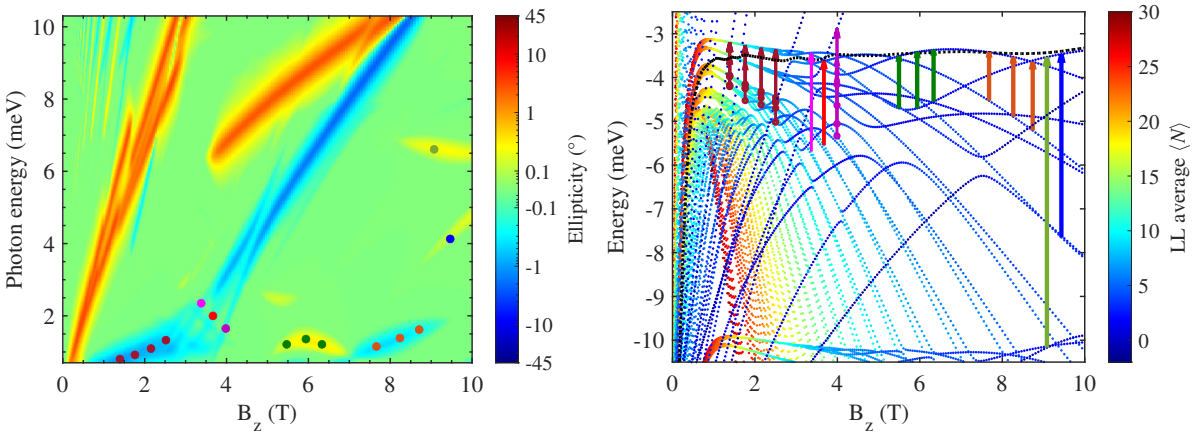

Fig. 5.14.: Calculated spectra (left) and LLs (right) for a 30 nm HgTe layer including valence band anisotropy with slight ($p = 10^{11}$ cm^{-2}) p-type charge majority. Since the LL structure does not change for higher energy states, the focus is on the upper valence bands with low energy transitions. In the low magnetic field region groups of four eigenstate bands are bunched together. Circular markers are added at the inital states where multiple transition arrows overlap. Calculations from [C14].

subband character, additional interaction terms in the Hamiltonian have a huge influence on the eigenstates.

To the author's knowledge, the only other publication that investigated the influence of symmetry lowering effects in p-type layered mercury telluride samples is reference [94]. The layer thicknesses investigated there ($\leq$ 11 nm) are in the quantum well (QW) regime where confinement energy splits the subbands far apart, thus lowering the interaction strength of different states. While the authors still calculate significantly different transitions with respect to the axial model, the general structure of LL states does not change and differences in spectra are mostly due to additional avoided crossings.

The following discussion on models including more symmetry lowering effects for thicker HgTe layers shows that the intuition one might gain from analysis of QW samples can be misleading and changes of the LL structure are much more dramatic here.

In the following, more and more asymmetry terms in the $\boldsymbol{k} \cdot \boldsymbol{p}$ model are taken into account and the effects onto the LL structure and calculated ellipticity spectra are discussed in detail for each step.

Valence band anisotropy

Considering the valence band anisotropy in the Kane Hamiltonian only changes the matrix element R, by allowing the term $\mu \neq 0$ in eq. (2.23). This minor change of the Hamiltonian destroys the block-diagonal character of the Hamiltonian with respect to the LL index, allowing for interaction and intermixing of the axial eigenstates. As the LL index N is not a conserved quantity anymore[11], the coloring of eigenstates with respect to the involved LLs is instead given in terms of the expectation value $\langle N \rangle$. The `kdotpy` observable name is `llavg`.

In the calculated spectra plot of Figure 5.14, notable changes occur mostly in the low energy range, while the results for higher energies are similar to the axial solution. The CR mode

[11] In an anisotropic system, angular momentum in general is not a conserved quantity anymore.

like feature is still caused foremost by transitions between LLs inside surface state bands (see black and grey markers in the axial calculation shown in Figure 5.13). Due to their surface localization, the interaction with the valence band states is reduced. The other two prominent features at higher magnetic fields and energies are also very similar to the axial version, with some additional signatures of avoided crossings.

The magnetic field dependence of the eigenstate energies in Figure 5.14 is focused on the upper valence band edge. At large magnetic fields, it resembles the axial approximation, with additional avoided crossings of some bands[12].

Towards lower magnetic fields the contribution of higher LL indices dominates the topmost valence band states. The interactions from the additional Hamiltonian term lead to a bunching of four eigenstate bands into practically four-fold degenerate single bands. In this region, the intermixing of axial states is so strong that the representation in terms of subband Landau levels and transition selection rules is not beneficial anymore for a transparent discussion[13].

Transitions between these bunched state bands all effectively decrease the LL indices from involved initial to final states and result in spectral signatures with negative ellipticity. The linearly increasing splitting between the bunched bands therefore gives rise to the CR mode like feature tagged with maroon colored markers in Figure 5.14. Upon increasing the magnetic field strength, the band bunching slowly breaks up and the eigenstates transition back into the single LL configuration of the axial symmetry. Transitions between the involved states are still possible (magenta, red and purple makers), but the spectral features smear out energetically and don't form a pronounced line as before. This explains the abrupt end of the CR mode like feature that was discussed for experimental data in section 5.2.1.

In higher magnetic fields transitions in between valence band states yield very similar features to the axial solution. Dark green markers show again transitions from states with dominant $N = 1$ character to such with $N = 2$. Due to avoided crossings between the inital states, the resulting shape in the spectral plot is now bowed instead of linear. The changing Landau level weight of eigenstates due to avoided crossings further enables additional transitions which have not been possible before (e.g. dark blue marker).

Even with the notable changes due to the reduced symmetry, the experimental spectra can not yet be reproduced. While the appearance of the CR like mode with negative ellipticity that gets less pronounced also at about 3 T is an indicator that the model evolves in the right direction, the magnetic field slope of the mode and most other features still do not match.

Bulk inversion asymmetry

With the addition of BIA, the remaining rotational symmetry around the magnetic field axis is only two-fold and every second LL couples in the Hamiltonian. As can be seen in the plots of eigenstates energies versus magnetic field (bottom panels in Figure 5.15), the increased interaction enforces the bunching of eigenstates into four-fold quasi-degenerate bands even more. The highest valence band eigenstates only unbundle notably above 6 T, but even then do not follow along the same paths as the axial approximation (compare to Figure 5.13).

The energetic splitting and slope of the bunched bands in the low magnetic field regime also

[12] The remaining four-fold rotational symmetry around the magnetic field axis couples every fourth LL, which leads to the observed avoided crossings.

[13] This does not imply that the selection rules are broken, but since an eigenstate is just not a single LL anymore with well defined parity of the envelope functions, the full picture is just very convoluted. The fully numerical calculation of transition matrix elements for arbitrary pairs of eigenstates does not rely on an interpretation along selection rules and still yields precise results.

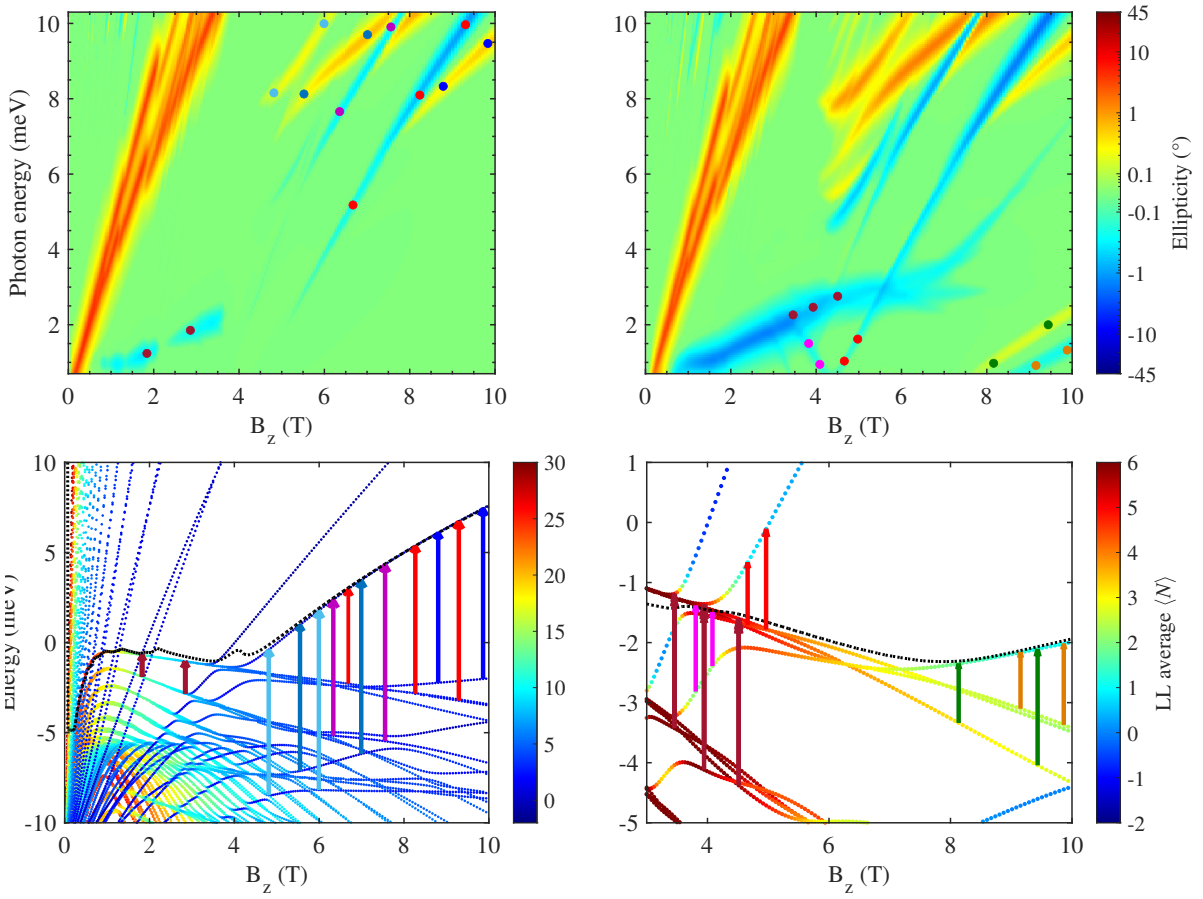

Fig. 5.15.: Calculated spectra (top) and eigenstates (bottom) for a 30 nm HgTe layer including valence band anisotropy and BIA with $n = 10^{11}$ cm^{-2} (left) and $p = 10^{11}$ cm^{-2} (right) total charge densities. In the p-type case, where the ECP enters the valence bands, the focus lies on the additional transitions enabled in between those bands. The colormap is adjusted to promote the evolution of the LL character for these bands. Calculation from [C15].

increased compared to the previous model including valence band anisotropy. The energy and magnetic field position of the CR like mode with negative ellipticity (maroon markers) now matches well with the experimentally observed values, e.g. they both show resonance at 2 meV photon energy with applied magnetic flux density of 3 T.

Drastic changes in the spectra are observed for larger photon energies: While in the previous models the transitions of $N = \pm 1$ valence band states into the $N = 0$ surface state (red and blue markers in Figure 5.13) have shown only two prominent features (apart from the CR like modes), there are now a lot more transitions. The red and blue markers in Figure 5.15 show again transitions into the $N = 0$ surface state[14] from the Landau level contributions with $N = \pm 1$ to the valence band eigenstates. The ordering of these spectral signatures is now inverted within the detectable energy and magnetic field range[15] and due to the bunching of states, the spectral signatures merge into a single line below 7.5 T. Both features fade out

[14] This state has a LL weight higher than 99 % as long as it is more than about 2 meV above the valence band edge.

[15] Whereas in axial approximation the crossing of those features happens at higher photon energies.

towards lower magnetic fields as the LL contribution to the initial states shifts to higher N, whereas the final state remains at $\langle N \rangle = 0$ up to the point where it enters into the valence bands. For the left case in Figure 5.15 with slight n-type charge, the final state additionally gets filled, such that the transitions fade out earlier. These signatures can be identified in the experimental spectra and will be discussed further below.

The strong intermixing of LLs and subbands enables further transitions from deeper valence band states (purple and lighter blue markers). In the axial approximation this energy region is filled with states of H2 and H3 subband character, but these labels do not make much sense in this context of strong intermixing. The spectral signature of transitions from such lower energy states is not easily identified in the experimental data. An avoided crossing similar to the one marked by lighter blue markers around 9 meV photon energy in Figure 5.15 can also be observed in experimental data around 6 meV (compare to Figure 5.12), but is also much less prominent and extended. This mismatch is assigned to the higher importance of parameters defining the off-diagonal orbital coupling in the Kane Hamiltonian in the dense state region. The discussion on $\boldsymbol{k} \cdot \boldsymbol{p}$ parameters is continued in section 5.2.4.

Once the ECP is lowered enough to depopulate the upper valence band states, few additional transitions happen in between bunched states that unbundle at high magnetic fields (orange and green markers). The polarity and strength of these features depend much on the LL composition of the involved eigenstates, which changes slowly for all states even at high fields.

Most features that have been visible before gain increased contrast as the final $N = 0$ state filling is further reduced (e.g. red markers). Similarly, the maroon markers show extending signatures due to more unfilled bunched states. A further interesting signature is caused by the avoided crossing of the $N = 0$ state with the valence bands. The part that continues along the original axial approximation course provides initial states for transitions into partially empty upper valence bands (magenta markers). Due to the strong intermixing of LL contributions in the eigenstates, the resulting ellipticity for transitions on both sides of the avoided crossing (magenta and red markers) has the same negative sign. For a simple crossing as in axial approximation the ellipticity would flip sign instead, as the LL characters of bands do not

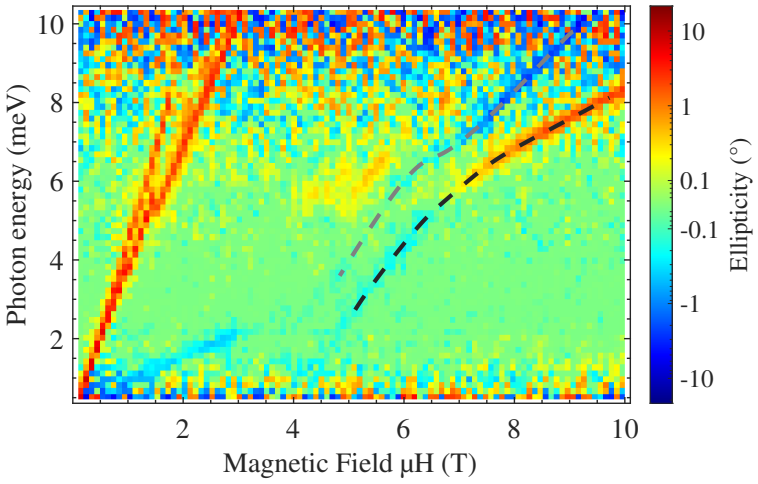

Fig. 5.16.: Measured ellipticity spectra for small charge density ($n \lesssim 10^{11}$ cm^{-2}) in a 30 nm layer of HgTe. Dashed lines have been added as guide to the eye along two continuous transition features. Data from [D7] (same as in Figure 5.12).

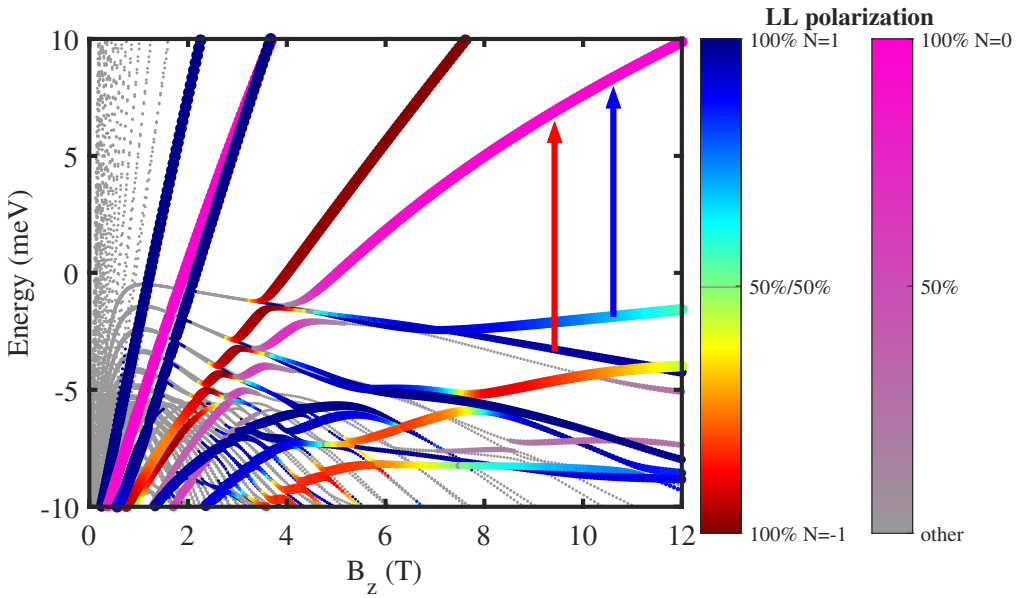

Fig. 5.17.: Alternative color coding of eigenstate magnetic field dependence (same data as Figure 5.15). Marker size increases with sum over LL weights with $N \in [-1, 1]$. The $N = \pm 1$ polarization of states from the odd LL index basis set is given by the first colormap (red to blue), while for states of the independent even LL index basis set the $N = 0$ weight is given in a gray to magenta colormap. Arrows (red and blue) mark the transitions relevant for the discussion. Calculation from [C15].

change in the axial case and the roles of final and initial transition states swap.

In a general comparison of experimental spectra with the calculated ones using different levels of bulk symmetry, the current model clearly shows the best agreement. But apart from comparing spectral signatures, there are also some strong indicators in the experimental data that BIA is required for explanation. Figure 5.16 highlights two transition features with dashed lines. Especially the black dashed line can be identified to be caused by transitions between a single pair of initial and final eigenstates[16] (blue arrow markers in Figure 5.15 and Figure 5.17). The observed ellipticity of this transition slowly changes from a negative sign at low magnetic fields to a positive sign at 7 T.

Such a change of the ellipticity can only be understood when considering a system with reduced symmetry, where eigenstates may be constructed using every second LL index state as basis[17]. Only then a transition between a single pair of eigenstates may have transitions involving both photon polarities. For the feature highlighted by the black dashed line, the initial state consists dominantly of $N = \pm 1$ LLs allowing for $\Delta N = \mp 1$ transitions into the final state which has more than 99 % $N = 0$ LL weight. The net sign of the ellipticity signal is not just given by the dominant LL weight, but the whole integrated transition matrix element has to be taken into account, as the LL contributions to the eigenstates may have different z-distribution and weights in the transition operator.

As can be seen in Figure 5.17, the band of eigenstates from which the transitions (blue arrow

[16] This becomes even clearer once structure inversion asymmetry (SIA) is introduced. Compare to Figure 5.19.

[17] This is the case when the rotational symmetry around the magnetic field axis is reduced to a two-fold symmetry. Such a situation can be obtained by layer growth on a low symmetry substrate plane (compare to [45] or, in case of the high-symmetry [0 0 1] substrate used here, by explicit consideration of the BIA.

marker) emerge changes the LL polarization

$$P_{\mathrm{LL}} = \frac{w_{+1} - w_{-1}}{w_{+1} + w_{-1}}, \tag{5.1}$$

where w_N denotes the weight of LL with index N in the eigenstate. With increasing magnetic field P_{LL} changes from a dominant $N = 1$ character and negative transition ellipticity towards an intermixed state with more $N = -1$ content which contributes a positive ellipticity signal.

Therefore, the inclusion of BIA adds a lot of value towards the correct interpretation of the spectra obtained from p-type samples and the underlying bandstructure. There are still notable differences, e.g. the clearly separated black and gray dashed lines in Figure 5.16, where the calculated initial eigenstates for those transitions overlap to a single line in Figure 5.15 and Figure 5.17 (transitions indicated by red and blue arrows). The following section delivers an explanation for such differences.

Structure inversion asymmetry

The observed splitting between black and gray marked transitions in Figure 5.16 motivates lowering the model symmetry even further. While bulk symmetries are already accounted for, the symmetry along the layer growth axis z is inherently broken by the single sided presence of a gate structure and its electric fields extending through the layer stack.

A clear indication for the relevance of electrostatic potentials caused by gating is shown in Figure 5.18. Tuning the gate voltage does not only change the filling of states and thus the visibility of transitions, but also shifts the photon energies of observable transitions. For such an effect, the gate voltage dependent electrostatic potential distribution inside the sample must be considered in the Hamiltonian.

This additional potential also lifts degeneracies between top and bottom surface states, causing surface eigenstates to localize at one interface instead of both (compare to Figure 5.3). It enables the use of the $\langle z \rangle$ localization observable for coloring each eigenvalue[18] to gain more insight into where states are localized and how this is influenced by potentials and other parameters.

[18] Technically this is always possible, but structure symmetry of the envelope functions enforces $\langle z \rangle = 0$ for all states. In such cases `kdotpy` offers `interfacecharacter` observables to distinguish interface from bulk states.

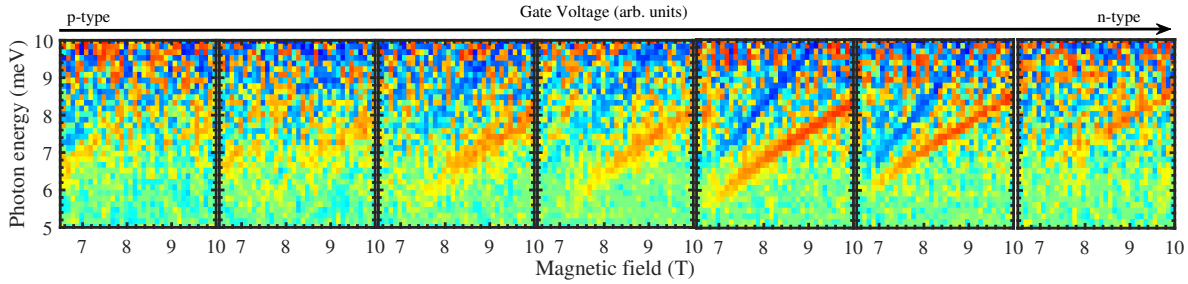

Fig. 5.18.: Measured ellipticity spectra for small charge densities (from $p = 1.7 \times 10^{11}$ cm^{-2} to $n = 1.9 \times 10^{11}$ cm^{-2}) in a 30 nm layer of HgTe. A shift of transition energies with varying gate voltage is observed. Color map as in Figure 5.16. Data from [D7].

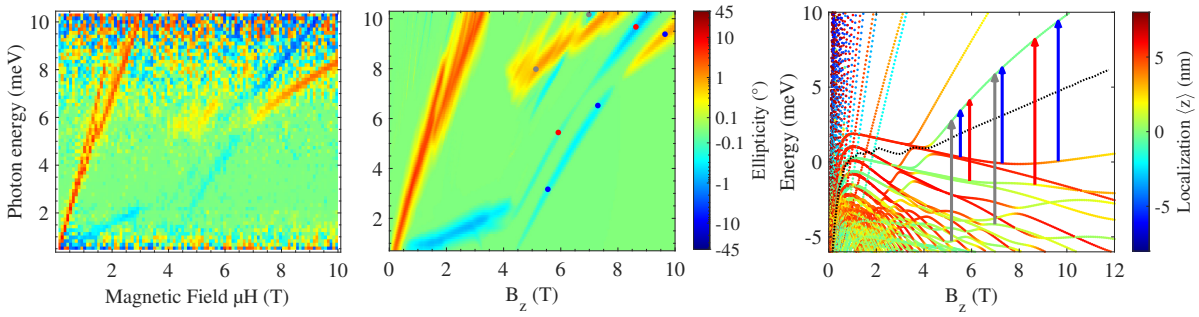

Fig. 5.19.: Calculated spectra (center) and eigenstates (right) for a 30 nm HgTe layer including bulk and structural asymmetries with zero net charge carrier density. The asymmetric toy potential located at the top interface splits the four-fold bunched valence band states into two sets. One set localizes closer to the top surface and has increased energy eigenvalues, while the other set remains mostly centered in the bulk with less changes in energy. This results in the separation of the transitions features (red and blue markers) also in the spectral plot. Deeper lying valence bands are also affected and the transitions signatures (gray markers) are further split. Left figure: Experimental spectra (same data as Figure 5.16) for comparison. Data from [D7, C16].

Figure 5.19 shows the results of a calculation using a one-sided toy potential. This potential has the value of +20 meV at the top HgTe interface[19] and decays quadratically to zero within 12 nm from the interface. The exact shape of the potential in the top barrier does not notably influence the result of the calculation, as long as it is 'well behaved', i.e. does not show discontinuities and is smaller than the potential well barriers given by the material band parameters. For simplicity of construction the potential is modeled symmetrically around the interface.

Inside the HgTe layer such a potential shape is equivalent to a potential caused by a homogeneous positive charge distribution in the upper 12 nm. While this surely does not represent the actual charge distribution in the HgTe layer, it is not totally out of line with the expected accumulation of charge in a top-side gated system. One should keep in mind that this toy potential calculation has a proof-of-principle character.

Comparing with experimental spectra in Figure 5.19 and Figure 5.18 one can see that the calculated photon energies do not match accurately, but the trends are now matching well: The splitting between the two transition features tagged with red and blue markers is reproduced with the same order of magnitude by the addition of electrostatic potentials. The upper one of both features has a strong negative ellipticity signature at high magnetic fields, fading out towards lower fields with a minimum in between, while the lower one has the dominant positive ellipticity at high magnetic fields which changes slowly towards negative ellipticity at smaller fields. The additional potential also moves the point where ellipticity flips sign towards a higher magnetic field of 8 T, indicating that also the LL weights of the eigenstates change with applied potential.

Furthermore, increasing either the penetration depth to 14 nm or the strength of the potential to +25 meV (corresponding to more negative gate voltage and stronger p-type charge doping), the photon energy of the transition tagged with blue markers is lowered by less than 0.5 meV.

[19] Since the electron potential is obtained by multiplication of the electrostatic potential with charge $-e$, the positive electron potential sign corresponds to negative voltages applied to the top gate. This is in line with the negative gate voltages required to reduce the intrinsic n-type charge density inside the samples.

Also, the splitting between the two transitions is increased. These trends are very much in line with the observed movement of bands in Figure 5.18.

Thus, it can be concluded from experimental spectra and the toy potential model, that the electrostatic potential in the HgTe layer plays another important role. It is however not straightforward to determine the correct potential landscape in the layer and this discussion is continued in section 5.3. The strength of potentials required to induce those subtle changes in the transition spectra is lower than [30] or comparable to [36, 69] previously suggested potentials for similar samples.

5.2.4. Quality of $\boldsymbol{k \cdot p}$ parameters

In the previous sections the agreement of the $\boldsymbol{k \cdot p}$ model and its various levels of asymmetry with measured spectra have been reviewed for samples gated close to the CNP. While the most asymmetric models cover many of the interesting trends observable in the measurement, there are also larger differences in the energetic positions of some transitions. In the calculated spectra (see Figure 5.15 and Figure 5.19) those features have been identified to have deeper lying valence band initial states but the same bulk band gap crossing $N = 0$ finial state as other states, for which a good match has been observed.

For the conduction bands and gap crossing states it can be seen from section 5.1.3, that the eigenstates do not depend much on additional interaction terms in the Kane Hamiltonian. Actually, most of the off-diagonal parameters can be set to zero while preserving the overall structure of the solution. Adjusting the basic material parameters such as band gap energies and offsets as well as strain and layer thickness has direct consequences for the bulk band gap, subband confinement energies and effective masses. These quantities are accessible by many experiments and the current parameter set has been used successfully in countless publications on mercury telluride materials systems to give a good match with observed values. Therefore, the above mentioned parameters can be considered good enough to start with.

However, in the bulk valence band the high density of states makes the off-diagonal parameters much more important and at the same time complicates the targeted measurement of the inner details of the valence band structure[20]. All off-diagonal parameters depend directly on either Luttinger parameters γ_i, κ, Kane element P (compare to eq. (2.23)) or BIA terms (see eq. (2.29)).

The BIA parameters for HgTe have only been established rather recently from density functional theory (DFT) calculations and require verification by experimental data. Under supervision of the author, Moritz Siebert thus tried to obtain a better set of parameters from fitting calculated spectra to experimental data as part of a Bachelor thesis. It turned out, that not only is the available set of BIA parameters well suited to explain the transitions between newly formed bunched bands (see Figure 5.15, maroon markers) quantitatively, but other parameters do not improve the energetic mismatch of the transitions from deeper valence band states. The largest influence on calculated spectra is obtained from $\Gamma_8 - \Gamma_8$ interaction parameter C_8, followed by $\Gamma_8 - \Gamma_6$ interaction parameter B_8^+ with much weaker sensitivity. The parameters B_8^- and B_7 did not show any notable influence on the spectra within a reasonably large range. The importance of the C_8 parameter for the THz spectra can be understood by orbital character analysis of the states near the band gap. The Γ_8 orbital has the dominant weight for all states, followed by a minor intermixing with Γ_6 in the conduction bands (compare to Figure 4.2). The

[20] The author is not aware of any publication specifically treating the valence band properties in mercury telluride thin films (30 – 100 nm).

Γ_7 states are far remote and intermixing with those orbitals is negligible at the band gap[21].

The Kane and Luttinger parameters are also not quite well known for mercury telluride. Landoldt-Börnstein [96] lists quite different sets of parameters obtained from various methods. Unfortunately, these parameters are not totally independent from each other [32]. However, the large spread of possible values motivates to test these parameters first for a set of values producing a better match with data.

Two key points need to be taken care of, when trying to obtain a new set of material parameters:

The energetic range that is investigated should cover a much larger window and the fitted values must yield a good approximation not just in the limited energetic window of THz spectroscopy. To this end, a new FTIR spectrometer has been set up at the chair of *Experimental Physics III* by L. Bovkun and V. Marković to carry on the investigations started in this thesis.

An even bigger question mark must still be put on the electrostatic potential landscape in HgTe layers. As can be seen from the previous section, the structure inversion asymmetry (SIA) also causes notable changes in the band structure. In following sections there is also a discussion about sample qualities in general. Only with recent improvements in the MBE growth process the sample quality increased and reduced the influence of electrostatic potentials through unwanted doping charges. It thus makes sense to focus on modeling the newest and cleanest samples first, possibly in a situation where potentials can be completely neglected. After having established a more precise set of material parameters, one may come back to model the more complex situations with potentials involved. Section 5.3 gives an outlook over the challenges to overcome when potentials are not negligible.

5.2.5. Conclusions about other experiments

From Figure 5.19 one can already gain further insight about the properties of the sample near the CNP and qualitatively explain the response to certain measurement methods.

Comparing to magneto-transport measurements [69, 97], the $\boldsymbol{k}\cdot\boldsymbol{p}$ model not only covers the observed results, but sheds some new light onto the interpretation of the data.

A prominent feature in Figure 5.19 is the emergence of massive Volkov-Pankratov [5] interface states from the bulk valence bands, when positive electrostatic potentials (corresponding to negative gate voltages) are introduced to the model's interfaces. In reference [69], deductions about the charge transport properties of such Volkov-Pankratov (VP) states have been made using a two-carrier model, where topological surface states and VP states are independent populations with fixed densities over the magnetic field range. The bulk is considered insulating in the model. An important observation is the presence of different Hall slopes in low and high magnetic fields. The populations' mobilities are evaluated from fitting Hall and longitudinal resistance data at zero magnetic field, further using charge carrier densities evaluated at higher magnetic fields. However, the underlying model equation does not cover the full extend of the presented Hall resistance curve, e.g. the magnetic field, where the slope changes sign, is predicted to be at higher values than observed in the data (see Figure 5 of [69]).

The $\boldsymbol{k}\cdot\boldsymbol{p}$ model does not interpret the sample in terms of independent fixed density populations, but only one total charge density can be meaningfully defined over the full magnetic field range. From the measured spectra, it is known that the effective broadening of LL states is typically less than 1 meV without a notable magnetic field dependence. Starting out at large magnetic fields in Figure 5.19, it is clear, that no states are close to the CNP with respect

[21] To investigate the remote bands and their relevant parameters, other methods with larger spectral range are required, e.g. a FTIR spectrometer.

to broadening and the sample is insulating in high fields. Going towards smaller magnetic fields, the energetic difference towards LLs gets smaller, until electron and hole states become populated due to broadening and the sample becomes conductive. For the situation presented in reference [69], the ECP actually sits much below the CNP, due to the large hole density. Therefore, at large magnetic fields, there are no electron states close enough to be filled and the total charge density is just the hole density. In the limit of small magnetic fields, the energetic spacing of the LLs is again much smaller and states above the CNP are within the energetic broadening around the ECP. Thus, the total charge density has still the same p-type value, but the additional presence of free electrons in the surface states is compensated by an equal amount of additional valence band carriers[22]. In the magneto-transport signal, the n-type contribution dominates the total signal, as the relevant surface states have smaller effective masses and thus higher mobilities compared to the topmost valence band states.

Another set of interesting magneto-transport measurements can be found in the doctoral thesis of V. Müller [97] (section 9). There, the influence of a combined top and bottom side gating is discussed along a model using independently gateable populations of top and bottom surface states (topological and massive VP states), as well as bulk states. Unfortunately, this simplified nearly free carrier bands model does not cover the essential physics well enough to describe the sample accurately in the presence of moderate to high magnetic fields. While in magnetic fields up to about 2 T the LL fan charts show a complex pattern with respect to both gate voltages, the pattern becomes much simpler at fields above about 3.5 T. Such behavior can already be understood qualitatively from the $\boldsymbol{k} \cdot \boldsymbol{p}$ model: Both gates influence the sample in terms of two parameters: Each gate voltage change is associated with a change of total charge carrier density inside the sample, proportional to the respective gate action factor (defined by insulator material properties and thickness). I.e. both gates change the same ECP valid for the whole HgTe layer. Additionally, both gate voltages also influence the electrostatic potential of the sample, as they define different electric field boundary conditions on top and bottom interface. This in turn changes the band structure and the LL energies up to few meV. A more detailed analysis of the top and bottom gate influences follows in section 5.3, around Figure 5.21. In presence of large magnetic fields, the splitting of LLs is typically larger than the changes caused by different gating situations and thus the pattern of LL vs. both gate voltages follows along equal charge density lines. For small magnetic fields however, the energetic differences between LLs are smaller (especially in the valence bands and top/bottom surface states). By changing the potential landscape, some of the LLs can come close to each other and even cross. As the magneto-transport measurement essentially keeps track of the filling of the measured LLs and not their energetic positions, the trace of voltages required to keep the ECP within a LL band can give rise to the observed complex patterns.

It can be summarized that the $\boldsymbol{k} \cdot \boldsymbol{p}$ model is also a powerful tool for the interpretation of magneto-transport data. Interestingly, the conclusions about the effect of gating on the top and bottom surface states are quite different in existing publications compared to the one given by the $\boldsymbol{k} \cdot \boldsymbol{p}$ model. In fact, the two surface states can not be gated totally independent, but due to the complex band structure of thin mercury telluride layers and the missing energy resolution of magneto-transport measurements, it is at least cumbersome to tell apart the fine but important details in the measured datasets [95].

[22] In the given scenario with strong p-type conductance, this only happens at very small magnetic fields < 0.2 T and is not resolved accurately with the limited number of LLs used for Figure 5.19. The zero magnetic field k-dispersion plot (Figure 5.10) illustrates this case better: Due to the indirect band gap, and the large density of states of the valence bands, there still will be filled band gap crossing states, while at the same time, the top valence band states are depleted.

Modeling the band structure of mercury telluride layers using independent effectively free carrier Drude models only works in simple limit cases. This can be seen from references [36, 93]. While for sufficiently thin HgTe QWs an isotropic reconstruction of the band structure from CR mode analysis works fine, it fails for thicker layers with smaller confinement energies. Much of a physicists intuition about analysis of QHE and LL fan charts has been developed in the regime of narrow QWs and large confinement energies. But in case of thicker HgTe layers, the confinement energy scale no longer dominates orbital interactions and the effects of asymmetry and strain, giving rise to non-linear magnetic field dependence of LLs and overlapping of different carrier type LL fans. Therefore, some of the extrapolation techniques and interpretations do not work out as simple as before.

5.2.6. Summary

The discussion of samples gated close to charge neutrality and their topologically inverted bandstructure shed first light onto the challenging level of detail that realistic models must cover. Whenever surface state or bulk valence properties are to be investigated in an experiment, simplified models fail to reproduce the real bandstructure. Even though changes happen "only" on the scale of few meV, this is enough to completely[23] rearrange the eigenstates of the system over a large magnetic field range from close to zero to at least 10 T (compare Figure 5.13 and Figure 5.15).

The inherent asymmetries of bulk valence bands already play a large role in the emergent two-carrier behavior of thin-layer HgTe samples at low magnetic fields and charge densities.

Adding SIA to the model by means of electrostatic gate potentials further splits the bands not only energetically, but also changes their localization with respect to the layer growth direction (see Figure 5.19). This opens the model for studying the emergence of Volkov-Pankratov (VP) out of bulk states, but also raises the question how to clearly assign the term "surface" state to some of the eigenstates, while their localization changes steadily in magnetic fields.

The time-domain THz polarimetry method proves to be an invaluable tool for investigation of the properties of the eigenstates in the magnetic field with unprecedented resolution. Apart from the identification of the required $\boldsymbol{k} \cdot \boldsymbol{p}$ Hamiltonian symmetry level, some of the unique spectral features clearly act as "smoking gun" signatures for the presence of rotational symmetry lowering (see Figure 5.16) and allow to quantify the influence of electrostatic potentials (see Figure 5.18).

Detailed measurements on high-quality samples open the opportunity to refine some of the material parameters used for the $\boldsymbol{k} \cdot \boldsymbol{p}$ method, like BIA parameters, previously only estimated from theoretical calculations. Due to the considerable number of parameters and their combined influence onto parts of the bandstructure, such a refinement approach works best with a large set of data for various sample thicknesses over a large energetic range.

As discussed in the next section, such an investigation also turns out to be a bottleneck for accurate modeling of the valence bands.

5.3. Valence bands in the p-type charge regime

In the previous section 5.2 the importance of asymmetric models for surface and valence band states has been established. The insights and knowledge gained from there are now applied to

[23] Only the $N = -2$ landau level states remain strictly linear, as they are pure single-orbital eigenstates and therefore not affected by additional off-diagonal terms in the Hamiltonian. However, these states do not play a role for the discussion in this section, as they are buried deeper in the valence bands.

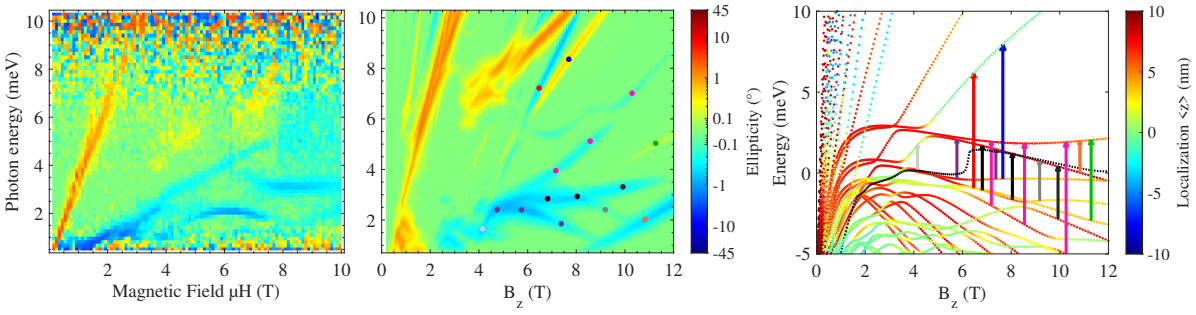

Fig. 5.20.: Spectra measured in a 30 nm HgTe layer gated to $p = 3.0 \times 10^{11}\mathrm{cm}^{-2}$ (left). Compared to calculated optical spectra at the same charge density (center), the energetic position does not match. The calculated eigenstates (right) show that these features with negative ellipticity emerge from transitions within the valence band states. Note that this shows one of many toy potentials and the number of LL states used was decreased to speed up calculations. Therefore, the results are inaccurate for magnetic fields below approximately 4 T. Data from [D7, C16].

the investigation of optical spectra where the ECP is moved down into the valence bands. A tetrahedral symmetry model involving valence band anisotropy and bulk inversion asymmetry (BIA) is the minimum model in this section.

Without considering structure inversion asymmetry (SIA), the model does not reproduce the many non-linear features with negative helicity, which must come from transitions inside the now partially filled valence bands, as described in Figure 5.20. While in the previous section, the influence of electrostatic potentials was notable, but still quite subtle, it now becomes clear that in the regime of densely spaced and strongly intermixed valence band states, it can not be ignored.

To further improve the $\boldsymbol{k} \cdot \boldsymbol{p}$ model, one needs to understand how electrostatic potentials affect the eigenstates of the Hamiltonian and which kind of potential model is required to provide realistic results.

The first subsection starts out by investigating the influence of toy-potentials on calculated optical spectra. It is followed up by a discussion about the benefits and challenges of a self-consistent potential method.

5.3.1. Toy potentials

The toy potential for Figure 5.20 was constructed in the same way as explained previously for Figure 5.19, but with changed parameters for the potential at the top surface and the penetration depth into the bulk. From a large range of different parameter values, the presented calculation is one of the better matches to the measured spectra. These results cannot be considered to be in good agreement with experimental data, but nevertheless offer some clues how to interpret the spectra.

Even though some of the features discussed in previous sections still show up in the theoretical spectra (especially the “smoking gun signatures” for BIA, indicated by red and blue markers), these cannot be identified clearly in experimental spectra. At those higher photon energies, the noise level is too high to resolve weaker features. The discussion here focuses on the features below 5 meV.

Compared to the charge neutral state in Figure 5.19, some of the valence band states are

pulled more towards the top interface by the larger top toy potential and gain about 1 meV higher energy eigenvalues. In contrast, the states localized more to the center of the bulk remain almost unchanged.

The increased energetic splitting between top and bulk/bottom states further separates the transitions marked by orange and green markers (compare to Figure 5.15). As the states also separate along the z axis, the strength of transitions between different localizations is reduced. The transition marked by the orange arrow is between states with a similar z expectation value, so the transition energy does not change much. It is plausible that this is the ascending transition which can be observed in the bottom right corner of the experimental spectra plot.

The transitions into the highest valence band states (magenta markers) also have a characteristic, nearly linear, ascending form. A similar feature can be seen for all experimental spectra in the measured p-type range (up to $p = 4 \times 10^{11}\mathrm{cm}^{-2}$), indicating that it is indeed a transition from deeper valence bands into the top-most one.

A downward-bent shape can also be found in both spectra plots (purple markers), even though the magnetic field positions differ[24]. The point of maximum photon energy for this transition mostly depends on the shape of the lower energy band. The change of slope here seems to be connected to increasing bulk localization and possibly interaction with near bulk localized states. Therefore, the behavior here should depend strongly on the exact form of the potential and the resulting localization and energetic splitting of bulk and near-interface valence band states.

For the transitions marked in black, it is harder to judge whether the initial lower energy states are connected to a band located close to the top interface or more inside the bulk, as the hybridization is strong here. From other calculations with higher potential values and less hybridization around this point, it looks like transitions are possible from both bulk and interface states, but the latter dominate the signal. As such, the almost constant transition energy of the transitions around 3 meV photon energy cannot be considered to be a characteristic signature of the SIA splitting, but rather seems to be connected to the energy difference between "bunched" bands. Furthermore, such an almost constant energy transition is not observed for most other values of the toy-potential.

As can be seen from the above discussion, toy potentials are not suited to describe the electrostatic potential distributions well enough to improve the overlap between calculated and observed spectra. The number of possible shapes and strengths of model distributions is also too large to guess or fit a "good" potential.

Nevertheless, the toy potentials can be used to analyze trends like the shifts in eigenenergy and localization of the valence band states. Figure 5.21 compares the same model with different signs for top and bottom interface potentials[25]. As the interpretation of the z expectation value alone can be misleading for the topological bandgap-crossing states, these are spared out from the discussion.

From both asymmetric potential sign configurations (top row), a similar conclusion can be derived as before: Positive potentials at an interface pull a subset of eigenstates (two out of the fourfold bunched bands) towards this interface, increasing their eigenenergies. This pull scales with the magnitude of the potential. The influence of the negative potential at the opposite interface is much weaker and the remaining subset of states is only slightly pushed towards

[24] With increasing toy-potential strength, this feature moves towards larger magnetic fields, more in line with the experimental observation.

[25] The notation here follows `kdotpy` in the sense, that potential means electron potential energy, which is the electric potential multiplied by the electron charge $-e$. Thus positive potential is linked to negative gate voltage (with respect to a grounded sample).

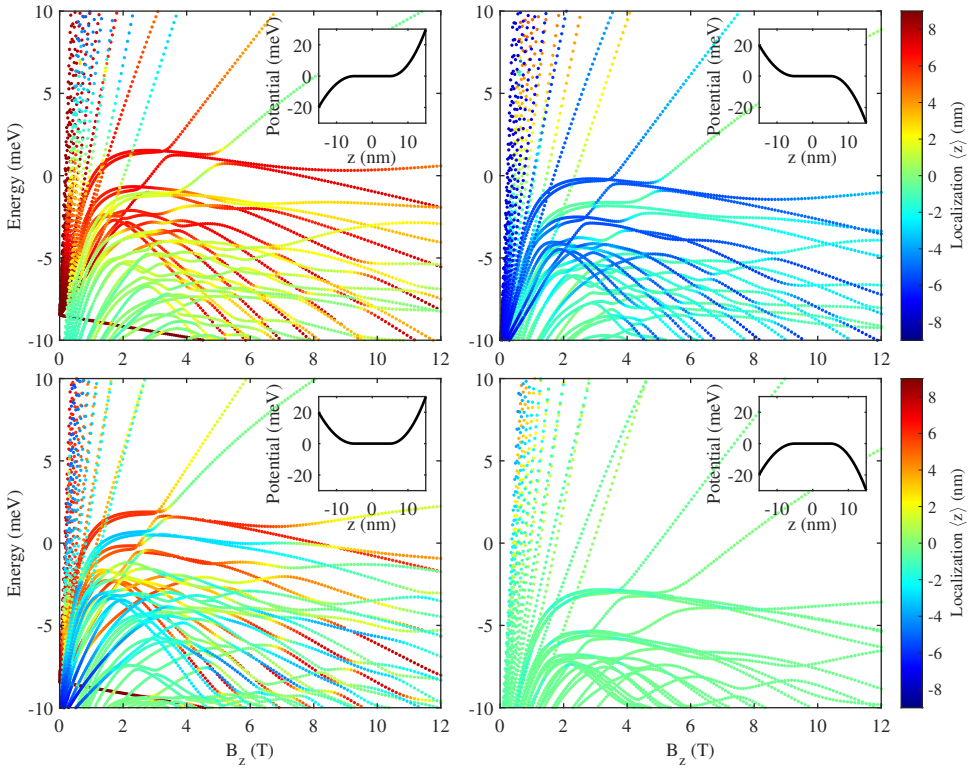

Fig. 5.21.: Comparison of valence band state localization in a 30 nm HgTe layer for different signs of top and bottom (electron) potentials (see inserts). Calculations analog to [C16].

the interface with the higher potential, with smaller changes in eigenenergies. Interestingly, the same subset of states moves towards either the top or bottom interface, depending on the external potential distribution. This is even the case for the bandgap crossing interface states - an observation in line with the degeneracy of those interface states in absence of external potentials (compare to Figure 5.3).

If the potential is positive at both interfaces, the two subsets are clearly split and drawn towards their respective interface. The shift in energy is different due to the unequal magnitudes for top and bottom potential. Interestingly, unlike before, most bands tend to have a weaker interface localization in higher magnetic fields. Presumably, this may be due to increased hybridization caused by the magnetic field.

In case of negative potentials at both interfaces, no splitting in the localization and energy of valence band states is observable. Instead of begin pulled out towards top or bottom interfaces, the valence band states are rather condensed a little into the center of the bulk[26]. Here the bands remain densely bunched together, contrary to the previous cases, where the energetic spacing between eigenstates is generally larger and more regular.

On first sight it may be counterintuitive that the states are pulled towards interfaces with higher (positive) potential. A simple intuitive explanation is based on the hole-like character of the valence band states. As holes have the opposite charge of electrons, the hole potential energy curve, which has the opposite sign of the electron potential energy plotted here, should be considered instead. Therefore, carriers move towards positions where their potential energy

[26]Note that the color tends slightly more towards the blue end of green, in line with the stronger top potential.

is minimized. A more rigorous mathematical derivation can be based on the reduction of the eight-orbital model down to, e.g., a four band model for the valence bands, using Löwdin partition [40, 98]. Analog to the derivation of the Rashba effect (reduction to conduction band states), the effect of electrostatic potential can be written in terms of the electric field, but the prefactor has opposite sign.

5.3.2. Summary and outlook towards self-consistent potentials

As previous sections have shown, there is a measurable influence of the gate voltage onto the energetic position of the eigenstates. It has further been successfully demonstrated, how toy potentials can be used to study the influence of electrical gating onto the bandstructure. While this is already useful for the analysis of trends in gate voltage studies, it is quite hard to find suitable parameters for a single electrostatic potential distribution that leads to better matches of the energetic positions of calculated transitions. Thus, a more sophisticated approach would be helpful for further and even more detailed analysis of the available spectra. The remainder of this last section presents possible ways to improve upon the status quo and highlights some of the challenges still ahead. The idea is to provide some useful thoughts, guidelines and caveats for follow-up projects.

Because the envelope-function approximation (EFA) does not just return the energy bandstructure, but also each eigenstate's spatially resolved wavefunction and occupation, a Hartree potential can be calculated from the $\boldsymbol{k}\cdot\boldsymbol{p}$ solution and the Poisson equation. This potential can then be fed back as input to the $\boldsymbol{k}\cdot\boldsymbol{p}$ calculation which then accounts for the potential of the charge distribution of the previous solution, returning a new, improved solution. Repeating this two-step procedure in a loop ideally lets the self-consistent model converge to the true solution.

A possible implementation of calculating the electrostatic potential from the $\boldsymbol{k}\cdot\boldsymbol{p}$ results is given in reference [45], which is conventionally used with the EFA approach [40, 99]. Here, calculated eigenstates must be attributed to either electronic conduction bands or hole valence bands and the effective charge sign and occupation factors are derived from this definition. The so calculated charge distributions are summed up and at the charge neutral point (CNP) at zero temperature this approach returns a uniform zero charge distribution throughout the sample, if there is a direct band gap or positive indirect band gap. Current versions of `kdotpy` still adopt this method for self-consistent potential calculations.

While this works for thin QW layers where the electron and hole character near the electrochemical potential (ECP) is mostly well definable, there are cases, like the thicker layers discussed in this thesis, in which such an attribution is not easily possible. A similar situation where band intermixing complicates the distinction between electrons and holes is discussed in reference [100]. With their "full-band envelope-function approach" (FB-EFA) the authors circumvent the concept of holes in the bandstructure altogether and stay in the "natural" picture of a bandstructure filled with electrons up to the ECP against a flat positive charge background given by the compensating atom core charges. Note that this approach is computationally more challenging, as in principle all subbands given by the Hamiltonian dimension must be calculated. The method gives rise to interface charges which effectively change the value of the valence band offset of the layer materials. As the $\boldsymbol{k}\cdot\boldsymbol{p}$ parameter for the valence band offset also contains such effects implicitly, this parameter must be renormalized.

Such an approach has been used in reference [36] to calculate the electrostatic potential in absence of magnetic fields for three charge densities. At the CNP the potential distribution calculated there indeed deviates from what is expected for a uniform zero charge distribution.

When incorporating magnetic fields into the calculation, further challenges arise. As discussed earlier, including magnetic fields along the growth axis into the $\boldsymbol{k} \cdot \boldsymbol{p}$ calculation would require to discretize one of the layers' in-plane coordinate which drastically increases the computational effort to an infeasible level. Thus, `kdotpy` uses a Landau level (LL) basis instead of $\boldsymbol{k}$-space whenever magnetic field dependence is of interest. With the currently implemented charge determination method `kdotpy` can reliably calculate a distribution of charge as difference to the state at the CNP[27] for each magnetic field[28]. However, the actual charge distributions for the CNP states are generally not known.

Using the CNP state charge distribution determined without the presence of a magnetic field for calculations including magnetic fields may not be a valid approach in many situations, as results presented in previous sections clearly show, that eigenstates are affected by the magnetic field and change their localization along the growth direction z. As a consequence, the CNP states for different magnetic fields are not identical and the actual electrostatic potential cannot be calculated by the charge differences output by `kdotpy`. A method similar to the FB-EFA [100] described above must be developed in the LL state space, where all states below the ECP are taken into account in front of a suitable positive atomic core background.

As the LL state space generally extends to infinite LLs, whereas $\boldsymbol{k}$-space is bounded by the discretization lattice spacing, and a suitable cut-off needs to be used for actual calculations, it remains to be tested[29] whether such an approach is feasible at all and returns valid results.

Aside the question of how the charge distribution in the sample is calculated correctly, there are further points to be considered when it comes to solving the Poisson equation. This can be done by integration over the charge density twice and introduces two boundary conditions (BCs). One possible choice[30] of BCs would be the values of the electric field and the potential, each at one arbitrary position. The BC for the potential can be chosen arbitrarily, as it only shifts the whole potential distribution and the bandstructure along the energy axis without measurable effects. The boundary condition for the electric field on the other hand, has an important influence on the solution. As the $\boldsymbol{k} \cdot \boldsymbol{p}$ solution without a SIA-introducing potential is totally symmetric with respect to the mercury telluride layer's center plane, setting the electric field to zero at this point results in a potential distribution which is also totally symmetric. Therefore, this special boundary condition does not break inversion asymmetry for any amount of charge in the layer.

As samples are typically gated asymmetrically from the top side, such a BC seems unrealistic. However, at the bottom end of the layer stack, where the sample is grown on a thick, charge-neutral substrate, no electric field is expected[31] at this position. Unless specifically doped, the barrier layers of the QW can also be assumed to be free of charge. Fixing the electric field to zero at the bottom end of the lower barrier layer is thus a good approximation for samples investigated in this work.

[27] This is because one can, again, not assign an electron or hole label to a calculated LL eigenstate. However, by the "band alignment" process of `kdotpy` one can keep track of the CNP, i.e. the point up to which eigenstates must be filled to such that the sample remains in a charge neutral state. Filling a state more above this point in energy adds electron charge into the system, emptying a state below the CNP removes electrons or effectively adds positive charge. Using this mechanism, the ECP can also be defined correctly for a given charge density.

[28] Note that smaller magnetic fields require a larger number of LLs for a realistic description.

[29] W. Beugeling and C. Berger have taken over this larger project from the author at the point of writing this thesis.

[30] In `kdotpy` other BCs can be defined, e.g. potentials at two positions. Under such circumstances, the total charge in the layer is not adjustable by the user, but defined by the BCs and calculated automatically.

[31] Further interface effects could be modeled with the electric field at this position as a variable parameter.

In the Poisson equation the static dielectric constant, more specifically the component along the z-axis of the dielectric tensor at zero frequency, $\epsilon_z(0)$, is required. But it is unclear, which value to use for the dielectric constant in mercury telluride layers [30, 54]. Considering HgTe bulk crystals are conductive semi-metals, it seems unfeasible that a finite value for a static dielectric constant may actually be defined. The often used literature value coming from reference [54] appears completely unmotivated in a summary table, without any definition of its actual meaning. Most likely, it is rather a value with summarizes the low-frequency response (with respect to the used frequency spectrum) of the investigated transitions and the ϵ_∞ contribution of higher frequency transitions, instead of a true static component at zero frequency. The fact, that reflectivity spectra presented in the reference approach 100 % in the limit of low frequencies is an indicator that there are much more low-energy transitions present, which are not included in the model of reference [54] but change the actual value of $\epsilon(\omega \to 0)$.

The Kubo-Greenwood formula approach (see section 2.2.5) allows to calculate the dielectric response functions based on possible transitions between states in the bandstructure, even within a self-consistent approach[32]. The relevant transitions for $\epsilon_z(\omega)$ are between adjacent subband states or equal subbands with opposite parity [49]. In very thick layers (or bulk crystals) the confinement energy splitting between subbands is close to zero and there is an extremely large number of possible subband transitions with low energy. This lets the value of the dielectric response function diverge in the static limit $\omega \to 0$.

In the limit of thin layers (as in the QW case), the confinement energy separates the subbands further apart, which reduces the amount and strength of low-energy transitions and allows for finite values of a dielectric constant. Generally, the correct value to use in the Poisson equation should depend on the thickness of the mercury telluride layer, the charge density inside the layer and the magnetic field. Possibly the value is also not constant along the growth direction, due to different localization of the eigenstates.

Even when putting aside the challenges described above and using `kdotpy`'s self-consistent algorithm as is, with a reasonable range of values for dielectric constants, one can run into numerical instabilities. Instead of converging to a single solution, the potential often jumps between different meta-stable configurations. Such a behavior is inherent to the self-consistent approach in a situation where the ECP resides between two states with notably different localization that tend to flip positions around the ECP for different electrostatic potentials, e.g., due to a close-by crossing point. As an example, in one iteration of the self-consistent loop, the state above the ECP is localized at the top interface, while the one below is closer towards the bottom interface. Evaluating the charge distribution of occupied states below the ECP, which has more charge at the bottom interface, may result in a potential that moves the bottom state above the ECP, while the top state consequently moves below the ECP. Now the charge distribution is changed to a situation where more charge is at the top interface, resulting in a different electrostatic potential, which may exchange the energetic positions of the top and bottom states again.

Such meta-stable stable flip-flop conditions can occur at many points in magnetic field dependence of LL eigenstates, when the ECP runs through a crossing point of eigenstates. Including more asymmetry in the model (e.g. BIA) helps to reduce such issues, as crossing points of eigenstates are turned into avoided crossings, where the states hybridize and localizations become similar. Of course, this comes at the cost of increased computation time for the more

[32] Note that the range of transitions that can be calculated realistically is limited and higher energy transitions would need to be modeled otherwise

complex models with higher asymmetry. Furthermore, not all crossing points can be lifted by introducing the asymmetries discussed in this thesis (compare to Figure 5.21).

Future projects may tackle the challenges laid out above by optimization of the `kdotpy` code and the use of high performance computation clusters as University of Würzburg's *Julia* cluster. Once some realistic calculations have been successful, the experience gained from those solutions may be used to derive good approximations for the faster toy-potential models and further improve the accuracy of the computed bandstructure.

6 Outlook and Conclusion

Over the course of this project, a setup for time-domain THz polarimetry has been developed, built and characterized successfully. The high degree of automatization enables long-term measurement campaigns with minimal user interaction at polarization noise levels down to 10^{-2} to 10^{-1} degrees. Samples can be investigated at temperatures from 1.4 to 300 K and in magnetic fields between ± 10 T. Specially developed large-area gate structures on the mecury cadmium telluride (MCT) samples in combination with a standardized chip-carrier system enable monitoring and adjustment of the charge carrier density in the samples alongside the THz measurements.

This combination of optical and electrical techniques, as well as the high measurement precision and sample quality are absolute novelties in the field of MCT material systems. The setup developed for this thesis will be able to provide high-quality data not only for the continuation of this project, but potentially also other small-bandgap (topological) insulator material systems.

Using this approach, single and weak optical transitions have been detected for the first time. Together with thorough analysis, backed by theoretical modelling, some spectral features could be traced back to unique combination of initial and final transition eigenstates. Further investigation allowed to determine the importance of asymmetry terms in the model Hamiltonian and an estimate for the strength of those asymmetry parameters. Additionally, new light could be shed onto the evolution of topological interface states towards a two-dimensional quantum Hall limit with increasing magnetic field.

As discussed extensively in the previous chapter, the $\boldsymbol{k} \cdot \boldsymbol{p}$ method, when used correctly, is a powerful tool to precisely calculate the band structure close to the Fermi level. Other than reduced effective models, it does not just fit to measured data, but is capable of predicting features in the measurement based on known basic properties of the model, like layer thickness, composition and charge density. The biggest advantages compared to simplified models often used in literature is the intrinsic inclusion of boundary states and external magnetic fields.

While none of the single methods and calculation strategies used throughout this thesis are truly new on their own, the combination of all of these together to form an experimental and theoretical tool set for highly precise band structure investigations is unprecedented.

To the author's knowledge, the bundling of former independent LL states upon consideration of valence band asymmetry in the $\boldsymbol{k} \cdot \boldsymbol{p}$ model has not been discussed in literature before, but becomes important when working with those valence band states. The experimental results obtained also show proof for the presence of bulk inversion asymmetry (BIA) effects in the measured spectra and contribute to answering the question whether and when BIA terms are required in the Hamiltonian describing (thick) CdTe/HgTe quantum wells.

Considering everything that has been learned from the samples and models discussed here, in which directions could further projects be driven?

Most straightforward would be the investigation of thicker mercury telluride layers. At the time these experiments were conducted, only newer thinner layers showed a new record in sample quality[1]. By now, first measurements have also been conducted on samples with 70 nm mecury telluride layer thickness. These show similarly clear and sharp features as the 30 and 45 nm samples discussed here. Comparing to Figure 5.2, no qualitatively different trends are expected from thicker layers. However, since the confinement energy is reduced

[1] Determined from carrier densities and mobilities measured in transport experiments.

for thicker layers, bands move closer together, which alone moves more optical transitions into the observable energy window of the Terahertz setup. Furthermore, the smaller energy difference between bands increases intermixing of states. While this makes the comparison of a growth series with increasing thickness a good possibility to look out for new trends and better calibration of material parameters, the details of the band structure become more and more challenging to analyze in thicker layers. Not only is the state intermixing stronger, which is already quite challenging in the valence bands, but also interface states tend to localize stronger at the boundaries. From previous experience, such strongly localized states make the calculations of self-consistent potentials even more unstable, as changes in their occupation have a strong influence on the resulting potential.

Another logical next step is the extension of the photon energies using FTIR spectroscopy. It helps to follow transitions of interest that run out of the energy windows accessible for the THz setup. Challenges are introduced from the many possible optical transitions at higher photon energies, where many subbands and LL states contribute with overlapping transition energies. The attribution of spectral features to a single transition becomes more and more difficult. Furthermore, all of these higher order bands need to be calculated in the $\boldsymbol{k} \cdot \boldsymbol{p}$ model as well, which can become a numerical challenge on its own.

A closer collaboration with teams running transport experiments can help to extract even more information. In optical experiments, the energy resolution is usually dominated by broadening effects, which are either intrinsic to the source and method itself, the lifetime of excited states or in some scenarios even due to temperature broadening. On the other hand, transport measurements like a Landau level (LL) fan chart map do not offer direct access to an energy scale, but can again be compared to $\boldsymbol{k} \cdot \boldsymbol{p}$ calculations. These experiments can be run at millikelvin temperatures, which drastically reduces broadening effects and enable to determine the intrinsic broadening of LL states themselves. As already mentioned shortly in section 2.1.7, small in-plane magnetic fields offer a way to tune between some LL crossings and avoided crossings. Such effects are covered by broadening in an optical measurement, but can be resolved in transport experiments. Optical measurements and the $\boldsymbol{k} \cdot \boldsymbol{p}$ method on the other hand are helpful when narrowing down the parameter range where to look for such special crossings.

As different material compositions and strain conditions are easily adjustable in the $\boldsymbol{k} \cdot \boldsymbol{p}$ model, the tool set developed here can accompany the drive of the mercury cadmium telluride material platform towards other (topological) phases or material classes. First work has already been conducted on Weyl-type samples, where compressive instead of tensile strain drives the valence and conduction bands of mercury telluride layers through each other instead of apart [101, 102]. In theory, this leads again to Dirac-like linear states at multiple points in the Brillouin zone, which are connected to each other via Fermi arcs. Such a system would allow to investigate quasi-particles which have not been found in nature so far.

It is also possible to add and change the cadmium concentration in the mercury telluride layer of interest. In tensile strained layers this is known to shift the energetic position of the interface states' Dirac point. It can also move linear dispersive states into the former bulk band gap. However, these states do not exhibit an interface character anymore and form in fact gapless bulk states. These materials are classified as Kane metals and are probably the most promising mercury cadmium telluride material system that offer linear dispersive states at the Fermi level [31].

The methods described here help to verify whether the real band structure of the sample is indeed the same as one required for the observation of the new quasi-particle effects.

A List of acronyms

ALD	atomic layer deposition
ARPES	angle-resolved photoemission spectroscopy
BC	boundary condition
BHZ	Bernevig, Hughes and Zhang
BIA	bulk inversion asymmetry
CNP	charge neutral point
CR	cyclotron resonance
CW	continuous wave
DFT	density functional theory
ECP	electro-chemical potential
EFA	envelope-function approximation
EM	electromagnetic
FTIR	Fourier transform infrared
HDPE	high-density polyethylene
HfO_2	hafnium dioxide
FT	Fourier transformation
FWHM	full width at half maximum
LL	Landau level
MBE	molecular beam epitaxy
MCT	mecury cadmium telluride
SIA	structure inversion asymmetry
SNR	signal to noise ratio
TD	time-domain
TDS	time-domain spectroscopy
THz	Terahertz
TI	Topological Insulator
QHE	quantum Hall effect
QW	quantum well
VdP	Van-der-Pauw
VP	Volkov-Pankratov
VTI	variable temperature insert

B Bibliography

Further publications under participation of the author

[A1] Christian Berger et al. "Diminishing topological Faraday effect in thin layer samples". In: *Phys. Rev. Res.* 6 (1 Jan. 2024), p. 013068. DOI: 10.1103/PhysRevResearch.6.013068. URL: https://link.aps.org/doi/10.1103/PhysRevResearch.6.013068.

[A2] Tatiana A. Uaman Svetikova et al. "Giant THz Nonlinearity in Topological and Trivial HgTe-Based Heterostructures". In: *ACS Photonics* 10.10 (2023), pp. 3708–3714. DOI: 10.1021/acsphotonics.3c00867. URL: https://doi.org/10.1021/acsphotonics.3c00867.

[A3] F. Münzhuber et al. "Polarization-Assisted Vector Magnetometry with No Bias Field Using an Ensemble of Nitrogen-Vacancy Centers in Diamond". In: *Phys. Rev. Applied* 14 (1 July 2020), p. 014055. DOI: 10.1103/PhysRevApplied.14.014055. URL: https://link.aps.org/doi/10.1103/PhysRevApplied.14.014055.

[A4] Stefan Imhof et al. "Topolectrical-circuit realization of topological corner modes". In: *Nature Physics* 14.9 (Sept. 2018), pp. 925–929. DOI: 10.1038/s41567-018-0246-1. URL: https://doi.org/10.1038/s41567-018-0246-1.

[A5] Ching Hua Lee et al. "Topolectrical Circuits". In: *Communications Physics* 1.1 (July 2018). DOI: 10.1038/s42005-018-0035-2. URL: https://doi.org/10.1038/42005-018-0035-2.

A continuously updated publication list can be found at the author's ORCID entry https://orcid.org/0000-0002-4428-7301.

Cited literature

[1] Prineha Narang, Christina AC Garcia, and Claudia Felser. "The topology of electronic band structures". In: *Nature Materials* 20.3 (2021), pp. 293–300. DOI: https://doi.org/10.1038/s41563-020-00820-4.

[2] Xiao-Liang Qi and Shou-Cheng Zhang. "Topological insulators and superconductors". In: *Rev. Mod. Phys.* 83 (4 Oct. 2011), pp. 1057–1110. DOI: 10.1103/RevModPhys.83.1057. URL: https://link.aps.org/doi/10.1103/RevModPhys.83.1057.

[3] C. L. Kane and E. J. Mele. "Z_2 Topological Order and the Quantum Spin Hall Effect". In: *Phys. Rev. Lett.* 95 (14 Sept. 2005), p. 146802. DOI: 10.1103/PhysRevLett.95.146802. URL: https://link.aps.org/doi/10.1103/PhysRevLett.95.146802.

[4] J. E. Moore and L. Balents. "Topological invariants of time-reversal-invariant band structures". In: *Phys. Rev. B* 75 (12 Mar. 2007), p. 121306. DOI: 10.1103/PhysRevB.75.121306. URL: https://link.aps.org/doi/10.1103/PhysRevB.75.121306.

[5] BA Volkov and OA Pankratov. "Two-dimensional massless electrons in an inverted contact". In: *Soviet Journal of Experimental and Theoretical Physics Letters* 42 (1985), p. 178. URL: http://jetpletters.ru/ps/1420/article_21570.shtml.

[6] O.A. Pankratov, S.V. Pakhomov, and B.A. Volkov. "Supersymmetry in heterojunctions: Band-inverting contact on the basis of $Pb_{1-x}Sn_xTe$ and $Hg_{1-x}Cd_xTe$". In: *Solid State Communications* 61.2 (1987), pp. 93–96. ISSN: 0038-1098. DOI: https://doi.org/10.1016/0038-1098(87)90934-3. URL: https://www.sciencedirect.com/science/article/pii/0038109887909343.

[7] D. J. Thouless et al. "Quantized Hall Conductance in a Two-Dimensional Periodic Potential". In: *Phys. Rev. Lett.* 49 (6 Aug. 1982), pp. 405–408. DOI: 10.1103/PhysRevLett.49.405. URL: https://link.aps.org/doi/10.1103/PhysRevLett.49.405.

[8] J. E. Avron, R. Seiler, and B. Simon. "Homotopy and Quantization in Condensed Matter Physics". In: *Phys. Rev. Lett.* 51 (1 July 1983), pp. 51–53. DOI: 10.1103/PhysRevLett.51.51. URL: https://link.aps.org/doi/10.1103/PhysRevLett.51.51.

[9] Liang Fu, C. L. Kane, and E. J. Mele. "Topological Insulators in Three Dimensions". In: *Phys. Rev. Lett.* 98 (10 Mar. 2007), p. 106803. DOI: 10.1103/PhysRevLett.98.106803. URL: https://link.aps.org/doi/10.1103/PhysRevLett.98.106803.

[10] Liang Fu and C. L. Kane. "Topological insulators with inversion symmetry". In: *Phys. Rev. B* 76 (4 July 2007), p. 045302. DOI: 10.1103/PhysRevB.76.045302. URL: https://link.aps.org/doi/10.1103/PhysRevB.76.045302.

[11] Xiao-Liang Qi, Taylor L. Hughes, and Shou-Cheng Zhang. "Topological field theory of time-reversal invariant insulators". In: *Phys. Rev. B* 78 (19 Nov. 2008), p. 195424. DOI: 10.1103/PhysRevB.78.195424. URL: https://link.aps.org/doi/10.1103/PhysRevB.78.195424.

[12] B. Andrei Bernevig, Taylor L. Hughes, and Shou-Cheng Zhang. "Quantum Spin Hall Effect and Topological Phase Transition in HgTe Quantum Wells". In: *Science* 314.5806 (2006), pp. 1757–1761. DOI: 10.1126/science.1133734. eprint: https://www.science.org/doi/pdf/10.1126/science.1133734. URL: https://www.science.org/doi/abs/10.1126/science.1133734.

[13] Markus König et al. "Quantum Spin Hall Insulator State in HgTe Quantum Wells". In: *Science* 318.5851 (2007), pp. 766–770. DOI: 10.1126/science.1148047. eprint: https://www.science.org/doi/pdf/10.1126/science.1148047. URL: https://www.science.org/doi/abs/10.1126/science.1148047.

[14] Markus König et al. "The Quantum Spin Hall Effect: Theory and Experiment". In: *Journal of the Physical Society of Japan* 77.3 (2008), p. 031007. DOI: 10.1143/JPSJ.77.031007. eprint: https://doi.org/10.1143/JPSJ.77.031007. URL: https://doi.org/10.1143/JPSJ.77.031007.

[15] David Hsieh et al. "A topological Dirac insulator in a quantum spin Hall phase". In: *Nature* 452.7190 (2008), pp. 970–974. DOI: https://doi.org/10.1038/nature06843.

[16] Yuqi Xia et al. "Observation of a large-gap topological-insulator class with a single Dirac cone on the surface". In: *Nature physics* 5.6 (2009), pp. 398–402. DOI: https://doi.org/10.1038/nphys1274.

[17] Haijun Zhang et al. "Topological insulators in Bi2Se3, Bi2Te3 and Sb2Te3 with a single Dirac cone on the surface". In: *Nature physics* 5.6 (2009), pp. 438–442. DOI: https://doi.org/10.1038/nphys1270.

[18] Pedram Roushan et al. “Topological surface states protected from backscattering by chiral spin texture”. In: *Nature* 460.7259 (2009), pp. 1106–1109. DOI: https://doi.org/10.1038/nature08308.

[19] Liang Wu et al. “Quantized Faraday and Kerr rotation and axion electrodynamics of a 3D topological insulator”. In: *Science* 354.6316 (2016), pp. 1124–1127. DOI: 10.1126/science.aaf5541. eprint: https://www.science.org/doi/pdf/10.1126/science.aaf5541. URL: https://www.science.org/doi/abs/10.1126/science.aaf5541.

[20] V Dziom et al. “Observation of the universal magnetoelectric effect in a 3D topological insulator”. In: *Nature communications* 8.1 (2017), pp. 1–8.

[21] Liang Fu and C. L. Kane. “Superconducting Proximity Effect and Majorana Fermions at the Surface of a Topological Insulator”. In: *Phys. Rev. Lett.* 100 (9 Mar. 2008), p. 096407. DOI: 10.1103/PhysRevLett.100.096407. URL: https://link.aps.org/doi/10.1103/PhysRevLett.100.096407.

[22] Ville Lahtinen and Jiannis K. Pachos. “A Short Introduction to Topological Quantum Computation”. In: *SciPost Phys.* 3 (3 2017), p. 021. DOI: 10.21468/SciPostPhys.3.3.021. URL: https://scipost.org/10.21468/SciPostPhys.3.3.021.

[23] C. L. Kane and E. J. Mele. “Quantum Spin Hall Effect in Graphene”. In: *Phys. Rev. Lett.* 95 (22 Nov. 2005), p. 226801. DOI: 10.1103/PhysRevLett.95.226801. URL: https://link.aps.org/doi/10.1103/PhysRevLett.95.226801.

[24] A. H. Castro Neto et al. “The electronic properties of graphene”. In: *Rev. Mod. Phys.* 81 (1 Jan. 2009), pp. 109–162. DOI: 10.1103/RevModPhys.81.109. URL: https://link.aps.org/doi/10.1103/RevModPhys.81.109.

[25] Aaron Bostwick et al. “Quasiparticle dynamics in graphene”. In: *Nature physics* 3.1 (2007), pp. 36–40. DOI: https://doi.org/10.1038/nphys477.

[26] Yuanbo Zhang et al. “Experimental observation of the quantum Hall effect and Berry’s phase in graphene”. In: *Nature* 438.7065 (2005), pp. 201–204. DOI: 10.1038/nature04235.

[27] C. Brüne et al. “Quantum Hall Effect from the Topological Surface States of Strained Bulk HgTe”. In: *Phys. Rev. Lett.* 106 (12 Mar. 2011), p. 126803. DOI: 10.1103/PhysRevLett.106.126803. URL: https://link.aps.org/doi/10.1103/PhysRevLett.106.126803.

[28] Jason N. Hancock et al. “Surface State Charge Dynamics of a High-Mobility Three-Dimensional Topological Insulator”. In: *Phys. Rev. Lett.* 107 (13 Sept. 2011), p. 136803. DOI: 10.1103/PhysRevLett.107.136803. URL: https://link.aps.org/doi/10.1103/PhysRevLett.107.136803.

[29] A. M. Shuvaev et al. “Terahertz quantum Hall effect of Dirac fermions in a topological insulator”. In: *Phys. Rev. B* 87 (12 Mar. 2013), p. 121104. DOI: 10.1103/PhysRevB.87.121104. URL: https://link.aps.org/doi/10.1103/PhysRevB.87.121104.

[30] Christoph Brüne et al. “Dirac-Screening Stabilized Surface-State Transport in a Topological Insulator”. In: *Phys. Rev. X* 4 (4 Dec. 2014), p. 041045. DOI: 10.1103/PhysRevX.4.041045. URL: https://link.aps.org/doi/10.1103/PhysRevX.4.041045.

[31] Raimund Schlereth. "New techniques and improvements in the MBE growth of Hg-containing narrow gap semiconductors". doctoral thesis. Universität Würzburg, 2020. DOI: 10.25972/OPUS-20079. URL: https://nbn-resolving.org/urn:nbn:de:bvb:20-opus-200790.

[32] A. Pfeuffer-Jeschke. "Ph.D. thesis". PhD thesis. Physikalisches Institut, Julius-Maximilians-Universität Würzburg, 2000.

[33] M. von Truchsess et al. "Spectroscopy of interface states in HgTe/$Hg_{1-x}Cd_xTe$ superlattices". In: *Journal of Crystal Growth* 184-185 (1998), pp. 1190–1194. ISSN: 0022-0248. DOI: https://doi.org/10.1016/S0022-0248(98)80249-2. URL: https://www.sciencedirect.com/science/article/pii/S0022024898802492.

[34] A. Shuvaev et al. "Room temperature electrically tunable terahertz Faraday effect". In: *Applied Physics Letters* 102.24 (2013), p. 241902. DOI: 10.1063/1.4811496. eprint: https://doi.org/10.1063/1.4811496. URL: https://doi.org/10.1063/1.4811496.

[35] Christopher Ames. "Molecular Beam Epitaxy of 2D and 3D HgTe, a Topological Insulator". doctoral thesis. Universität Würzburg, 2015. URL: https://nbn-resolving.org/urn:nbn:de:bvb:20-opus-151136.

[36] J. Gospodarič et al. "Band structure of a HgTe-based three-dimensional topological insulator". In: *Phys. Rev. B* 102 (11 Sept. 2020), p. 115113. DOI: 10.1103/PhysRevB.102.115113. URL: https://link.aps.org/doi/10.1103/PhysRevB.102.115113.

[37] Wouter Beugeling et al. *kdotpy*. Version 0.71 – 0.78. Python script collection. Würzburg, Germany: Universität Würzburg, Physikalisches Institut, EP3, 2021. URL: https://git.physik.uni-wuerzburg.de/kdotpy/kdotpy.

[38] Simon Moser. "An experimentalist's guide to the matrix element in angle resolved photoemission". In: *Journal of Electron Spectroscopy and Related Phenomena* 214 (2017), pp. 29–52. ISSN: 0368-2048. DOI: https://doi.org/10.1016/j.elspec.2016.11.007. URL: https://www.sciencedirect.com/science/article/pii/S0368204816301724.

[39] P. Yu and M. Cardona. *Fundamentals of Semiconductors*. 2nd ed. Berlin Heidelberg: Springer-Verlag, 1999. ISBN: 3-540-65352-X. DOI: https://doi.org/10.1007/978-3-642-00710-1.

[40] R. Winkler. *Spin–Orbit Coupling Effects in Two-Dimensional Electron and Hole Systems*. 1st ed. Berlin Heidelberg: Springer-Verlag, 2003. ISBN: 3-540-01187-0. DOI: https://doi.org/10.1007/b13586.

[41] J. M. Luttinger and W. Kohn. "Motion of Electrons and Holes in Perturbed Periodic Fields". In: *Phys. Rev.* 97 (4 Feb. 1955), pp. 869–883. DOI: 10.1103/PhysRev.97.869. URL: https://link.aps.org/doi/10.1103/PhysRev.97.869.

[42] Ahmet Elçi and Eric D. Jones. "Some consequences of the closure of the momentum Bloch functions". In: *Phys. Rev. B* 34 (12 Dec. 1986), pp. 8611–8615. DOI: 10.1103/PhysRevB.34.8611. URL: https://link.aps.org/doi/10.1103/PhysRevB.34.8611.

[43] E.O. Kane. "Chapter 3 The k · p Method". In: *Semiconductors and Semimetals*. Ed. by R.K. Willardson and Albert C. Beer. Vol. 1. Semiconductors and Semimetals. Elsevier, 1966, pp. 75–100. DOI: https://doi.org/10.1016/S0080-8784(08)62376-5. URL: https://www.sciencedirect.com/science/article/pii/S0080878408623765.

[44] Evan O. Kane. “Band structure of indium antimonide”. In: *Journal of Physics and Chemistry of Solids* 1.4 (1957), pp. 249–261. ISSN: 0022-3697. DOI: https://doi.org/10.1016/0022-3697(57)90013-6. URL: https://www.sciencedirect.com/science/article/pii/0022369757900136.

[45] E. G. Novik et al. “Band structure of semimagnetic $Hg_{1-y}Mn_yTe$ quantum wells”. In: *Phys. Rev. B* 72 (3 July 2005), p. 035321. DOI: 10.1103/PhysRevB.72.035321. URL: https://link.aps.org/doi/10.1103/PhysRevB.72.035321.

[46] L. J. Sham and M. Nakayama. “Effective-mass approximation in the presence of an interface”. In: *Phys. Rev. B* 20 (2 July 1979), pp. 734–747. DOI: 10.1103/PhysRevB.20.734. URL: https://link.aps.org/doi/10.1103/PhysRevB.20.734.

[47] G. Bastard. “Superlattice band structure in the envelope-function approximation”. In: *Phys. Rev. B* 24 (10 Nov. 1981), pp. 5693–5697. DOI: 10.1103/PhysRevB.24.5693. URL: https://link.aps.org/doi/10.1103/PhysRevB.24.5693.

[48] G.E. Marques and L.J. Sham. “Theory of space-charge layers in narrow-gap semiconductors”. In: *Surface Science* 113.1 (1982), pp. 131–136. ISSN: 0039-6028. DOI: https://doi.org/10.1016/0039-6028(82)90573-8. URL: https://www.sciencedirect.com/science/article/pii/0039602882905738.

[49] H. Luo and J. K. Furdyna. “Optical transitions in semiconductor superlattices with zinc-blende structure in the k·p approximation”. In: *Phys. Rev. B* 41 (8 Mar. 1990), pp. 5188–5196. DOI: 10.1103/PhysRevB.41.5188. URL: https://link.aps.org/doi/10.1103/PhysRevB.41.5188.

[50] M G Burt. “The justification for applying the effective-mass approximation to microstructures”. In: *Journal of Physics: Condensed Matter* 4.32 (Aug. 1992), pp. 6651–6690. DOI: 10.1088/0953-8984/4/32/003. URL: https://doi.org/10.1088/0953-8984/4/32/003.

[51] M G Burt. “Fundamentals of envelope function theory for electronic states and photonic modes in nanostructures”. In: *Journal of Physics: Condensed Matter* 11.9 (Jan. 1999), pp. 53–83. DOI: 10.1088/0953-8984/11/9/002. URL: https://doi.org/10.1088/0953-8984/11/9/002.

[52] R. Winkler and U. Rössler. “General approach to the envelope-function approximation based on a quadrature method”. In: *Phys. Rev. B* 48 (12 Sept. 1993), pp. 8918–8927. DOI: 10.1103/PhysRevB.48.8918. URL: https://link.aps.org/doi/10.1103/PhysRevB.48.8918.

[53] K. Suzuki and J. C. Hensel. “Quantum resonances in the valence bands of germanium. I. Theoretical considerations”. In: *Phys. Rev. B* 9 (10 May 1974), pp. 4184–4218. DOI: 10.1103/PhysRevB.9.4184. URL: https://link.aps.org/doi/10.1103/PhysRevB.9.4184.

[54] J. Baars and F. Sorger. “Reststrahlen spectra of HgTe and CdxHg1-xTe”. In: *Solid State Communications* 10.9 (1972), pp. 875–878. ISSN: 0038-1098. DOI: https://doi.org/10.1016/0038-1098(72)90211-6. URL: https://www.sciencedirect.com/science/article/pii/0038109872902116.

[55] E Bangert et al. “The optical absorption coefficient of HgTe-CdTe superlattices-theory and experiment”. In: *Semiconductor Science and Technology* 8.1S (Jan. 1993), pp. 99–101. DOI: 10.1088/0268-1242/8/1s/022. URL: https://doi.org/10.1088/0268-1242/8/1s/022.

[56] Ryogo Kubo. “Statistical-Mechanical Theory of Irreversible Processes. I. General Theory and Simple Applications to Magnetic and Conduction Problems”. In: *Journal of the Physical Society of Japan* 12.6 (1957), pp. 570–586. DOI: 10.1143/JPSJ.12.570. eprint: https://doi.org/10.1143/JPSJ.12.570. URL: https://doi.org/10.1143/JPSJ.12.570.

[57] Ryogo Kubo, Mario Yokota, and Sadao Nakajima. “Statistical-Mechanical Theory of Irreversible Processes. II. Response to Thermal Disturbance”. In: *Journal of the Physical Society of Japan* 12.11 (1957), pp. 1203–1211. DOI: 10.1143/JPSJ.12.1203. eprint: https://doi.org/10.1143/JPSJ.12.1203. URL: https://doi.org/10.1143/JPSJ.12.1203.

[58] “Phenomenological Theory”. In: *Condensed Matter Physics*. John Wiley & Sons, Ltd, 2010. Chap. 20, pp. 611–631. ISBN: 9780470949955. DOI: https://doi.org/10.1002/9780470949955.ch20. eprint: https://onlinelibrary.wiley.com/doi/pdf/10.1002/9780470949955.ch20. URL: https://onlinelibrary.wiley.com/doi/abs/10.1002/9780470949955.ch20.

[59] I. M. Boswarva et al. “Faraday effect in semiconductors”. In: *Proceedings of the Royal Society of London. Series A. Mathematical and Physical Sciences* 269.1336 (1962), pp. 125–141. DOI: 10.1098/rspa.1962.0166. eprint: https://royalsocietypublishing.org/doi/pdf/10.1098/rspa.1962.0166. URL: https://royalsocietypublishing.org/doi/abs/10.1098/rspa.1962.0166.

[60] I. M. Boswarva, A. B. Lidiard, and Robert William Ditchburn. “Faraday effect in semiconductors. II”. In: *Proceedings of the Royal Society of London. Series A. Mathematical and Physical Sciences* 278.1375 (1964), pp. 588–609. DOI: 10.1098/rspa.1964.0084. eprint: https://royalsocietypublishing.org/doi/pdf/10.1098/rspa.1964.0084. URL: https://royalsocietypublishing.org/doi/abs/10.1098/rspa.1964.0084.

[61] L. Duvillaret, F. Garet, and J.-L. Coutaz. “A reliable method for extraction of material parameters in terahertz time-domain spectroscopy”. In: *IEEE Journal of Selected Topics in Quantum Electronics* 2.3 (Sept. 1996), pp. 739–746. ISSN: 1077-260X. DOI: 10.1109/2944.571775.

[62] Takeshi Yasui, Eisuke Saneyoshi, and Tsutomu Araki. “Asynchronous optical sampling terahertz time-domain spectroscopy for ultrahigh spectral resolution and rapid data acquisition”. In: *Applied Physics Letters* 87.6 (2005), p. 061101. DOI: 10.1063/1.2008379. eprint: https://doi.org/10.1063/1.2008379. URL: https://doi.org/10.1063/1.2008379.

[63] A. Bartels et al. “High-resolution THz spectrometer with kHz scan rates”. In: *Opt. Express* 14.1 (Jan. 2006), pp. 430–437. DOI: 10.1364/OPEX.14.000430. URL: http://www.opticsexpress.org/abstract.cfm?URI=oe-14-1-430.

[64] M. van Exter and D. R. Grischkowsky. “Characterization of an optoelectronic terahertz beam system”. In: *IEEE Transactions on Microwave Theory and Techniques* 38.11 (Nov. 1990), pp. 1684–1691. ISSN: 0018-9480. DOI: 10.1109/22.60016.

[65] C. M. Morris et al. “Polarization modulation time-domain terahertz polarimetry”. In: *Opt. Express* 20.11 (May 2012), pp. 12303–12317. DOI: 10.1364/OE.20.012303. URL: http://www.opticsexpress.org/abstract.cfm?URI=oe-20-11-12303.

[66] L.G. Cohen, Chinlon Lin, and W.G. French. "Tailoring zero chromatic dispersion into the 1.5–1.6 µm low-loss spectral region of single-mode fibres". English. In: *Electronics Letters* 15 (12 June 1979), 334–335(1). ISSN: 0013-5194. URL: https://digital-library.theiet.org/content/journals/10.1049/el_19790237.

[67] Martin van Exter, Ch. Fattinger, and D. Grischkowsky. "Terahertz time-domain spectroscopy of water vapor". In: *Opt. Lett.* 14.20 (Oct. 1989), pp. 1128–1130. DOI: 10.1364/OL.14.001128. URL: http://ol.osa.org/abstract.cfm?URI=ol-14-20-1128.

[68] National Institute of Standards and Technology (NIST). *Hall effect measurements*. June 2021. URL: https://www.nist.gov/pml/nanoscale-device-characterization-division/popular-links/hall-effect (visited on 02/06/2022).

[69] David M. Mahler et al. "Massive and Topological Surface States in Tensile-Strained HgTe". In: *Nano Letters* 21.23 (2021). PMID: 34812638, pp. 9869–9874. DOI: 10.1021/acs.nanolett.1c02456. eprint: https://doi.org/10.1021/acs.nanolett.1c02456. URL: https://doi.org/10.1021/acs.nanolett.1c02456.

[70] Jun Nakagawa et al. "Magnetic field enhancement of water vaporization". In: *Journal of Applied Physics* 86.5 (1999), pp. 2923–2925. DOI: 10.1063/1.371144. URL: https://doi.org/10.1063/1.371144.

[71] Edward Bormashenko. "Moses effect: physics and applications". In: *Advances in Colloid and Interface Science* 269 (2019), pp. 1–6. ISSN: 0001-8686. DOI: https://doi.org/10.1016/j.cis.2019.04.003. preprint: https://doi.org/10.20944/preprints201901.0152.v1. URL: https://www.sciencedirect.com/science/article/pii/S0001868619300636.

[72] Koichi Kitazawa et al. "Magnetic field effects on water, air and powders". In: *Physica B: Condensed Matter* 294-295 (2001). Proceedings of the Sixth International Symposium on Research in High Magnetic Fields, pp. 709–714. ISSN: 0921-4526. DOI: https://doi.org/10.1016/S0921-4526(00)00749-3. URL: https://www.sciencedirect.com/science/article/pii/S0921452600007493.

[73] Deepu K. George, Ali Charkhesht, and N. Q. Vinh. "New terahertz dielectric spectroscopy for the study of aqueous solutions". In: *Review of Scientific Instruments* 86.12 (2015), p. 123105. DOI: 10.1063/1.4936986. eprint: https://doi.org/10.1063/1.4936986.

[74] G. Ghosh. "Temperature dispersion of refractive indexes in some silicate fiber glasses". In: *IEEE Photonics Technology Letters* 6.3 (Mar. 1994), pp. 431–433. ISSN: 1941-0174. DOI: 10.1109/68.275509.

[75] J. L. Cruz, M. V. Andres, and M. A. Hernandez. "Faraday effect in standard optical fibers: dispersion of the effective Verdet constant". In: *Appl. Opt.* 35.6 (Feb. 1996), pp. 922–927. DOI: 10.1364/AO.35.000922. URL: http://ao.osa.org/abstract.cfm?URI=ao-35-6-922.

[76] M. F. Wagdy and S. S. Awad. "Effect of sampling jitter on some sinewave measurements". In: *6th IEEE Conference Record., Instrumentation and Measurement Technology Conference*. 1989, pp. 195–198. DOI: 10.1109/IMTC.1989.36850.

[77] A Rogalski. "HgCdTe infrared detector material: history, status and outlook". In: *Reports on Progress in Physics* 68.10 (Aug. 2005), p. 2267. DOI: 10.1088/0034-4885/68/10/R01. URL: https://dx.doi.org/10.1088/0034-4885/68/10/R01.

[78] P. Capper et al., eds. *Mercury Cadmium Telluride: Growth, Properties and Applications*. Wiley Series in Materials for Electronic & Optoelectronic Applications. Wiley, 2010. ISBN: 9780470669464. DOI: https://doi.org/10.1002/9780470669464.

[79] T. Skauli and T. Colin. "Accurate determination of the lattice constant of molecular beam epitaxial CdHgTe". In: *Journal of Crystal Growth* 222.4 (2001), pp. 719–725. ISSN: 0022-0248. DOI: https://doi.org/10.1016/S0022-0248(00)01005-8. URL: https://www.sciencedirect.com/science/article/pii/S0022024800010058.

[80] Junhao Chu and Arden Sher. *Physics and properties of narrow gap semiconductors*. Vol. 1. Springer, 2008. DOI: https://doi.org/10.1007/978-0-387-74801-6.

[81] J.N. Schulman and T.C. McGill. "Evanescent states and the CdTe/HgTe superlattice". In: *Solid State Communications* 34.1 (1980), pp. 29–31. ISSN: 0038-1098. DOI: https://doi.org/10.1016/0038-1098(80)90622-5. URL: https://www.sciencedirect.com/science/article/pii/0038109880906225.

[82] Y. R. Lin-Liu and L. J. Sham. "Interface states and subbands in HgTe-CdTe heterostructures". In: *Phys. Rev. B* 32 (8 Oct. 1985), pp. 5561–5563. DOI: 10.1103/PhysRevB.32.5561. URL: https://link.aps.org/doi/10.1103/PhysRevB.32.5561.

[83] N A Cade. "Quantum well bound states of HgTe in CdTe". In: *Journal of Physics C: Solid State Physics* 18.26 (Sept. 1985), p. 5135. DOI: 10.1088/0022-3719/18/26/024. URL: https://dx.doi.org/10.1088/0022-3719/18/26/024.

[84] J. N. Schulman and Yia-Chung Chang. "HgTe-CdTe superlattice subband dispersion". In: *Phys. Rev. B* 33 (4 Feb. 1986), pp. 2594–2601. DOI: 10.1103/PhysRevB.33.2594. URL: https://link.aps.org/doi/10.1103/PhysRevB.33.2594.

[85] K. C. Woo, S. Rafol, and J. P. Faurie. "Magnetotransport properties of p-type HgTe-CdTe superlattices". In: *Phys. Rev. B* 34 (8 Oct. 1986), pp. 5996–5999. DOI: 10.1103/PhysRevB.34.5996. URL: https://link.aps.org/doi/10.1103/PhysRevB.34.5996.

[86] J. R. Meyer et al. "Ultrahigh electron and hole mobilities in zero-gap Hg-based superlattices". In: *Phys. Rev. B* 38 (3 July 1988), pp. 2204–2207. DOI: 10.1103/PhysRevB.38.2204. URL: https://link.aps.org/doi/10.1103/PhysRevB.38.2204.

[87] O A Pankratov. "Electronic properties of band-inverted heterojunctions: supersymmetry in narrow-gap semiconductors". In: *Semiconductor Science and Technology* 5.3S (Mar. 1990), S204. DOI: 10.1088/0268-1242/5/3S/045. URL: https://dx.doi.org/10.1088/0268-1242/5/3S/045.

[88] M. Fornari et al. "Electronic structure and wave functions of interface states in HgTe-CdTe quantum wells and superlattices". In: *Phys. Rev. B* 55 (24 June 1997), pp. 16339–16348. DOI: 10.1103/PhysRevB.55.16339. URL: https://link.aps.org/doi/10.1103/PhysRevB.55.16339.

[89] P Ballet et al. "MBE growth of strained HgTe/CdTe topological insulator structures". In: *Journal of electronic materials* 43.8 (2014), pp. 2955–2962.

[90] C. Berger and F. Bayer. *Lithographic processes and masks for THz transmission compatible HgTe sample fabrication*. Apr. 27, 2021. URL: https://git.physik.uni-wuerzburg.de/ag-kiessling/setup-data/thz-lithography.

[91] E D Palik and J K Furdyna. “Infrared and microwave magnetoplasma effects in semiconductors”. In: *Reports on Progress in Physics* 33.3 (Sept. 1970), pp. 1193–1322. DOI: 10.1088/0034-4885/33/3/307. URL: https://doi.org/10.1088%2F0034-4885%2F33%2F3%2F307.

[92] A. M. Shuvaev et al. “Giant Magneto-Optical Faraday Effect in HgTe Thin Films in the Terahertz Spectral Range”. In: *Phys. Rev. Lett.* 106 (10 Mar. 2011), p. 107404. DOI: 10.1103/PhysRevLett.106.107404. URL: https://link.aps.org/doi/10.1103/PhysRevLett.106.107404.

[93] Jan Gospodarič et al. “Energy spectrum of semimetallic HgTe quantum wells”. In: *Phys. Rev. B* 104 (11 Sept. 2021), p. 115307. DOI: 10.1103/PhysRevB.104.115307. URL: https://link.aps.org/doi/10.1103/PhysRevB.104.115307.

[94] L S Bovkun et al. “Landau level spectroscopy of valence bands in HgTe quantum wells: effects of symmetry lowering”. In: *Journal of Physics: Condensed Matter* 31.14 (Feb. 2019), p. 145501. DOI: 10.1088/1361-648x/aafdf0. URL: https://doi.org/10.1088/1361-648x/aafdf0.

[95] J. Ziegler et al. “Quantum Hall effect and Landau levels in the three-dimensional topological insulator HgTe”. In: *Phys. Rev. Research* 2 (3 July 2020), p. 033003. DOI: 10.1103/PhysRevResearch.2.033003. URL: https://link.aps.org/doi/10.1103/PhysRevResearch.2.033003.

[96] O. Madelung, U. Rössler, and M. Schulz, eds. *Mercury telluride (HgTe) Luttinger and Kane parameters: Datasheet from Landolt-Börnstein - Group III Condensed Matter · Volume 41B: “II-VI and I-VII Compounds; Semimagnetic Compounds” in SpringerMaterials (https://doi.org/10.1007/10681719_674)*. accessed 2022-03-23. DOI: 10.1007/10681719_674. URL: https://materials.springer.com/lb/docs/sm_lbs_978-3-540-31359-5_674.

[97] Valentin Leander Müller. “Transport signatures of topological and trivial states in the three-dimensional topological insulator HgTe”. doctoral thesis. Universität Würzburg, 2022. DOI: 10.25972/OPUS-25952. URL: https://nbn-resolving.org/urn:nbn:de:bvb:20-opus-259521.

[98] R. Winkler. “Rashba spin splitting in two-dimensional electron and hole systems”. In: *Phys. Rev. B* 62 (7 Aug. 2000), pp. 4245–4248. DOI: 10.1103/PhysRevB.62.4245. URL: https://link.aps.org/doi/10.1103/PhysRevB.62.4245.

[99] R Winkler. “A note on analytic quadratic Brillouin zone integration”. In: *Journal of Physics: Condensed Matter* 5.15 (Apr. 1993), p. 2321. DOI: 10.1088/0953-8984/5/15/005. URL: https://dx.doi.org/10.1088/0953-8984/5/15/005.

[100] Till Andlauer and Peter Vogl. “Full-band envelope-function approach for type-II broken-gap superlattices”. In: *Phys. Rev. B* 80 (3 July 2009), p. 035304. DOI: 10.1103/PhysRevB.80.035304. URL: https://link.aps.org/doi/10.1103/PhysRevB.80.035304.

[101] Jiawei Ruan et al. “Symmetry-protected ideal Weyl semimetal in HgTe-class materials”. In: *Nature communications* 7.1 (2016), p. 11136.

[102] David M. Mahler et al. “Interplay of Dirac Nodes and Volkov-Pankratov Surface States in Compressively Strained HgTe”. In: *Phys. Rev. X* 9 (3 Aug. 2019), p. 031034. DOI: 10.1103/PhysRevX.9.031034. URL: https://link.aps.org/doi/10.1103/PhysRevX.9.031034.

C Calculation parameters

All calculations shown in this work have been done using `kdotpy` [37] (version given below for each calculation) on the author's workstation with following specification: AMD Ryzen Threadripper 2970WX (24-core processor), 128 GB RAM, Windows 10, Python 3.9.5 (numpy 1.21.2, scipy 1.7.1). A suitable data repository is not yet available, data can be requested from the author or Dr. Tobias Kießling. Specific parameters (e.g. number of CPUs to use) have been removed from the command line to enable easy interoperability with other workstations. Scripts for customized plotting can be found at `https://git.physik.uni-wuerzburg.de/ag-kiessling/kdotp-matlab-scripts`.

[C1] F. Bayer. *Bulk CdTe, kdotpy-bulk, axial approximation.* Version 0.87. Physikalisches Institut, Universität Würzburg, Jan. 15, 2023. Command line: `kdotpy-bulk.py norb 8 obs orbitalrgb erange -1700 1400 kz 0 4 / 100 split 0.01 mater CdTe msubst CdTe ignorestrain noax out _CdTe outdir ./data/Bulk char legend symmetrize`.

[C2] F. Bayer. *Bulk HgTe, kdotpy-bulk, axial approximation.* Version 0.87. Physikalisches Institut, Universität Würzburg, Jan. 15, 2023. Command line: `kdotpy-bulk.py norb 8 obs orbitalrgb erange -1700 1400 kz 0 4 / 100 split 0.01 mater HgTe msubst CdTe ignorestrain noax out _HgTe outdir ./data/Bulk char legend symmetrize`.

[C3] F. Bayer. *Bulk HgTe strained on CdTe, kdotpy-bulk, axial approximation.* Version 0.87. Physikalisches Institut, Universität Würzburg, Jan. 15, 2023. Command line: `kdotpy-bulk.py norb 8 obs orbitalrgb erange -1700 1400 kz 0 4 / 500 split 0.01 mater HgTe msubst CdTe noax out _HgTe_onCdTe outdir ./data/Bulk char legend symmetrize`.

[C4] F. Bayer. *HgTe 5nm, kdotpy-2d (k-dispersion), axial mode.* Version 0.87. Physikalisches Institut, Universität Würzburg, Jan. 15, 2023. Command line: `kdotpy-2d.py temp 1.7 zres 0.25 lbarr 10 lwell 5 k 0 0.5 / 200 kphi 45 b 0 mwell HgTe mbarr HgCdTe 0.68 msubst CdTe erange -1000 1000 targetenergy 50 neig 60 norb 8 axial obs orbitalrgb dimful plotstyle auto legend char verbose split -0.01 out _HgTe5nm outdir ./data/HgTe5 symmetrize`.

[C5] F. Bayer. *HgTe 8nm, kdotpy-2d (k-dispersion), axial mode.* Version 0.87. Physikalisches Institut, Universität Würzburg, Jan. 15, 2023. Command line: `kdotpy-2d.py temp 1.7 zres 0.25 lbarr 10 lwell 8 k 0 0.5 / 200 kphi 45 b 0 mwell HgTe mbarr HgCdTe 0.68 msubst CdTe erange -1000 1000 targetenergy 150 neig 80 norb 8 axial obs orbitalrgb dimful plotstyle auto legend char verbose split -0.01 out _HgTe8nm outdir ./data/HgTe8 symmetrize`.

[C6] F. Bayer. *HgTe 30nm, kdotpy-2d (k-dispersion), axial mode.* Version 0.87. Physikalisches Institut, Universität Würzburg, Jan. 15, 2023. Command line: `kdotpy-2d.py temp 1.7 zres 0.25 lbarr 10 lwell 30 k 0 0.5 / 200 kphi 45 b 0 mwell HgTe mbarr HgCdTe 0.68 msubst CdTe erange -300 400 targetenergy 20 neig 80 norb 8 axial obs orbitalrgb dimful plotstyle auto legend char verbose split -0.01 out _HgTe30nm outdir ./data/HgTe30 symmetrize`.

[C7] F. Bayer. *HgTe 30nm, kdotpy-ll, axial mode*. Version 0.67. Physikalisches Institut, Universität Würzburg, July 13, 2021. Command line: `kdotpy-ll.py lbarr 10 lwell 30 zres 0.35 mwell HgTe mbarr HgCdTe 0.68 msubst CdTe b 0 12 // 89 temp 1.7 targetenergy 15 nll 30 neig 400 norb 8 erange -50 100 obs llindex plotstyle auto legend transitions dos cardens -0.002 0.008 / 0.0005 char dimful split 0.01 out _HgTe30_Pot0 outdir ./data/new-transitions/HgTe30/axial`.

[C8] F. Bayer. *HgTe 45nm, kdotpy-ll, axial mode*. Version 0.67. Physikalisches Institut, Universität Würzburg, July 26, 2021. Command line: `kdotpy-ll.py lbarr 10 lwell 45 zres 0.35 mwell HgTe mbarr HgCdTe 0.68 msubst CdTe b 0 12 // 89 temp 1.7 targetenergy 15 nll 30 neig 400 norb 8 erange -50 100 obs llindex plotstyle auto legend transitions dos cardens -0.002 0.008 / 0.0005 char dimful split 0.01 out _HgTe45_Pot0 outdir ./data/new-transitions/HgTe45/axial`.

[C9] F. Bayer. *HgTe 58nm, kdotpy-ll, axial mode*. Version 0.70. Physikalisches Institut, Universität Würzburg, Nov. 8, 2021. Command line: `kdotpy-ll.py lbarr 10 lwell 58 zres 0.35 mwell HgTe mbarr HgCdTe 0.68 msubst CdTe b 0 12 // 200 temp 1.7 targetenergy 15 nll 30 neig 400 norb 8 erange -50 100 obs llindex plotstyle auto legend transitions dos cardens -0.002 0.009 / 0.0005 char dimful split -0.01 out _HgTe58_Pot0 outdir ./data/new-transitions/HgTe58/axial`.

[C10] F. Bayer. *HgTe 58nm, kdotpy-ll, axial mode*. Version 0.77. Physikalisches Institut, Universität Würzburg, Mar. 9, 2022. Command line: `kdotpy-ll.py lbarr 10 lwell 58 zres 0.35 mwell HgTe mbarr HgCdTe 0.68 msubst CdTe b 0 12 // 200 temp 1.7 targetenergy 25 nll 30 neig 660 norb 8 erange -50 100 obs llindex plotstyle auto legend transitions dos cardens -0.010 0.0240 / 0.0005 char dimful split -0.01 out _HgTe58_Pot0 outdir ./data/HgTe58/axial`.

[C11] F. Bayer. *HgTe 58nm, kdotpy-2d (k-dispersion), axial mode*. Version 0.77. Physikalisches Institut, Universität Würzburg, Mar. 24, 2022. Command line: `kdotpy-2d.py lbarr 10 lwell 58 zres 0.25 mwell HgTe mbarr HgCdTe 0.68 msubst CdTe k 0 0.6 / 100 kphi 45 b 0 temp 1.7 targetenergy -100 neig 400 norb 8 erange -1000 600 obs interfacechar10nm plotstyle auto legend char dimful split -0.01 out _HgTe58_Pot0 outdir ./data/HgTe58/2D/axial`.

[C12] F. Bayer. *HgTe 30nm, kdotpy-ll, axial mode, wavefunctions*. Version 0.79. Physikalisches Institut, Universität Würzburg, June 29, 2022. Command line: `kdotpy-ll.py lbarr 10 lwell 30 zres 0.25 mwell HgTe mbarr HgCdTe 0.68 msubst CdTe b 0 12 / 0.2 temp 1.7 targetenergy 15 nll 15 neig 250 norb 8 erange -50 100 obs llindex plotstyle auto legend char dimful split -0.01 plotwf out _HgTe30 outdir ./data/HgTe30/axial/WF`.

[C13] F. Bayer. *HgTe 30nm, kdotpy-ll, axial mode*. Version 0.70. Physikalisches Institut, Universität Würzburg, Nov. 30, 2021. Command line: `kdotpy-ll.py lbarr 10 lwell 30 zres 0.35 mwell HgTe mbarr HgCdTe 0.68 msubst CdTe b 0 12 // 300 temp 1.7 targetenergy 15 nll 30 neig 400 norb 8 erange -50 100 obs llindex plotstyle auto legend transitions dos cardens`

`-0.01 0.01 / 0.0005 char dimful split -0.01 out _HgTe30 outdir ./data/HgTe30/axial`.

[C14] F. Bayer. *HgTe 30nm, kdotpy-ll, noax mode*. Version 0.72. Physikalisches Institut, Universität Würzburg, Dec. 1, 2021. Command line: `kdotpy-ll.py temp 1.7 zres 0.35 lbarr 10 lwell 30 nll 30 b 0 12 // 300 mwell HgTe mbarr HgCdTe 0.68 msubst CdTe erange -50 100 targetenergy 15 neig 400 norb 8 noax obs llavg llobs plotstyle auto legend transitions dos cardens -0.01 0.01 / 0.0005 char dimful split -0.01 out _HgTe30 outdir ./data/HgTe30/noax`.

[C15] F. Bayer. *HgTe 30nm, kdotpy-ll, bia mode*. Version 0.72. Physikalisches Institut, Universität Würzburg, Dec. 2, 2021. Command line: `kdotpy-ll.py temp 1.7 zres 0.35 lbarr 10 lwell 30 nll 30 b 0 12 // 300 mwell HgTe mbarr HgCdTe 0.68 msubst CdTe erange -50 100 targetenergy 15 neig 400 norb 8 noax bia obs llavg llobs plotstyle auto legend transitions dos cardens -0.01 0.01 / 0.0005 char dimful split -0.01 out _HgTe30 outdir ./data/HgTe30/bia/default_params`.

[C16] F. Bayer. *HgTe 30nm, kdotpy-ll, bia mode, with electrostatic potential*. Version 0.77 with commit `ef42de5b16`. Physikalisches Institut, Universität Würzburg, Mar. 23, 2022. Command line: `kdotpy-ll.py temp 1.7 zres 0.35 lbarr 5 lwell 30 nll 30 b 0 12 // 299 mwell HgTe mbarr HgCdTe 0.68 erange -50 100 targetenergy 15 neig 360 norb 8 noax bia msubst CdTe obs llavg llobs plotstyle auto legend transitions dos cardens -0.002 0.004 / 0.0005 char dimful split -0.01 out _HgTe30_vs_0_20_12nm_moreLL outdir ./data/HgTe30/bia/default_params/vsurf_quad_asym/depth vsurf [0,0,20,0] 12 q`.

D Dataset references

A list of all experiment datasets used throughout this work. All experiments have been designed and conducted by the author. Support by colleges during measurements is acknowledged per entry. Most measurements run over multiple days and the given date labels the starting date. Links (where available) point to the raw data repository and entries in the electronic lab book instance *eLabFTW* (access can be provided by the responsible person of SFB 1170 project Z03). Data storage locations may change in the future. Access to data, evaluation scripts and supplementary calculations is also provided by the author upon request.

[D1] F. Bayer. *Reference spectra with empty cryostat.* 1–23. System at base temperature < 2 K. C129 THz, Physikalisches Institut, Universität Würzburg, June 7, 2019.

[D2] F. Bayer. *Reference spectra with empty cryostat.* C129 THz, Physikalisches Institut, Universität Würzburg, Feb. 2021. URL: `https://elabftw.ctqmat.de/experiments.php?mode=view&id=299` `https://git.physik.uni-wuerzburg.de/ag-kiessling/setup-data/thz-data`.

[D3] C. Berger and F. Bayer. *Monitoring of THz transmision through empty cryostat with partially open beam path housing.* 2. C129 THz, Physikalisches Institut, Universität Würzburg, Oct. 18, 2020. URL: `https://elabftw.ctqmat.de/experiments.php?mode=view&id=166` `https://git.physik.uni-wuerzburg.de/ag-kiessling/setup-data/thz-data`.

[D4] C. Berger and F. Bayer. *THz spot profiling.* C129 THz, Physikalisches Institut, Universität Würzburg, Oct. 23, 2019. URL: `https://elabftw.ctqmat.de/experiments.php?mode=view&id=361`.

[D5] F. Bayer. *Reference spectra with empty cryostat.* 1. System at base temperature < 2 K. C129 THz, Physikalisches Institut, Universität Würzburg, June 13, 2019.

[D6] F. Bayer. *Measurement of THz polarization in empty cryostat over more than a month.* 1. C129 THz, Physikalisches Institut, Universität Würzburg, Feb. 25, 2020. URL: `https://elabftw.ctqmat.de/experiments.php?mode=view&id=345` `https://git.physik.uni-wuerzburg.de/ag-kiessling/setup-data/thz-data`.

[D7] F. Bayer. *Gated THz measurement on Q3236-THz1 (30 nm HgTe) below T=2 K.* C129 THz, Physikalisches Institut, Universität Würzburg, Oct. 1, 2021. URL: `https://git.physik.uni-wuerzburg.de/ag-kiessling/setup-data/thz-data` `https://elabftw.ctqmat.de/experiments.php?mode=view&id=702`.

[D8] F. Bayer. *Gated THz measurement on Q3219-THz1 (45 nm HgTe) below T=2 K.* C129 THz, Physikalisches Institut, Universität Würzburg, May 31, 2021. URL: `https://git.physik.uni-wuerzburg.de/ag-kiessling/setup-data/thz-data` `https://elabftw.ctqmat.de/experiments.php?mode=view&id=542`.

[D9] F. Bayer. *Gated THz measurement on Q3071-THz1 (58 nm HgTe) below T=2 K.* This measurement series was interrupted by a power blackout at the facility and continued on 2020-06-29. C129 THz, Physikalisches Institut, Universität Würzburg, June 18, 2020. URL: `https://git.physik.uni-wuerzburg.de/ag-kiessling/setup-data/thz-data` `https://elabftw.ctqmat.de/experiments.php?mode=view&id=111`.

[D10] F. Bayer. *Gated THz measurement on Q2833-THz2 (70 nm HgTe) below T=2 K*. 3,4,6. Old data taken with first version of THz setup. Sample not measured again due to issues with contacts and gating. C129 THz, Physikalisches Institut, Universität Würzburg, Jan. 30, 2019. URL: https://elabftw.ctqmat.de/experiments.php?mode=view&id=215.